Department of Environmental Engineering
University of Genova

Michele Bolla Pittaluga

Long term morphodynamic equilibrium of tidal channels

Sede Amministrativa: Università degli Studi di Padova
Sede Consorziata: DIAM - Università degli Studi di Genova

Dottorato di Ricerca in
Ingegneria Idraulica e Modellistica dei Sistemi Ambientali
XV CICLO

Michele Bolla Pittaluga

Long term morphodynamic equilibrium of tidal channels

Supervisore:
Prof. Giovanni Seminara -Università degli Studi di Genova

Revisore:
Prof. Andrea Defina - Università degli Studi di Padova

Università degli Studi di Padova
Dottorato di Ricerca in Ingegneria Idraulica e Modellistica dei Sistemi Ambientali

XV CICLO

Coordinatore:
Prof. Andrea Rinaldo - Università degli Studi di Padova

Coommissione esaminatrice:
Prof. Erik Mosselmann - Delft Hydraulics
Prof. Bruno Brunone - Università degli Studi di Perugia
Prof. Enrico Foti - Università degli Studi di Catania
Prof. Marino Gatto - Politecnico di Milano

Esame finale:
24 Febbraio 2003

Contents

List of Figures

Riassunto

La presente tesi è suddivisa in tre capitoli.

Nel primo Capitolo viene sviluppato un modello per il trasporto in sospensione mediato sulla profondità, fondato su un classico metodo perturbativo. Tale approccio si basa sull'esistenza nel problema di parametri piccoli che misurano l'importanza relativa della convezione longitudinale e delle variazioni locali di concentrazione rispetto alla diffusione turbolenta e alla sedimentazione. Lo sviluppo dell'analisi evidenzia i limiti del modello sviluppato originariamente da *Galappatti* [1983], successivamente generalizzato da *Wang* [1992] e *Katopodi* [1992] e diffusamente utilizzato nei codici numerici in commercio. Si dimostra infatti che, anziché condurre ad un'equazione differenziale per la concentrazione mediata sulla profondità, l'approccio corretto conduce a correzioni di ordine superiore della classica distribuzione di Rouse, espresse in termini delle derivate spaziali e temporali della soluzione al minimo ordine. Utilizzando tale procedimento viene quindi qui derivata una formula per il trasporto solido in sospensione, utilizzabile in numerosi contesti relativi alla morfodinamica fluviale e lagunare.

Nel Capitolo 2 si investiga l'equilibrio morfodinamico di lungo termine di canali mareali attraverso un modello numerico unidimensionale. Punto di partenza dell'analisi è il recente contributo di *Lanzoni e Seminara* [2002], dove si dimostrava che i canali mareali possono raggiungere una configurazione di equilibrio caratterizzata da flusso netto di sedimenti nullo in un ciclo mareale. Vengono quindi rimosse alcune ipotesi semplificative e viene valutato il loro effetto sulla configurazione di equilibrio. In particolare vengono introdotti i seguenti ingredienti: una marea quarto-diurna M_4 presente nella forzante, gli effetti di non equilibrio sul trasporto in sospensione e l'influenza di una alimentazione di sedimenti alla bocca. Di quest'ultima si tiene conto attraverso un modello semplificato secondo il quale il flusso di sedimenti durante la fase di riflusso è governato dalla capacità di trasporto del canale, mentre durante la fase di flusso esso viene determinato sulla base di una concentrazione fissata all'imbocco.

I precedenti risultati teorici sono confermati dalle indagini sperimentali effettuate nel laboratorio del Dipartimento di Ingegneria Ambientale dell'Università di Genova, riportate nell'ultimo capitolo. In particolare i due esperimenti descritti nel Capitolo 3 hanno consentito di verificare che i canali mareali chiusi ad una estremità e connessi ad un bacino oscillante

dall'altra raggiungono una configurazione di equilibrio morfodinamico. Inoltre, gli esperimenti hanno mostrato che il grado dominanza flusso/riflusso nella regione prossima all'imbocco è ridotto rispetto alle osservazioni e alle predizioni effettuate da *Blondeaux et al.* [1982] nell'ambito di una schematizzazione a fondo fisso. Infine, è stata anche osservata nel canale la formazione di barre libere mareali le cui caratteristiche si rivelano in accordo con la recente teoria di *Seminara e Tubino* [2001]. Le condizioni di similitudine che assicurano la corrispondenza tra modello e un caratteristico canale mareale prototipo sono discusse nell'ambito di quest'ultimo Capitolo.

Abstract

The present work consists of three Chapters.

Chapter 1 is devoted to the development of a depth averaged model for the transport of suspended sediment, based on a rational perturbation method. Such approach relies on the existence of small parameters measuring the relative importance of advection and local variations of concentration versus turbulent diffusion and gravitational settling. The development of the analysis points out the limits of the approach originally developed by *Galappatti* [1983], later generalized by *Wang* [1992] and *Katopodi* [1992] and widely employed in commercial codes. In fact we show that, rather than deriving a differential equation for the depth averaged concentration, the correct approach leads to a sequence of higher order corrections for the depth averaged concentration, expressed in terms of spatial and temporal derivatives of the leading order solution. A simple relationship for the flux of suspended sediment, suitable to applications to a variety of morphodynamic computations is finally provided.

In Chapter 2 the long term equilibrium of tidal channels is investigated through a one dimensional numerical model. The starting point of the analysis is the recent contribution of *Lanzoni and Seminara* [2002], where it was shown that tidal channels may achieve an equilibrium configuration characterized at each cross section by a vanishing net sediment flux in a tidal cycle. In the present work some simplifying hypotheses assumed in the latter contribution are removed and their effect on the equilibrium configuration is evaluated. In particular, the following novel ingredients are introduced: a quarter-diurnal overtide M_4 present in the tidal forcing, non equilibrium effects on the suspended sediment transport and the role of sediment supply. The latter is accounted for through a simple model whereby the sediment flux during the ebb phase is assumed to be controlled by the transport capacity in the channel, while during the flood phase it is taken to be forced by some externally driven concentration.

In the final Chapter the above theoretical findings are substantiated through the results of a controlled laboratory investigation carried out in the laboratory of the Department of Environmental Engineering of the University of Genova (Italy). In particular the two experiments described in Chapter 3 allowed to check that tidal channels closed at one end and connected to the other end with a tidal sea do indeed reach a morphodynamic

equilibrium. Moreover, the experiments showed that the degree of ebb-flood flow asymmetry in the 'sea' region close to the inlet is reduced compared to the one observed and predicted in the fixed bed case by *Blondeaux et al.* [1982]. Finally tidal free bars were also observed in accordance with the theory of *Seminara and Tubino* [2001]. The theoretical foundation of the scaling arguments insuring similarity between the present model and a prototype tidal channel are also discussed in the final Chapter.

Acknowledgments

I wish to thank first of all and most of all my supervisor, Giovanni Seminara, who has been unfailingly brilliant to work with. He has been an enthusiastic and constant source of inspiration besides a continuous support. Thanks are also due to Prof. Defina for his agreement to read this work. I also thank Prof. E. Marchi, whom I have had the pleasure and the honour to work with.

I am deeply grateful to Marco Tubino who introduced me to the spectacular world of research and to all the scientists I met during these years, and particularly to Marco Colombini, Rodolfo Repetto, Stefano Lanzoni, Andrea Rinaldo, Giampaolo Di Silvio and Luigi D'Alpaos. I also thank all the people working in the Department of Environmental Engineering of the University of Genova and especially Marco Galiani, Giancarlo Cassini, Luigi Stagi, Tina D'Agostino, Franco Porcile, Gianni Ruà and Piero Manzoli.

A special thank to Giovanni, Nunzio, Bianca, Michele, Laura, Luca, Veronica and Alessandro who shared with me this Ph.D. experience: they are special friends more than colleagues. Many thanks in particular to Nicoletta whose contribution has been crucial to the successful performance of our laboratory experiments. Thanks are also due to Caterina, Valeria e Paola for their collaboration for the laboratory experiments.

This thesis is dedicated to my wife Fede, who has constantly encouraged me throughout my activity, as well as to our daughter Laura and the new baby we are expecting.

Introduction

In order to set the scene for our discussion and motivate the reader it may be of help to describe briefly a case study of special importance: the Venice Lagoon. In fact, this work was originally motivated by the need to understand the main processes contributing to the morphodynamic evolution of a lagoon system. A brief history of the Venice Lagoon is very instructive to appreciate the fact that estuaries and lagoons are indeed fairly delicate environments, hardly in equilibrium: on the contrary, they evolve at a rate depending on a variety of factors, some of them being of anthropic nature.

The Venice Lagoon formed at the mouth of various rivers, notably Brenta, Piave and Sile. Since the medieval age the main concern of the Venice Republic was the increasing siltation of the lagoon: in fact an extensive reduction of flow depth threatened the efficiency of navigation, crucially important for strategic as well as for commercial reasons, and implied a reduction of the flushing effect of tidal currents, with the consequent development of unhealthy conditions due to the prevalence of fresh waters of fluvial origin. Note that the increased siltation of the lagoon was likely caused by the construction of a levee protection system for the population residing in the river valleys, which were subject to frequent inundations. The channelization of the rivers caused an increased sediment load discharged into the lagoon. Here is the first important example of how anthropization may affect the equilibrium of estuaries and lagoons.

The response of the Venice Republic was quite effective through the establishment, at the beginning of the 16th century, of a new governing body (the *Magistrato alle Acque*) responsible for all matters concerning the management of the Venice Lagoon, including the lagoon itself, as well as the rivers debouching into it and the coasts. Various major actions were then taken to reduce siltation: in particular, the mouths of the Brenta, Piave and Sile were diverted outside the lagoon. The effects of such major works were felt in the course of the next two centuries: tidal flats (called *barene*) stopped prograding, shoals (so called *bassifondi*) deepened while tidal channels increased their cross sections. This is documented by the first extensive and accurate

survey of the Venice Lagoon performed by Denaix (around 1810).

The next major anthropic action was undertaken around the mid 1800: in order to counteract the tendency of the three inlets of the Venice Lagoon (*Lido, Malamocco and Chioggia*) to be progressively obstructed by sediment deposition extending also to the main navigation channels, i.e. in order to improve navigation, jetties were constructed at each inlet. Their lengths were designed to be large enough to move the inlets beyond the regions affected by the coastal bars. The impact of the latter actions was fairly fast: indeed, the depth at the inlets increased as expected, but various further undesirable effects were displayed. In fact, jetties intercepted sediments transported by the littoral currents producing severe progradation of the coastlines to the north of the Lido and Malamocco inlets and on both sides of the Chioggia inlet. Moreover, the coasts adjacent to the islands of Lido and Pellestrina deepened (Fig. 1). Furthermore, a reduction and coarsening of sediments entering the lagoon originated from the seaward displacement of the source of sediments carried by the tidal currents and the enhanced asymmetry of the flow field associated with flood and ebb phases in the inlet region.

Various further anthropic effects have more recently affected the morphodynamic evolution of the Venice Lagoon: subsidence (enhanced by withdrawal of groundwater recently stopped), eusthatism, the construction of new large channels (*canale dei petroli*) which have modified the pattern of tidal currents, the effects of chemical pollution on sea weeds (*Zostera Marina*) (which have largely disappeared thus losing their protecting action on the bottom of the intertidal areas) finally the stirring action of illegal clam-fishing techniques as well as of outboard navigation. As a result of all the above effects an increased tendency to the so called *'lagoon marification'* is now recognized as a major problem which adds further complexity to the related, fundamental problem of defending the city of Venice from the increasingly frequent phenomenon of high water. The role of the scientific community is to develop a better understanding of the main processes contributing to the morphodynamic evolution of the lagoon system in order to help developing appropriate countermeasures to the process of marification of the Venice Lagoon, the tidal environment we ultimately wish to analyze.

The present work investigates few such processes starting with a derivation of a theoretical model for the suspended sediment transport able to account for non equilibrium effects, and then developing some theoretical and experimental investigations on the main processes influencing the morphodynamic evolution of tidal channels.

In fact, in the context of River and Estuarine Morphodynamics it is not uncommon for sediments to be dominantly transported in suspension in streams characterized by spatial and/or temporal variations of the hydro-

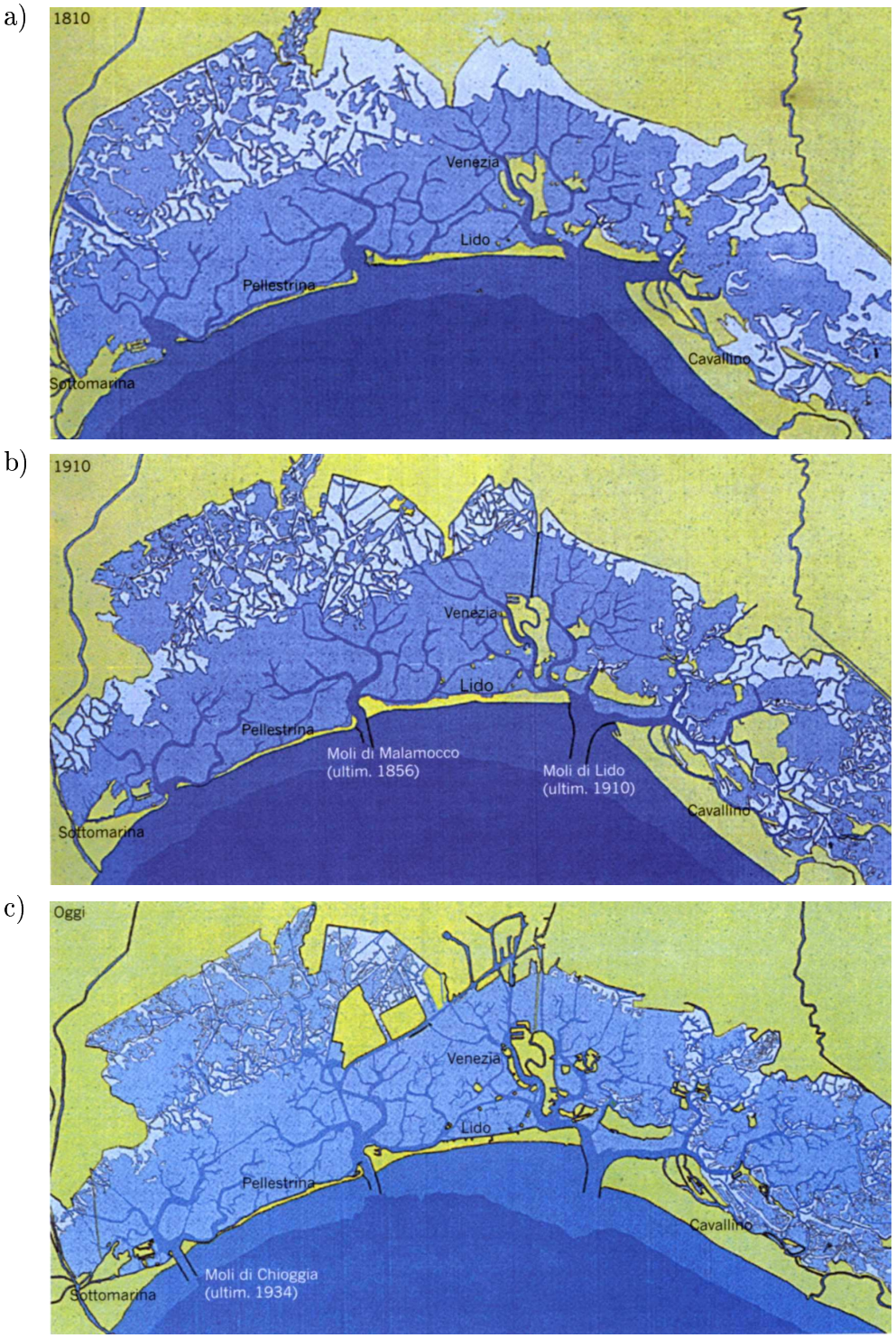

Figure 1: Anthropic effects in the morphodynamic evolution of the Venice Lagoon. a) 1810, b) 1910, c) 2000.

dynamics occurring on very large scales such that, in some sense which will be later defined more precisely, the flow may be considered 'slowly varying' in space and/or time. Typical examples are tidal flows and flood waves. Moreover computations of long term morphodynamical processes are too heavy to be performed using 3D numerical models. Hence the use of depth integrated models proves necessary.

In this sense, the solution of the problem of morphodynamics would benefit from the availability of an appropriate depth averaged model to evaluate the sediment flux transported in suspension.

Developing such a model is the aim pursued in Chapter 1 where we revisit the asymptotic approach originally developed by *Galappatti* [1983], more recently generalized by *Wang* [1992] and *Katopodi* [1992] and widely employed in commercial codes. Such approach relies on the existence of small parameters measuring the relative importance of advection and local variations of concentration versus turbulent diffusion and gravitational settling and is based on a classical regular perturbation expansion (see for instance, *Nayfeh*, 1973), except for the peculiar treatment proposed by the author for the boundary conditions. A comparison, performed on a model problem, between the latter approach and a classical perturbation expansion of the solution in powers of the small parameter has let us discover that Galappatti's approach is indeed formally incorrect. In fact, we show that, if the boundary condition is expanded in powers of the small parameter, rather than deriving a differential equation for the depth averaged concentration as claimed by the above authors, one finds a sequence of higher order corrections for the depth averaged concentration expressed in terms of the spatial and temporal derivatives of the leading order solution.

We have then developed an alternative depth averaged model for the transport of suspended sediment, based on a rational perturbation method, leading to a simple relationship for the flux of suspended sediment, suitable to applications to a variety of morphodynamic computations.

Though the present analysis has been restricted to the 1D case, i.e. assuming that spatial variations of the flow - topography fields occur only in the 'longitudinal' direction, its extension to the 2D case is straightforward. Through such an extension a variety of 2D configurations, like flows in tidal inlets, bifurcations, flows induced by large scale bedforms, become amenable to the present treatment.

Chapter 2 is devoted to investigating theoretically the long term equilibrium of tidal channels. In spite of its relevance, the question of whether tidal channels may achieve a state of morphodynamic equilibrium, defined as a state such that the longitudinal bottom profile of the channel does not undergo net variations within a tidal cycle, has only been partially investi-

gated in the last few years [*Schuttelaars and de Swart*, 1996, 2000; *Lanzoni and Seminara*, 2002] and still awaits to be fully explored. In the present work, we build upon the recent contribution of *Lanzoni and Seminara* [2002] where the latter authors, solving numerically the one dimensional equations for the fluid and solid phases, found that, starting from an arbitrary initial profile, the bottom evolves asymptotically toward an equilibrium configuration everywhere characterized by a vanishing net sediment flux in a tidal cycle. Both the final depth at the inlet and the final length of the channel are determined by channel geometry and tidal forcing. However, the latter work was based on various simplifying assumptions, namely sediment transport was assumed to be in equilibrium with the local and instantaneous hydrodynamic conditions at any cross section (including the inlet) and no overtides were assumed to be present in the tidal forcing. In Chapter 2 we have removed the latter restrictions and we have also taken into account the ebb - flood asymmetry of sediment transport at the inlet through a simple model whereby the sediment flux during the ebb phase is assumed to be controlled by the transport capacity in the channel, while during the flood phase it is taken to be forced by some externally driven concentration. Such effects turn out to affect the long term morphodynamic evolution of tidal channels but none of them prevents channels from reaching equilibrium. The possible presence of tidal flats flanking the main channel has still been neglected and will have to be considered in future developments of the present work.

In the final Chapter, the above theoretical findings are substantiated through the results of a controlled laboratory investigation which were carried out in the laboratory of the Department of Environmental Engineering of the University of Genova (Italy), on a large indoor platform 29.6 m long and 2.3 m wide. To the author's knowledge no attempts to pursue the same goal on the basis of controlled laboratory observations were previously made. Such experimental observations have allowed to check under controlled conditions referring to simple channel geometries, the main mechanisms governing the morphodynamic evolution of tidal channels emerged from the theoretical works mentioned above, a goal quite difficult to achieve on the basis of field observations whose interpretation is generally made complicated by the simultaneous presence of a variety of further natural features whose role cannot be readily isolated. Moreover, the two experiments described in Chapter 3 have allowed us to observe the formation of tidal free bars whose mechanism of formation has recently been analyzed by *Seminara and Tubino* [2001]. The latter authors have showed that the formation of tidal bars arises from an instability of the cohesionless bed, conceptually similar to the well known mechanism underlying the formation of fluvial bars. The unsteady, oscillatory character of tidal flow prevents bar migration, except for a weak

propagation possibly driven by the presence of residual currents. Essentially, bars form whenever the aspect ratio of the channel exceeds a threshold value depending mainly on the intensity of sediment transport measured by the so called Shields parameter. In the conditions reproduced in the experiments, the threshold value of the aspect ratio ranged about few units.

Observations on ripple formation and the morphodynamic evolution of the inlet region are also reported in Chapter 3 where the theoretical foundation of the scaling arguments underlying the physical conditions reproduced in the experiments are also discussed.

The laboratory observations proposed in Chapter 3, which have been performed in collaboration with N. Tambroni, are also reported in *Tambroni et al.* [2003].

Chapter 1

Depth integrated modelling of suspended sediment transport.

We derive a depth averaged model of suspended sediment transport. The development of the analysis leads us to revisit the asymptotic approach originally developed by *Galappatti* [1983], more recently generalized by *Wang* [1992] and *Katopodi* [1992] and widely employed in commercial codes. We show that Galappatti's approach is formally incorrect as it differs from the formal asymptotic expansion of the exact solution. Moreover, the correct approach rather than leading to a differential equation for the depth averaged concentration actually provides higher order corrections for the leading order equilibrium approximation of the depth averaged concentration. Such corrections can be expressed in terms of spatial and temporal derivatives of the leading order solution. The latter picture is demonstrated on two model problems which are easily amenable to analytical treatment. Based on the formal asymptotic expansion of the exact solution, we are then able to derive an analytical form for the flux of suspended sediment in slowly varying flows, which is suitable to applications to a variety of morphodynamic contexts including tidal and fluvial environments. An example of potential applications of the present approach is also provided by examining the problem of suspended sediment transport due a flood wave.

1.1 Introduction

River and Estuarine Morphodynamics is a discipline aimed at predicting the short - long term evolution of the interface between the flowing mixture of water and sediments and the underlying cohesionless (or cohesive) container. It is not uncommon for sediments to be dominantly transported in suspen-

sion in streams characterized by spatial and/or temporal variations of the hydrodynamics occurring on very large scales such that, in some sense to be precisely defined below, the flow may be considered as 'slowly varying' in space and/or time. Typical examples are tidal flows and flood waves. Under the latter conditions, the problems of morphodynamics would benefit from the availability of an appropriate depth averaged model to evaluate the sediment flux transported in suspension.

In 1983 Galappatti (but see also *Galappatti and Vreugdenhil*, 1985) attempted to derive a depth averaged form of the convection diffusion equation for sediment concentration on the basis of an asymptotic approach relying on the existence of small parameters measuring the relative importance of advection and local variations of concentration versus turbulent diffusion and gravitational settling. The approach is then based on a classical regular perturbation expansion (see for instance, *Nayfeh*, 1973), except for the peculiar treatment proposed by the author for the boundary conditions. In fact, essentially the author does not expand the boundary conditions in terms of the small parameter, as is typical of classical perturbation approaches. Rather, he stipulates that the depth averaged value of the concentration is wholly determined by the lower order approximation of the solution, while higher order terms are forced to have vanishing depth average. The boundary condition at the bed interface is eventually reinforced by requiring that the sum of the lowest and higher order components of the solution must satisfy it. This leads to a relationship which the author treats as a differential equation for the as yet unknown depth averaged concentration.

We wish to compare the latter approach with a classical perturbation expansion of the solution in powers of the small parameter. Such exercise proves instructive. Indeed, various interesting results arise:

1. Galappatti's solution is found to differ from the classical perturbation expansion at any order of approximation.

2. Galappatti's approach does not actually lead to a differential equation for the depth averaged concentration. In fact, we show that, if the boundary condition is expanded in powers of the small parameter, rather than deriving a differential equation for the depth averaged concentration one finds a sequence of higher order corrections for the depth averaged concentration expressed in terms of spatial and temporal derivatives of the leading order solution.

Such revisitation of Galappatti's approach then suggests that, under the assumed slowly varying conditions, the rate of transport of suspended sediment can be expressed in terms of its local and instantaneous equilibrium

value corrected by terms proportional to spatial and temporal derivatives of such equilibrium solution. This approach which appears to be simpler than Galappatti's [1983] approach, is pursued in Sect. 1.3 where we derive a relationship for the flux of suspended sediment appropriate to slowly varying flows.

The rest of the chapter proceeds as follows. In the next section we investigate two model problems which are amenable to simple analytical treatment, providing a simple context where we can demonstrate the main ideas outlined above. Sect. 1.3 is devoted to the derivation of an asymptotic expansion for the solution of the actual problem of transport of suspended sediment; an analytic relationship appropriate to slowly varying flows is derived for the flux of suspended sediment. Sect. 1.4 applies the latter formulation to the problem of transport of suspended sediments by flood waves, while some conclusions follow in the last section.

1.2 Analysis of two Model Problems.

1.2.1 The first model problem.

Let us consider the following partial differential problem:

$$f_{,zz} + f_{,z} = \delta f_{,\tau} \ , \tag{1.1a}$$

$$f_{,z} + f = 0 \qquad (z = 1) \ , \tag{1.1b}$$

$$f = a \exp(i\omega\tau) \qquad (z = 0) \ , \tag{1.1c}$$

where $f(z, \tau)$ is a function of the spatial coordinate z defined in the range [0,1] and of a temporal coordinate τ defined in $[0, \infty)$. Note that the left hand side of (1.1a) provides a simplified model of turbulent diffusion and gravitational settling while the right hand side models the unsteady term of the advection diffusion equation. The boundary conditions (1.1b, 1.1c) similarly model the actual boundary condition of the suspended sediment problem for periodic flows.

Exact periodic solution

The exact periodic solution of the latter problem is readily obtained by setting:

$$f = F(z) \exp(i\omega\tau) \ . \tag{1.2}$$

Substituting from (1.2) into the equations (1.1) one finds:

$$F(z) = aK \left[(1 + \lambda_1) \exp(\lambda_1 + \lambda_2 z) - (1 + \lambda_2) \exp(\lambda_2 + \lambda_1 z) \right] \ , \tag{1.3}$$

where

$$K = [(1+\lambda_1)\exp(\lambda_1) - (1+\lambda_2)\exp(\lambda_2)]^{-1} \ , \tag{1.4a}$$

$$\lambda_{1,2} = \frac{1}{2}\left(-1 \pm \sqrt{1+4i\delta\omega}\right) \ . \tag{1.4b}$$

Formal perturbation solution for the case $\delta << 1$

In the weakly forced case ($\delta << 1$) a formal perturbation solution of the differential system (1.1) is obtained by expanding the function f in powers of the small parameter δ in the form:

$$f = f_0 + \delta f_1 + \delta^2 f_2 + O(\delta^3) \ . \tag{1.5}$$

By substituting from the latter expansion into the differential problem (1.1) and equating likewise powers of δ we find a sequence of differential problems at the various orders of approximation:

$\boxed{O(\delta^n)}$

$$f_{n,zz} + f_{n,z} = b_n \ , \tag{1.6a}$$

$$f_{n,z} + f_n = 0 \qquad (z=1) \ , \tag{1.6b}$$

$$f_n = d_n \qquad (z=0) \ , \tag{1.6c}$$

where $n = 0, 1, 2, ...$ and

$$b_0 = 0, \ b_n = f_{n-1,\tau} \qquad (n \geq 1) \ , \tag{1.7a}$$

$$d_0 = a\exp(i\omega\tau), \ d_n = 0 \qquad (n \geq 1) \ . \tag{1.7b}$$

The periodic solution of the above systems is obtained recursively and reads:

$$f_0 = a\exp(-z + i\omega\tau) \ , \tag{1.8}$$

$$f_1 = i\frac{\omega}{e} a\exp(i\omega\tau)\left\{1 - (1+ze)\exp(-z)\right\} \ , \tag{1.9}$$

$$f_2 = -\frac{\omega^2}{e} a\exp(i\omega\tau)\left\{\left(z - \frac{1}{e} - 4\right)\right. \tag{1.10}$$

$$\left. + \left[z + \frac{1}{e} + 4 + ze\left(1 + \frac{z}{2}\right)\right]\exp(-z)\right\} \ , \tag{1.11}$$

where $e = \exp(1)$.

Galappatti's solution

Galappatti's approach can be applied to the differential problem (1.1) by setting an expansion identical to (1.5), say:

$$f = f_0^G + \delta f_1^G + \delta^2 f_2^G + O(\delta^3) \ . \tag{1.12}$$

Such expansion is applied to the differential equation (1.1a) and the boundary condition (1.1b), while the lower boundary condition (1.1c) is replaced by the following integral conditions:

$$\int_0^1 f_0^G dz = F_0^G(\tau) \, , \ \int_0^1 f_n^G dz = 0 \ , \quad (n \geq 1) \tag{1.13}$$

where F_0^G is the 'depth averaged' value of f, as yet unknown. Replacing the boundary conditions (1.6c) by the latter integral conditions (1.13), the differential system (1.6) is again solved recursively to give:

$$f_0^G = \frac{e}{e-1} \exp(-z) F_0^G(\tau) \ , \tag{1.14}$$

$$f_1^G = \frac{e}{e-1} \left[\frac{1}{e} + \frac{3-e}{1-e} \exp(-z) - z \exp(-z) \right] \frac{dF_0^G}{d\tau} \ . \tag{1.15}$$

Galappatti's approach then proceeds by applying the boundary condition (1.1c) to the above solution, hence:

$$\frac{e}{e-1} \left\{ F_0^G(\tau) + \delta \left[\frac{1}{e} + \frac{3-e}{1-e} \right] \frac{dF_0^G}{d\tau} + O\left(\delta^2\right) \right\} = a \exp(i\omega\tau) \ . \tag{1.16}$$

The periodic solution of the latter equation is obtained in closed form and reads:

$$F_0^G(\tau) = \frac{a(e-1)^2}{e(e-1) - \delta i\omega (1 + 2e - e^2)} \exp(i\omega\tau) \ . \tag{1.17}$$

Comparison among solutions

Let us first analyze Galappatti's solution in the light of the formal asymptotic solution. A glance at the form of the function F_0^G reveals that it can be expanded in powers of δ, i.e. it is an $O(1)$ quantity which however contains smaller contributions of any order in δ. This feature shows that the 'leading order' component of Galappatti's solution f_0^G actually includes part of the higher order components of the solution. Expanding F_0^G in powers of δ, one readily finds:

$$F_0^G = F_{00}^G + \delta F_{01}^G + O(\delta^2) \ , \tag{1.18}$$

where

$$F_{00}^G = \frac{e-1}{e} a \exp(i\omega\tau) \ , \tag{1.19}$$

$$F_{01}^G = F_{00}^G \left[i\omega \ \frac{1+2e-e^2}{e\,(e-1)} \right] \ . \tag{1.20}$$

The reader will check that, using such results in the expansion for f^G one may rewrite the latter in the form:

$$f^G = f_{00}^G + \delta \left[f_{10}^G + f_{01}^G \right] + O(\delta^2) \ , \tag{1.21}$$

where

$$f_{00}^G = \frac{e}{e-1} \exp(-z) F_{00}^G(\tau) \equiv f_0 \ , \tag{1.22}$$

$$\begin{aligned} f_{10}^G + f_{01}^G &= \frac{e}{e-1} \left[\frac{1}{e} + \left(\frac{3-e}{1-e} - z \right) \exp(-z) \right] \frac{dF_{00}^G}{d\tau} \\ &\quad + \frac{e}{e-1} \exp(-z) F_{01}^G(\tau) \\ &= i\frac{\omega}{e} a \left\{ 1 - (1+ze) \exp(-z) \right\} \exp(i\omega\tau) \equiv f_1 \ . \end{aligned} \tag{1.23}$$

In other words if one expands the function F_0^G in powers of δ and the Galappatti's expansion is formally rearranged, then it can be made to coincide with the formal asymptotic expansion.

A second feature reveals the need to reinterpret Galappatti's approach. In fact, the relationship for the depth averaged quantity F_0^G is treated by that author as a differential equation for F_0^G since it includes a contribution proportional to the first order derivative of F_0^G. However, if the expansion were carried out to higher order, say order n, such differential equation would be of $n-th$ order, hence it would require $(n-1)$ initial conditions whose nature is unclear. Such dilemma is readily resolved if one recognizes that formal consistency calls for a perturbation expansion of the solution for F_0^G in powers of δ, as shown above: then, the determination of F_0^G does not require to solve an $n-th$ order differential equation. Rather, higher order corrections for F_0^G are derived in terms of the derivatives of the leading order solution $d^j F_0^G / d\tau^j \quad (j = 1, 2, ...)$.

Figure (1.1) shows a comparison between the real parts of the exact solution, the formal asymptotic expansion truncated at leading order or at first order and Galappatti's solution. In the present case, it appears that the latter is uniformly less accurate than the second order approximation of the

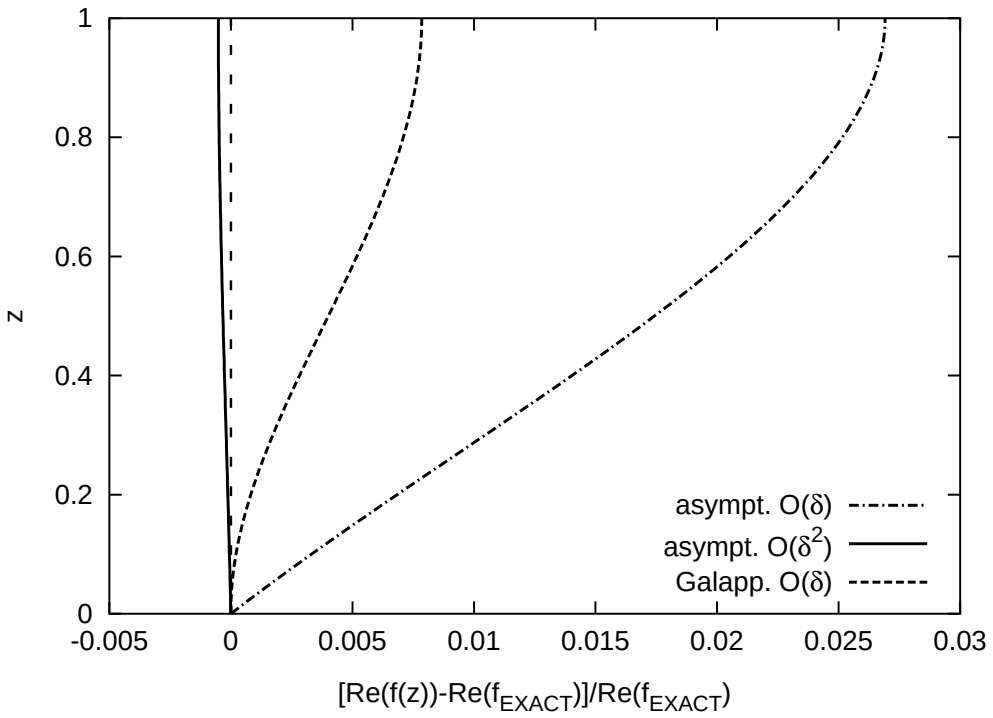

Figure 1.1: Comparison between the real parts of the exact solution, the formal asymptotic expansion truncated at leading order or at first order and Galappatti's solution. ($\delta = 0.5, \tau = 0$)

exact solution, but more accurate than the first order approximation. This is not surprising in the light of the previous discussion, as we have shown that the leading order solution of Galappatti is only apparently of order δ, it rather hides higher order contributions in the depth averaged quantity F_0^G. From the latter results one might be tempted to conclude that the leading order solution of Galappatti can be safely employed as a useful tool which provides an answer 'more accurate' than that provided by the $O(\delta)$ formal asymptotic solution. However, such conclusion would be incorrect: the next model problem will show that the higher order contributions hidden in the leading order solution of Galappatti, may make the latter less accurate than the formal asymptotic solution even at $O(\delta)$.

1.2.2 The second model problem.

Let us consider the following partial differential problem:

$$f_{,zz} + f_{,z} = \delta f \exp(ix) \ , \tag{1.24a}$$

$$f_{,z} + f = 0 \qquad (z = 1) \ , \tag{1.24b}$$

$$f = 1 \qquad (z = 0) \ , \tag{1.24c}$$

where δ is a small parameter and $f(z,x)$ is a function of the spatial coordinate z defined in the range [0,1] and of a spatial coordinate x defined in $(-\infty, \infty)$. Note that the left hand side of (1.24a) provides a simplified model of turbulent diffusion and gravitational settling while the right hand side models the advective term of the advection diffusion equation for spatially periodic flows. The boundary conditions (1.24b, 1.24c) similarly model the actual boundary condition of the suspended sediment problem.

Exact periodic solution

The exact periodic solution of the latter problem is readily obtained and reads:

$$f\,(z,x) = K\left[(1+\lambda_1)\exp(\lambda_1 + \lambda_2 z) - (1+\lambda_2)\exp(\lambda_2 + \lambda_1 z)\right] \ , \tag{1.25}$$

where

$$\lambda_{1,2} = \frac{1}{2}\left(-1 \pm \sqrt{1 + 4\delta\exp(ix)}\right) \ , \tag{1.26}$$

and K reads

$$K = \left[(1+\lambda_1)\exp(\lambda_1) - (1+\lambda_2)\exp(\lambda_2)\right]^{-1} \ . \tag{1.27}$$

Formal perturbation solution for the case $\delta << 1$

In the weakly forced case ($\delta << 1$) a formal perturbation solution of the differential system (1.24) is obtained by expanding the function f in powers of the small parameter δ in the form:

$$f = f_0 + \delta f_1 + \delta^2 f_2 + O(\delta^3) \ . \tag{1.28}$$

By substituting from the latter expansion into the differential problem (1.24) and equating likewise powers of δ we find a sequence of differential problems at the various orders of approximation:

$\boxed{O(\delta^n)}$

$$f_{n,zz} + f_{n,z} = b_n \ , \tag{1.29a}$$

$$f_{n,z} + f_n = 0 \qquad (z = 1) \ , \tag{1.29b}$$

$$f_n = d_n \qquad (z = 0)\ , \tag{1.29c}$$

where $n = 0, 1, 2, ...$ and

$$b_0 = 0,\ b_n = f_{n-1}\exp(ix) \qquad (n \geq 1)\ , \tag{1.30a}$$
$$d_0 = 1,\ d_n = 0 \qquad (n \geq 1)\ . \tag{1.30b}$$

The periodic solution of the above systems is obtained recursively and reads:

$$f_0 = \exp(-z)\ , \tag{1.31}$$
$$f_1 = \frac{1}{e}\exp(ix)\left\{1 - (1 + ze)\exp(-z)\right\}\ , \tag{1.32}$$
$$f_2 = \frac{1}{e}\exp(i2x) \left\{\left(z - \frac{1}{e} - 4\right) + \left[z + \frac{1}{e} + 4 + ze\left(1 + \frac{z}{2}\right)\right]\exp(-z)\right\}\ . \tag{1.33}$$

Galappatti's solution

Galappatti's approach can be applied to the differential problem (1.24) by setting an expansion identical to (1.28), say:

$$f^G = f_0^G + \delta f_1^G + \delta^2 f_2^G + O(\delta^3)\ . \tag{1.34}$$

Such expansion is applied to the differential equation (1.24a) and the boundary condition (1.24b), while the lower boundary condition (1.24c) is replaced by the following integral conditions:

$$\int_0^1 f_0^G dz = F_0^G(x)\,, \qquad \int_0^1 f_n^G dz = 0 \qquad (n \geq 1)\ , \tag{1.35}$$

where F_0^G is the 'depth averaged' value of f^G, as yet unknown. Replacing the boundary conditions (1.29c) by the latter integral conditions (1.35), the differential system (1.29) is again solved recursively to give:

$$f_0^G = \frac{e}{e-1}\exp(-z)F_0^G(x)\ , \tag{1.36}$$
$$f_1^G = \frac{e}{e-1}\exp(ix)\left\{\frac{1}{e} + \left[\frac{3-e}{1-e} - z\right]\exp(-z)\right\}F_0^G(x)\ . \tag{1.37}$$

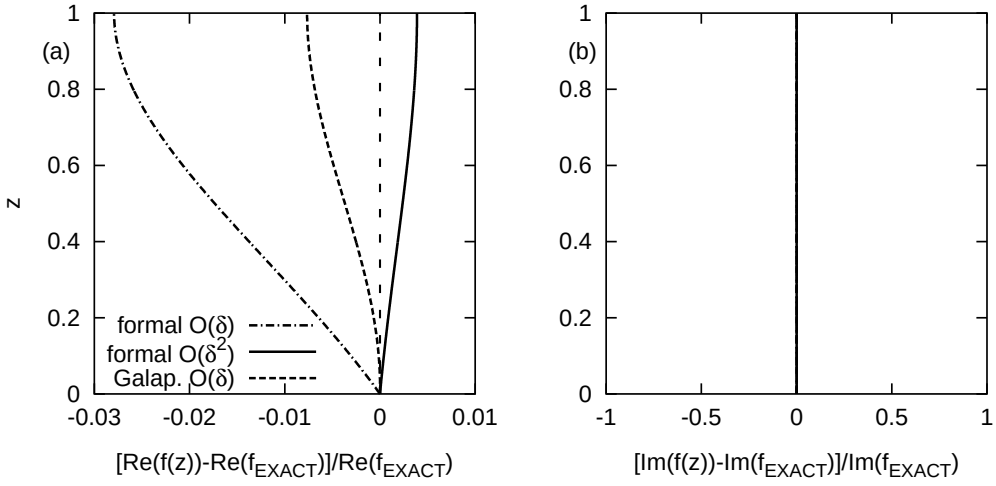

Figure 1.2: Comparison between the [real (a), imaginary (b)] part of the exact solution, the formal asymptotic expansion truncated at leading order or at first order and Galappatti's solution ($\delta = 0.5,\ x = 0$).

Galappatti's approach then proceeds by applying the boundary condition (1.24c) to the above solution, hence:

$$\frac{e}{e-1} F_0^G(x) \left\{ 1 + \delta \left[\frac{1}{e} + \frac{3-e}{1-e} \right] \exp(ix) + O\left(\delta^2\right) \right\} = 1 \ . \tag{1.38}$$

The periodic solution of the latter equation is obtained in closed form and reads:

$$F_0^G(x) = \frac{(e-1)^2}{e(e-1) - \delta\left(1 + 2e - e^2\right)\exp(ix)} \ . \tag{1.39}$$

Comparison among solutions

Figures 1.2, 1.3, 1.4 show a comparison between the exact solution, the formal asymptotic expansion truncated at leading order or at first order and Galappatti's solution for different values of x. From Figures 1.2, representing the situation at $x = 0$, it appears that Galappatti's solution is uniformly less accurate than the second order approximation of the exact solution, but more accurate than the first order approximation. Figures 1.3 show that the higher order contributions hidden in the leading order solution of Galappatti, may make the latter less accurate than the formal asymptotic solution

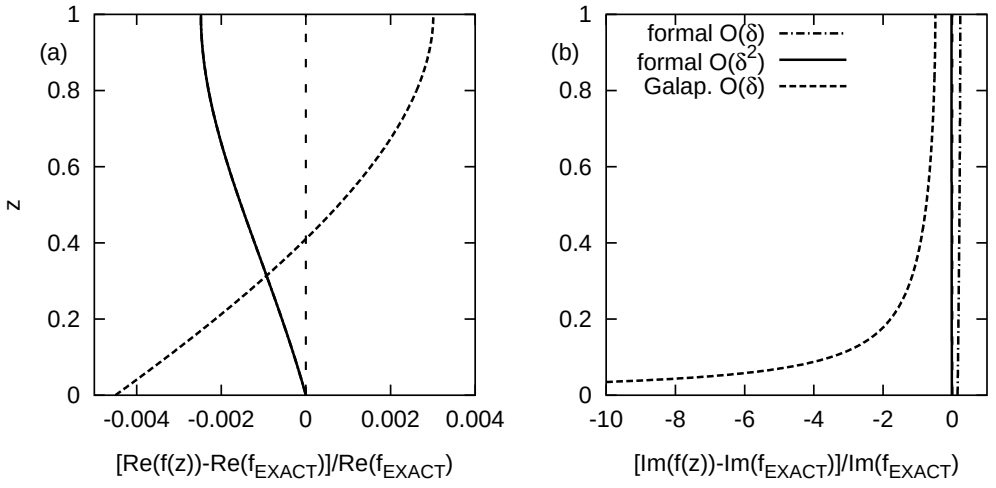

Figure 1.3: Comparison between the [real (a), imaginary (b)] part of the exact solution, the formal asymptotic expansion truncated at leading order or at first order and Galappatti's solution ($\delta = 0.5,\ x = \pi/4$).

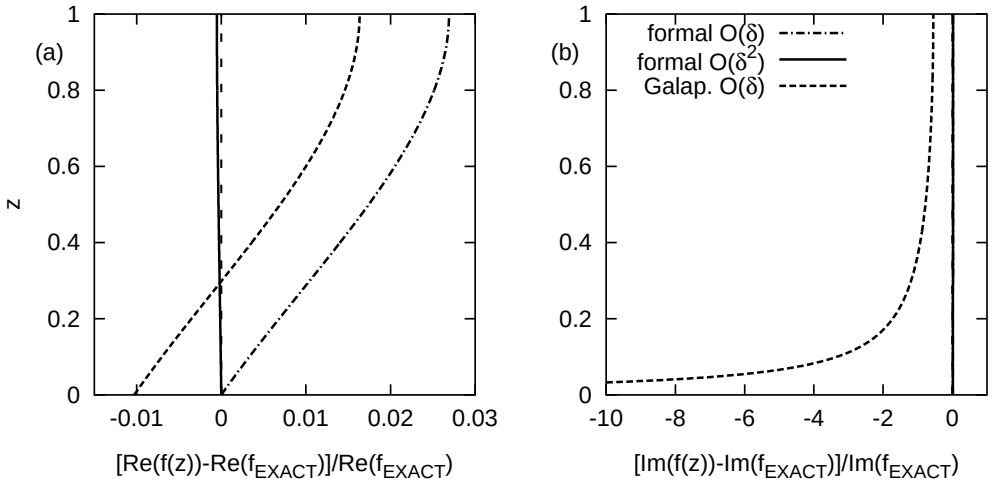

Figure 1.4: Comparison between the [real (a), imaginary (b)] part of the exact solution, the formal asymptotic expansion truncated at leading order or at first order and Galappatti's solution ($\delta = 0.5,\ x = \pi/2$).

at $O(\delta)$. Notice also the low accuracy of the solution of Galappatti near the bed both in its real and imaginary parts. The same picture arises in Figures 1.4. In the light of our previous discussion, we can easily interpret the latter findings: the accuracy of Galappatti's solution is not known a priori as the quantity F_0^G contains contributions of any order in δ.

1.3 Transport of Suspended Sediment by Slowly Varying Flows.

1.3.1 Formulation of the problem

Let us now consider the flow of a dilute mixture of water and fine sediment particles and refer the flow field to a cartesian coordinate system (x^*, y^*, z^*) with z^* vertical, x^* longitudinal and y^* transverse (hereafter a superscript asterisk will denote a dimensional quantity subsequently made dimensionless). The transport of suspended sediment under gravity is then governed by the convection-diffusion equation which reads:

$$\frac{\partial C}{\partial t^*} + U^* \frac{\partial C}{\partial x^*} + V^* \frac{\partial C}{\partial y^*} + W^* \frac{\partial C}{\partial z^*} - W_s \frac{\partial C}{\partial z^*} = \frac{\partial}{\partial x^*}\left(\mathcal{D}_x^* \frac{\partial C}{\partial x^*}\right) + \frac{\partial}{\partial y^*}\left(\mathcal{D}_y^* \frac{\partial C}{\partial y^*}\right) + \frac{\partial}{\partial z^*}\left(\mathcal{D}_z^* \frac{\partial C}{\partial z^*}\right) , \qquad (1.40)$$

where

C	: local volumetric sediment concentration;
(U^*, V^*, W^*)	: longitudinal, transverse and vertical components of the local velocity;
t^*	: time;
W_s	: particle fall velocity;
$(\mathcal{D}_x^*, \mathcal{D}_y^*, \mathcal{D}_z^*)$	: longitudinal, transverse and vertical components of the eddy diffusivity.

For the sake of simplicity we restrict our attention to the case of plane flows such that the convection-diffusion equation (1.40) reduces to the form:

$$\frac{\partial C}{\partial t^*} + U^* \frac{\partial C}{\partial x^*} + W^* \frac{\partial C}{\partial z^*} - W_s \frac{\partial C}{\partial z^*} = \frac{\partial}{\partial x^*}\left(\mathcal{D}_x^* \frac{\partial C}{\partial x^*}\right) + \frac{\partial}{\partial z^*}\left(\mathcal{D}_z^* \frac{\partial C}{\partial z^*}\right) \qquad (1.41)$$

Let us make the relevant physical quantities dimensionless as follows:

$$t = \omega t^*, \qquad (U, W) = \left(\frac{U^*}{U_0^*}, \frac{W^*}{W_0^*}\right),$$

$$x = \frac{x^*}{L_0^*}, \qquad z = \frac{z^*}{D_0^*}, \qquad (\mathcal{D}_x, \mathcal{D}_z) = \frac{(\mathcal{D}_x^*, \mathcal{D}_z^*)}{u_{*0} D_0^*} \ , \tag{1.42}$$

having employed the following scales:

ω	: typical frequency of the flow field;
U_0^*	: longitudinal velocity scale;
$W_0^* = D_0^* U_0^* / L_0^*$	: scale for vertical velocity;
L_0^*	: longitudinal spatial scale;
D_0^*	: reference flow depth;
u_{*0}	: reference friction velocity.

Note that the scale for the vertical velocity arises from the equation of continuity. Using the above dimensionless variables the equation (1.41) takes the form

$$\delta_1 \frac{\partial C}{\partial t} + \delta_2 U \frac{\partial C}{\partial x} + (\delta_2 W - 1) \frac{\partial C}{\partial z} = \frac{1}{k Z_0} \left[\frac{\partial}{\partial z} \left(\mathcal{D}_z \frac{\partial C}{\partial z} \right) + \delta_3 \frac{\partial}{\partial x} \left(\mathcal{D}_x \frac{\partial C}{\partial x} \right) \right], \tag{1.43}$$

where the following dimensionless parameters arise:

$$\delta_1 = \frac{\omega D_0^*}{W_s}, \quad \delta_2 = \frac{U_0^* D_0^*}{W_s L_0^*}, \quad \delta_3 = \left(\frac{D_0^*}{L_0^*} \right)^2, \quad Z_0 = \frac{W_s}{k u_{*0}} \ . \tag{1.44}$$

In (1.43,1.44) k is the von Karman constant and Z_0 is the reference Rouse number. Note that the parameters $\delta_j (j = 1, 3)$ are typically small for slowly varying flows like tidal flows [*Lanzoni and Seminara*, 2002] and flood waves. In particular, δ_3 is usually much smaller than δ_1 and δ_2 and, therefore, the second term in square brackets in (1.43) can be neglected.
Let us define a transformed vertical coordinate ζ as follows:

$$\zeta = \frac{z^* - \eta^*}{D^*} = \frac{1}{D} (z - \eta) \ , \tag{1.45}$$

where

$$D = \frac{D^* (x^*, t^*)}{D_0^*} = D (x, t) \ , \tag{1.46}$$

$$\eta = \frac{\eta^* (x^*, t^*)}{D_0^*} = \eta (x, t) \ , \tag{1.47}$$

and η is the dimensionless bottom elevation. It should be noted that, ζ being dependent on x and t, it follows that:

$$\frac{\partial}{\partial z} \rightarrow \frac{1}{D}\frac{\partial}{\partial \zeta} \,, \tag{1.48a}$$

$$\frac{\partial}{\partial x} \rightarrow \frac{\partial}{\partial x} + \frac{\partial \zeta}{\partial x}\frac{\partial}{\partial \zeta} = \frac{\partial}{\partial x} + \left[-\frac{1}{D}\left(\frac{\partial \eta}{\partial x} + \zeta \frac{\partial D}{\partial x}\right)\right]\frac{\partial}{\partial \zeta} \,, \tag{1.48b}$$

$$\frac{\partial}{\partial t} \rightarrow \frac{\partial}{\partial t} + \frac{\partial \zeta}{\partial t}\frac{\partial}{\partial \zeta} = \frac{\partial}{\partial t} + \left[-\frac{1}{D}\left(\frac{\partial \eta}{\partial t} + \zeta \frac{\partial D}{\partial t}\right)\right]\frac{\partial}{\partial \zeta} \,. \tag{1.48c}$$

Setting

$$\delta_2 = \delta, \qquad \delta_1 = \gamma\delta \quad (\gamma \sim O(1)) \,, \tag{1.49}$$

employing the transformations (1.48) and neglecting the term proportional to δ_3, the convection-diffusion equation (1.43) becomes:

$$\begin{aligned} &\frac{1}{kZ_0}\left[\frac{\partial}{\partial \zeta}\left(\mathcal{D}_\zeta \frac{\partial C}{\partial \zeta}\right)\right] + D\frac{\partial C}{\partial \zeta} = \\ &\delta\left\{\gamma D^2 \frac{\partial C}{\partial t} - \gamma D\left(\frac{\partial \eta}{\partial t} + \zeta \frac{\partial D}{\partial t}\right)\frac{\partial C}{\partial \zeta}\right. \\ &\left. + D^2 U \frac{\partial C}{\partial x} - UD\left(\frac{\partial \eta}{\partial x} + \zeta \frac{\partial D}{\partial x}\right)\frac{\partial C}{\partial \zeta} + DW\frac{\partial C}{\partial \zeta}\right\} \,. \end{aligned} \tag{1.50}$$

The boundary conditions to be associated with equation (1.50) impose vanishing sediment flux at the free surface. Furthermore at the bed we impose the so called 'gradient boundary condition' which essentially consists of an entrainment assumption whereby the net sediment flux is assumed to be proportional to the difference between the actual local instantaneous concentration and the value that concentration would attain at equilibrium with the local and instantaneous flow conditions, the proportionality constant, i.e. the entrainment coefficient, being equal to the particle velocity normal to the bed. The resulting form of the boundary conditions reads:

$$\frac{\mathcal{D}_\zeta}{kZ_0}\frac{\partial C}{\partial \zeta} + DC = \delta\left\{DWC - DUC\frac{\partial h}{\partial x}\right\} \quad (\zeta = 1) \,, \tag{1.51a}$$

$$\frac{\mathcal{D}_\zeta}{kZ_0}\frac{\partial C}{\partial \zeta} + DC_e = \delta\left\{DWC - DUC\frac{\partial \eta}{\partial x}\right\} \quad (\zeta = \zeta_R) \,, \tag{1.51b}$$

where h is the free surface elevation made dimensionless as follows:

$$h\,(x,t) = \frac{h^*\,(x,t)}{D_0^*} \,. \tag{1.52}$$

Moreover, ζ_R is the conventional dimensionless value of the reference elevation where the boundary condition is imposed under uniform conditions. Several empirical expressions for C_e and ζ_R are available in the literature. They correlate C_e with a dimensionless measure of the bottom stress, the so called Shields parameter ϑ, and with the particle Reynolds number R_p, which read

$$\vartheta = \frac{\tau^*}{(\varrho_s - \varrho)\, g d_s^*}, \qquad R_p = \frac{\sqrt{(s-1)\, g d_s^{*3}}}{\nu} \ , \tag{1.53}$$

where τ^* is the local and instantaneous component of the tangential stress acting at the bottom, d_s^* and ϱ_s are diameter and density of sediment particles assumed to be uniform respectively, s is the relative density ϱ_s/ϱ, ν is the kinematic viscosity of the fluid phase and g is gravity.

A closure relation for the eddy diffusivity $\mathcal{D}_\zeta$ is also required and, assuming slow time variations of the flow field consisting of a quasi-steady sequence of equilibrium states, we can write

$$\mathcal{D}_\zeta = D \frac{u_*}{u_{*0}} N(\zeta) \ , \tag{1.54}$$

with u_* the instantaneous value of friction velocity and $N(\zeta)$ the vertical distribution of eddy diffusivity at equilibrium. Using the classical parabolic distribution for $N(\zeta)$ we write:

$$N(\zeta) = k\zeta(1-\zeta) \ . \tag{1.55}$$

In the case of plane flows, the continuity equation for the flow field reads:

$$\frac{\partial U^*}{\partial x^*} + \frac{\partial W^*}{\partial z^*} = 0 \ . \tag{1.56}$$

We make the above relation dimensionless using the scales introduced previously (1.42), employing the transformations (1.48), and perform depth integration to obtain:

$$W = \left(\frac{\partial \eta}{\partial x} + \zeta \frac{\partial D}{\partial x}\right) U - \frac{\partial D}{\partial x} \int_{\zeta_0}^{\zeta} U(\xi)\, d\xi - D \int_{\zeta_0}^{\zeta} \frac{\partial U}{\partial x}\, d\xi \ . \tag{1.57}$$

Assuming a self similar structure of the velocity field appropriate to slowly varying flows, we can write

$$U = \overline{U}(x,t)\ F(\zeta) \ , \tag{1.58a}$$

$$F(\zeta) = \frac{\sqrt{C_{f0}}}{k}\left(\ln\frac{\zeta}{\zeta_0} + A\zeta^2 + B\zeta^3\right), \quad A = 1.84, \quad B = -1.56 \ ,$$

(1.58b)

where C_{f0} represents the friction coefficient at the reference state (defined by $\overline{U}(x,t)=1$) and ζ_0 is the conventional dimensionless value of the reference elevation for no slip in uniform flows. With the aid of (1.58) the vertical component of the velocity (1.57) takes the form

$$W=\left(\frac{\partial\eta}{\partial x}+\zeta\frac{\partial D}{\partial x}\right)U+\gamma\frac{\partial D}{\partial t}G(\zeta)\ , \tag{1.59}$$

where

$$G(\zeta)=\int_{\zeta_0}^{\zeta}F(\xi)\,d\xi\ , \tag{1.60}$$

and we have employed the dimensionless 1D form of the mass balance equation for the flow field, which reads:

$$\gamma\frac{\partial D}{\partial t}+\frac{\partial\left(D\overline{U}\right)}{\partial x}=0\ . \tag{1.61}$$

Substituting from (1.54) and (1.59) into (1.50, 1.51) we obtain the following final form of the differential problem:

$$\frac{1}{kZ}\left[\frac{\partial}{\partial\zeta}\left(N(\zeta)\frac{\partial C}{\partial\zeta}\right)\right]+\frac{\partial C}{\partial\zeta}= \\ \delta\left\{\gamma D\frac{\partial C}{\partial t}+DU\frac{\partial C}{\partial x}+\left[\left(\frac{\partial D}{\partial t}\right)G(\zeta)-\left(\frac{\partial\eta}{\partial t}+\zeta\frac{\partial D}{\partial t}\right)\right]\gamma\frac{\partial C}{\partial\zeta}\right\}\ , \tag{1.62}$$

$$\frac{N(\zeta)}{kZ}\frac{\partial C}{\partial\zeta}+C=\delta\left\{\gamma C\frac{\partial D}{\partial t}\right\}\qquad(\zeta=1)\ , \tag{1.63}$$

$$\frac{N(\zeta)}{kZ}\frac{\partial C}{\partial\zeta}+C_e=\delta\left\{\zeta UC\frac{\partial D}{\partial x}+\gamma C\frac{\partial D}{\partial t}G(\zeta)\right\}\qquad(\zeta=\zeta_R)\ . \tag{1.64}$$

Condition (1.64) can be further simplified if one neglects the longitudinal velocity U and the integral $G(\zeta)$ both evaluated at the reference height ζ_R. With these assumptions the right hand side of (1.64) vanishes.

1.3.2 Formal perturbation solution for the case $\delta << 1$.

Following the same line of reasoning introduced in Section 1.2, a formal perturbation solution of the differential equation (1.62), associated with the boundary conditions (1.63, 1.64), can be obtained by expanding the concentration C in powers of the small parameter δ in the form:

$$C=C_0(\zeta,x,t)+\delta C_1(\zeta,x,t)+O(\delta^2)\ . \tag{1.65}$$

By substituting from the latter expansion into the differential problem (1.62, 1.63, 1.64) and equating likewise powers of δ we find a sequence of differential problems at the various orders of approximation.

At the leading order we find the following differential system

$\boxed{O(\delta^0)}$

$$\frac{1}{kZ}\left[\frac{\partial}{\partial\zeta}\left(N(\zeta)\frac{\partial C_0}{\partial\zeta}\right)\right]+\frac{\partial C_0}{\partial\zeta}=0\ , \tag{1.66a}$$

$$\frac{1}{kZ}\left(N(\zeta)\frac{\partial C_0}{\partial\zeta}\right)+C_0=0 \qquad (\zeta=1)\ , \tag{1.66b}$$

$$-\frac{1}{kZ}\left(N(\zeta)\frac{\partial C_0}{\partial\zeta}\right)=C_e \qquad (\zeta=\zeta_R)\ , \tag{1.66c}$$

which leads to the classical Rouse solution:

$$C_0=\overline{C}_0(x,t)\ \ \phi_0(\zeta,\vartheta,R_p)\ \ , \tag{1.67}$$

where

$$\overline{C}_0(x,t)=C_e(\vartheta,R_p)\ \ I(\vartheta,R_p)\ \ , \tag{1.68}$$

$$I(\vartheta,R_p)=\frac{1}{1-\zeta_R}\int_{\zeta_R}^{1}\left(\frac{1-\zeta}{1-\zeta_R}\ \frac{\zeta_R}{\zeta}\right)^Z d\zeta\ , \tag{1.69}$$

$$\phi_0(\zeta,\vartheta,R_p)=\frac{1}{I(\vartheta,R_p)}\left(\frac{1-\zeta}{1-\zeta_R}\ \frac{\zeta_R}{\zeta}\right)^Z\ . \tag{1.70}$$

At the following order of approximation we then find

$\boxed{O(\delta)}$

$$\begin{aligned}&\frac{1}{kZ}\left[\frac{\partial}{\partial\zeta}\left(N(\zeta)\frac{\partial C_1}{\partial\zeta}\right)\right]+\frac{\partial C_1}{\partial\zeta}=\gamma D\frac{\partial C_0}{\partial t}+\overline{U}DF(\zeta)\frac{\partial C_0}{\partial x}\\&+\left[\left(\frac{\partial D}{\partial t}\right)G(\zeta)-\left(\frac{\partial\eta}{\partial t}+\zeta\frac{\partial D}{\partial t}\right)\right]\gamma\frac{\partial C_0}{\partial\zeta}\ ,\end{aligned} \tag{1.71a}$$

$$\frac{1}{kZ}\left(N(\zeta)\frac{\partial C_1}{\partial\zeta}\right)+C_1=0 \qquad (\zeta=1)\ , \tag{1.71b}$$

$$\frac{\partial C_1}{\partial\zeta}=0 \qquad (\zeta=\zeta_R)\ . \tag{1.71c}$$

Neglecting $\phi_{0,x}$ and $\phi_{0,t}$, we can write

$$\frac{\partial C_0}{\partial t}=\phi_0(\zeta)\frac{\partial\overline{C}_0}{\partial t}\ , \tag{1.72a}$$

$$\frac{\partial C_0}{\partial x} = \phi_0(\zeta)\frac{\partial \overline{C}_0}{\partial x} , \tag{1.72b}$$

$$\frac{\partial C_0}{\partial \zeta} = \overline{C}_0\frac{\partial \phi_0(\zeta)}{\partial \zeta} . \tag{1.72c}$$

Recalling the structure of the forcing terms in the right hand side of (1.71a) and the expressions (1.72), the solution for C_1 can then be written in the form

$$\begin{aligned} C_1(\zeta,\vartheta,R_p) &= \gamma D\frac{\partial \overline{C}_0}{\partial t}C_{11} + \overline{U}D\frac{\partial \overline{C}_0}{\partial x}C_{12} - \overline{C}_0\gamma\frac{\partial \eta}{\partial t}C_{13} \\ &\quad + \overline{C}_0\gamma\frac{\partial D}{\partial t}(C_{14}-C_{15}) , \end{aligned} \tag{1.73}$$

where the functions $C_{1j}(j=1,5)$ are solutions of the boundary value problems:

$$LC_{1j} = a_j(\zeta) \qquad (j=1,5) , \tag{1.74}$$

$$BC_{1j} = 0 \qquad (\zeta=1) \qquad (j=1,5) , \tag{1.75}$$

$$\frac{dC_{1j}}{d\zeta} = 0 \qquad (\zeta=\zeta_R) \qquad (j=1,5) , \tag{1.76}$$

with the following definitions of the operators L and B:

$$L = \frac{1}{kZ}\left[\frac{d}{d\zeta}\left(N(\zeta)\frac{d}{d\zeta}\right)\right] + \frac{d}{d\zeta} , \tag{1.77}$$

$$Bf = \frac{1}{kZ}N(\zeta)\frac{df}{d\zeta} + f , \tag{1.78}$$

and

$$\begin{aligned} &a_1 = \phi_0(\zeta) , \qquad a_2 = \phi_0(\zeta)F(\zeta) , \qquad a_3 = \frac{d\phi_0(\zeta)}{d\zeta} , \\ &a_4 = G(\zeta)\frac{d\phi_0(\zeta)}{d\zeta} , \qquad a_5 = \zeta\frac{d\phi_0(\zeta)}{d\zeta}. \end{aligned} \tag{1.79}$$

The boundary value problems (1.74-1.79) were solved numerically by using a shooting technique.

1.3.3 Derivation of an analytical relationship for the suspended sediment flux under slowly varying conditions.

Following the same ideas introduced in Section 1.3.2, we then expand the suspended sediment flux in powers of the small parameter δ in the form

$$q_s = q_{s0} + \delta q_{s1} + O(\delta^2) , \tag{1.80}$$

where q_{s0} and q_{s1} have been made dimensionless as follows:

$$(q_{s0},\ q_{s1}) = \frac{(q^*_{s0},\ q^*_{s1})}{U^*_0 D^*_0}\ . \tag{1.81}$$

With the aid of (1.58a) we can write:

$$\boxed{q_s = q\,(x,t)\,\psi\,(x,t)}\ , \tag{1.82}$$

where

$$q\,(x,t) = \overline{U}\,(x,t)\,D\,(x,t)\ \ , \tag{1.83a}$$

$$\psi\,(x,t) = \int_{\zeta_R}^{1} \left[C_0 + \delta C_1 + O(\delta^2)\right] F\,(\zeta)\,d\zeta = \psi_0 + \delta\psi_1 + O(\delta^2)\ . \tag{1.83b}$$

By susbstituing (1.67) and (1.73) into (1.83b) we end up with the following relationships for ψ_0 and ψ_1

$$\psi_0 = \frac{\sqrt{C_{f0}}}{k} C_e\,[I_{02} + K_1 I_{01}]\ \ , \tag{1.84a}$$

$$\psi_1 = \frac{\sqrt{C_{f0}}}{k}\left[D\frac{\partial \overline{C}_0}{\partial t}\ q_{s11} + \overline{U} D \frac{\partial \overline{C}_0}{\partial x}\ q_{s12} + \frac{\partial \eta}{\partial t}\overline{C}_0\ q_{s13} + \frac{\partial D}{\partial t}\overline{C}_0\ q_{s14}\right]\ , \tag{1.84b}$$

where

$$K_1 = -\ln \zeta_0\ , \tag{1.85}$$

and the integrals $I_{0j} (j = 1,\ 2)$ read

$$I_{01}\,(\zeta_R, Z) = \int_{\zeta_R}^{1} \left(\frac{1-\zeta}{1-\zeta_R}\ \frac{\zeta_R}{\zeta}\right)^Z d\zeta = I\,(\vartheta, R_p)\,(1-\zeta_R)\ \ , \tag{1.86a}$$

$$I_{02}\,(\zeta_R, Z) = \int_{\zeta_R}^{1} \left(\ln\zeta + A\zeta^2 + B\zeta^3\right)\left(\frac{1-\zeta}{1-\zeta_R}\ \frac{\zeta_R}{\zeta}\right)^Z d\zeta\ . \tag{1.86b}$$

Moreover, the coefficients $q_{s1j} (j = 1..4)$ appearing in (1.84b) read

$$q_{s11} = \gamma\,(A_{11} + K_1 A^*_{11})\ \ , \tag{1.87a}$$

$$q_{s12} = (A_{12} + K_1 A^*_{12})\ \ , \tag{1.87b}$$

$$q_{s13} = -\gamma \left(A_{13} + K_1 A^*_{13} \right) \ , \tag{1.87c}$$

$$q_{s14} = \gamma \left(A_{14} + K_1 A^*_{14} - A_{15} - K_1 A^*_{15} \right) \ , \tag{1.87d}$$

where the integrals $A_{1j} (j = 1..5)$ read

$$A_{1j} \left(\zeta_R, Z \right) = \int_{\zeta_R}^{1} C_{1j} \left(\xi, \vartheta, R_p \right) F_1 \left(\xi \right) d\xi \qquad (j = 1, 5) \ , \tag{1.88a}$$

$$A^*_{1j} \left(\zeta_R, Z \right) = \int_{\zeta_R}^{1} C_{1j} \left(\xi, \vartheta, R_p \right) d\xi \qquad (j = 1, 5) \ , \tag{1.88b}$$

and

$$F_1 \left(\zeta \right) = \ln \left(\zeta \right) + A\zeta^2 + B\zeta^3 \ . \tag{1.89}$$

Since the above coefficients (1.86, 1.88) are functions of ζ_R and Z, in order for the relationships (1.82, 1.83, 1.84) to provide a simple tool to be incorporated into morphodynamic numerical models, analytical forms for the latter coefficients have been derived according to the following procedure.

We have calculated numerically each of the above quantities using Simpson's rule for a set of values for ζ_R and Z falling in the ranges:

$$\log \zeta_R \in [-3, -1] \ , \qquad Z \in [0.01, 6.30] \ , \tag{1.90}$$

with steps

$$\Delta \log \zeta_R = 0.05 \ , \qquad \Delta Z = 0.01 \ . \tag{1.91}$$

We then used the calculated values to derive analytical expressions for each coefficient by performing interpolations of the general form

$$P(x, y) = \sum_{i=1}^{7} \sum_{j=1}^{7} p_{ij} x^{i-1} y^{j-1} \ , \tag{1.92}$$

where x is equal to $\log \zeta_R$, y is the Rouse number and the coefficients p_{ij} have been obtained by a least square regression. The values of p_{ij} are not reported here for the sake of brevity but can be made available at request by the author. Figures (1.5a,b) show a sample comparison between the interpolated values of the coefficient I_{01} and the values attained by numerical integration of the integral (1.86a). Note that the relative error of such comparison does never exceed 0.05% (Figure 1.6). With the help of such expressions, equations (1.82, 1.83, 1.84) provide a simple analytical approach to evaluate the flux of suspended sediment in slowly varying flows suitable to applications to a variety of morphodynamic contexts including tidal and fluvial environments.

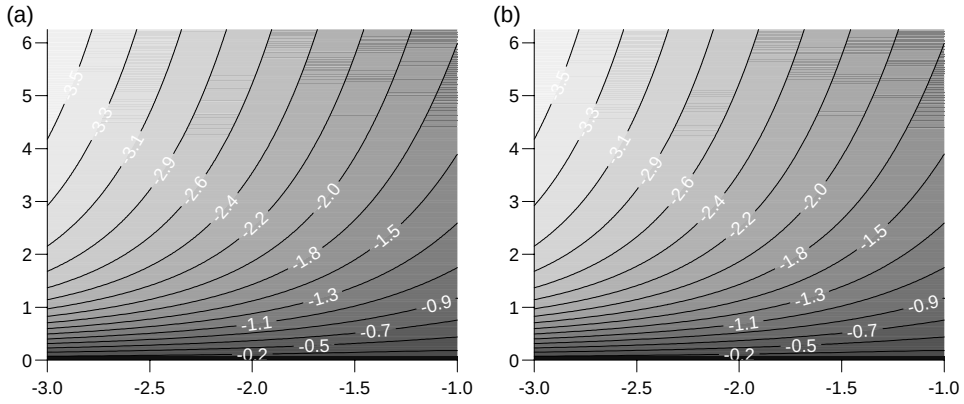

Figure 1.5: Comparison between the interpolated values of the coefficient I_{01} (b) and the values attained by numerical integration of the integral (1.86a) (a). The x axis represents the $\log \zeta_R$, the y axis the Rouse number and the contour levels report the $\log I_{01}$.

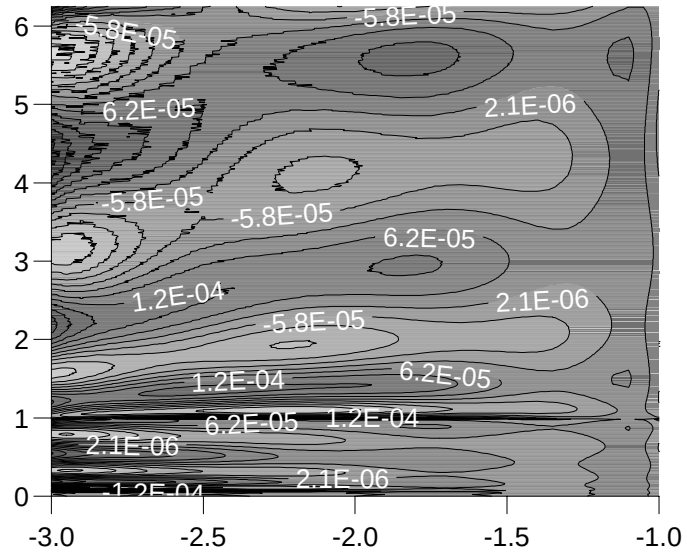

Figure 1.6: Relative error between the interpolated values of the coefficient I_{01} and the values attained by numerical integration of the integral (1.86a).

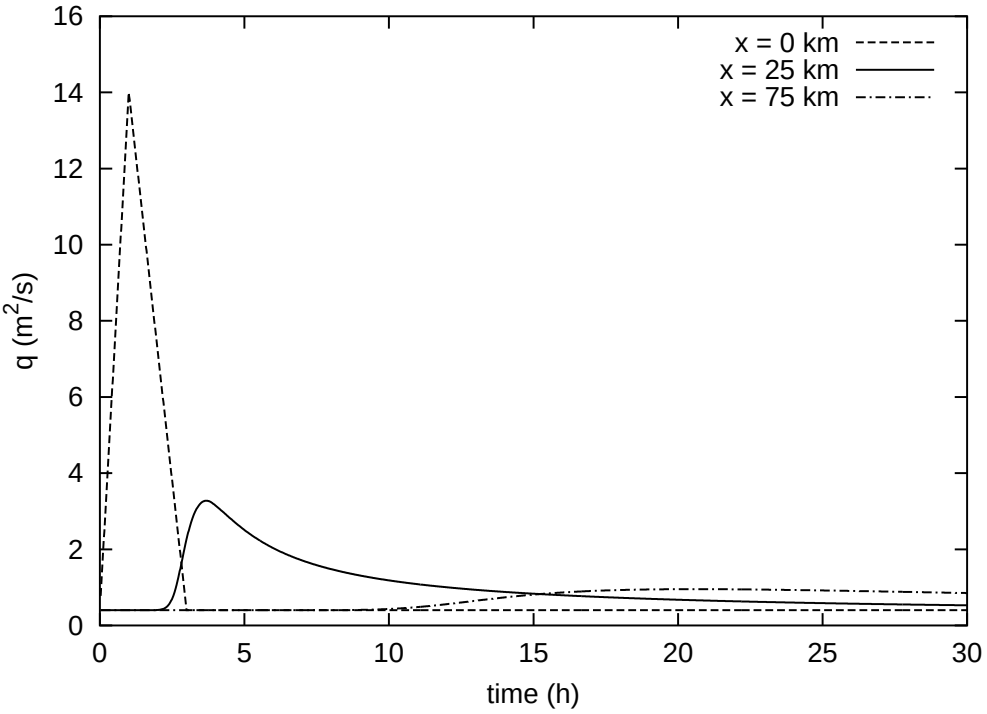

Figure 1.7: Water discharge per unit width at different cross sections.

1.4 Applications to the Problem of Transport of Suspended Sediment by Flood Waves

Various aspects of river management require the ability to predict the tendency of the bed to aggrade or degrade, in response to e.g. the propagation of a flood, the construction of regulation works, the occurrence of meander cutoff, etc. Similar problems are found by engineers dealing with the management of estuaries and lagoons. The new 'equilibrium' configuration of the bed following each of the above events may require many decades to be reached. For such calculations of 'long term' morphodynamic equilibrium the tool developed in the last section is then most suitable to avoid the prohibitively lengthy calculations needed if a 3D model for the transport of suspended sediment is employed and the reach considered is long. The formulation developed in Sect. 1.3 is then applied to the propagation of a flood wave down a 125 km stretch of a straight river with uniform bed slope $5 \cdot 10^{-5}$, 'wide' rectangular cross section and median grain size $d_{50} = 0.075$ mm. A flood wave was generated at the upstream end of the reach (Figure 1.7) and its propagation was computed solving the 1D form of the continuity and momentum equations using an appropriate numerical code based on the classical finite

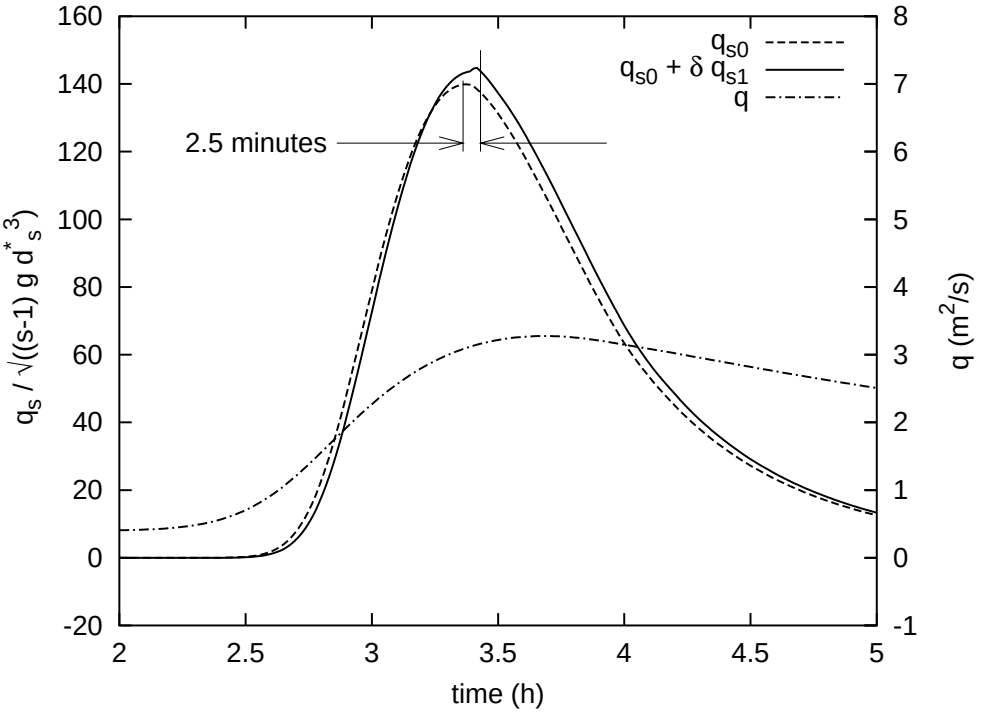

Figure 1.8: Comparison between the dimensionless suspended sediment transport capacity per unit width at the leading (q_{s0}) and first order of approximation ($q_{s0} + \delta q_{s1}$) at the cross section 25 km from the upstream end of the river.

difference Mac Cormack scheme. Water depths and averaged flow velocities were computed at each grid cell as time progressed and used as inputs for the evaluation of the suspended sediment flux at the leading (q_{s0}) and first order of approximation ($q_{s0} + \delta q_{s1}$).

Figures 1.8 and 1.9 represent a comparison between the dimensionless suspended sediment transport capacity per unit width at the leading and first order approximations at a cross section 25 km far from the upstream end of the river during the passage of the flood. Note that, as expected, the peak of water discharge is delayed with respect the the peak of the 'equilibrium' suspended sediment flux. In fact, the latter is proportional to some power of the averaged flow velocity through the Shields stress and a flood wave is well known to experience the velocity peak first followed by the peak of water discharge.

The corrections of the suspended sediment flux due to the 'settling lag' effect and to the local variation of concentration have the coupled effect of increasing and delaying the peak of suspended sediment flux transported by the current. In fact, notice that in the cross section 25 km far from the up-

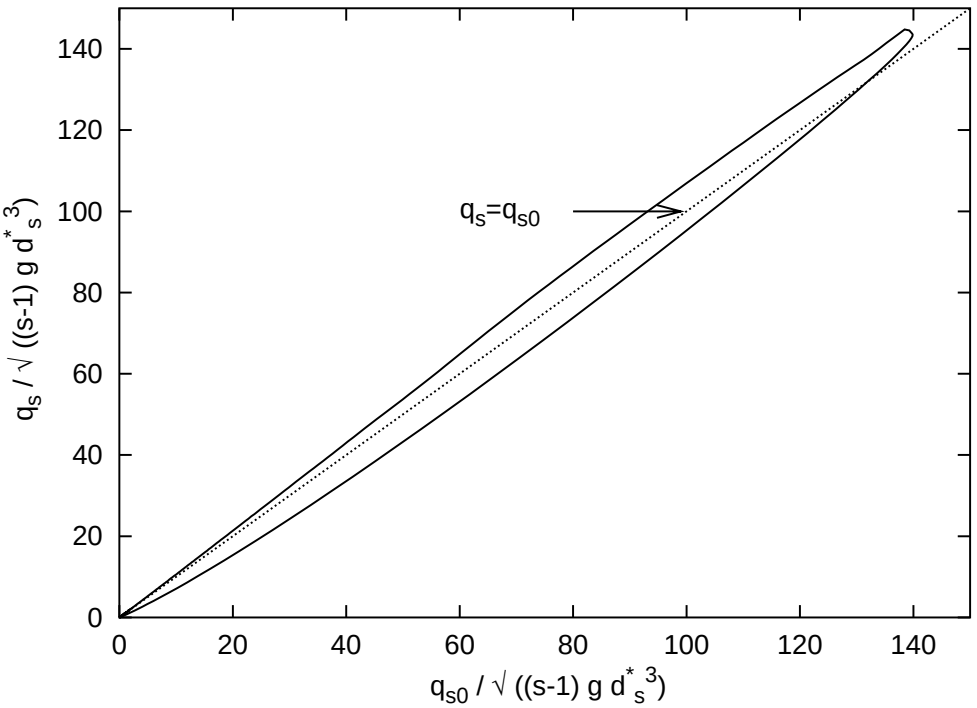

Figure 1.9: (q_{s0}) versus $(q_{s0} + \delta q_{s1})$ at the cross section 25 km far from the upstream end of the river during the passage of flood.

stream end of the river (Figure 1.8) the peak of the sediment flux is increased roughly by 3.5% and delayed 2.5 minutes. It is also worth noticing that the most significant contribution to the deviation from the equilibrium sediment flux is due to the temporal and spatial variations of concentration (Figure 1.10). Such effects are likely to play a crucial role in flows characterized by significant temporal and spatial variations of the hydrodynamics.

1.5 Conclusions

The achievements pursued in the present chapter are twofold:

- on one hand, we analyzed the conceptual and practical limits of Galappatti's perturbation approach;
- on the other hand, we developed an alternative depth averaged model for the transport of suspended sediment, based on a rational perturbation method, leading to a simple relationship for the flux of suspended sediment, suitable to applications to a variety of morphodynamic computations.

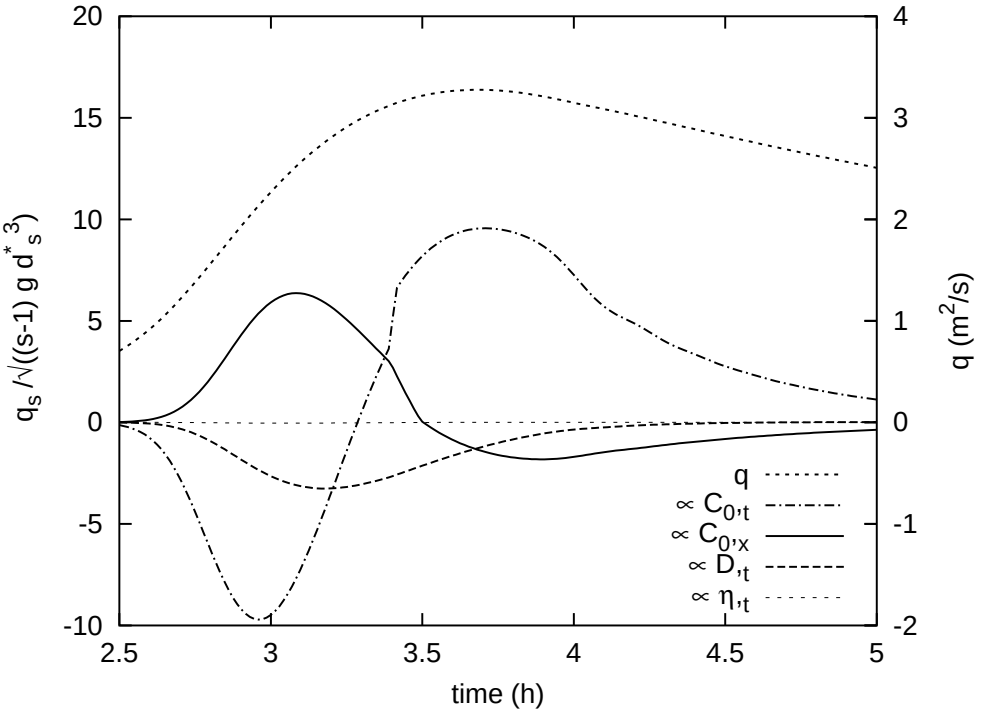

Figure 1.10: Contribution to the deviations from the equilibrium suspended sediment flux (see equation 2.23) at the cross section 25 km far from the upstream end of the river during the passage of flood.

The analysis reported in Sect. 1.2 has clarified that Galappatti's approach is non - standard, with the following consequences:

- its accuracy, in terms of the small parameters on which the perturbation approach is based, is not known a priori;
- the relative error of such solution with respect to the exact solution may be very large (locally exceeding 100% !) as suggested by the figures 1.3b and 1.4b.

The present approach has a major advantage: morphodynamic computations involving flows which are slowly varying in space and / or time can be performed using a depth averaged model for the hydrodynamics, coupled with a bed evolution equation (Exner's continuity equation) and the transport formula derived herein, whereby the suspended sediment flux is expressed in terms of local hydrodynamic quantities and their spatial - temporal derivatives. Such an approach, while retaining in a formally correct fashion all the relevant information arising from the 3D nature of the convection diffusion equation, avoids the need to solve the latter numerically at

each step, as required by most modern approaches. In the next chapter it will also be shown that the heavy numerical computations associated with morphodynamic calculations of long term equilibrium of tidal environments are considerably reduced if the present approach is employed.

Though the present analysis has been restricted to the 1D case, i.e. when spatial variations of the flow - topography fields occur only in the 'longitudinal' direction, the extension to the 2D case is straightforward. Through such an extension a variety of 2D configurations, like flows in tidal inlets, bifurcations, flows induced by large scale bedforms, become amenable to the present treatment.

Chapter 2

Long term morphodynamic equilibrium of tidal channels. Theoretical investigation.

We build on a recent contribution of *Lanzoni and Seminara* [2002] focused on the long term morphodynamic equilibrium of tidal channels. In the latter paper it was shown that, starting from an initially horizontal bed profile, a sediment wave develops in the channel carrying sediments landward and leading to deposition at the inner boundary until the bed emerged in the inner portion of the channel. The final equilibrium profile was found to be concave seaward and slightly convex landward. Furthermore, an equilibrium depth was reached at the inlet section which depended only on channel geometry and tidal forcing.

The latter work was based on various simplifying assumptions, namely sediment transport in equilibrium with the local and instantaneous hydrodynamic conditions at any cross section (including the inlet) and no overtides present in the tidal forcing. In the present contribution we remove the latter restrictions. We account for the effect of spatial and temporal variations of the channel hydrodynamics on the dynamics of suspended load with the help of a model of transport in suspension recently developed by the present author, suitable to flow fields which are slowly varying in space and time [*Bolla Pittaluga and Seminara*, 2002] and fully described in the previous chapter. Moreover, we take into account the ebb - flood asymmetry of sediment transport at the inlet through a simple model whereby the sediment flux during the ebb phase is assumed to be controlled by the transport capacity in the channel, while during the flood phase it is taken to be forced by some externally driven concentration. Finally, we investigate the effects of overtides contributing to the forcing tidal oscillation. Each of the latter effects turns

out to affect the long term morphodynamic evolution of tidal channels significantly but none of them prevents channels from reaching equilibrium.

In the next chapter, but see also *Tambroni et al.* [2003], the above findings are substantiated through the results of a laboratory investigation.

2.1 Introduction

The question of whether tidal channels may reach a state of morphodynamic equilibrium is of obvious practical relevance for the management of lagoon and estuarine environments. We note that, in the following, we define *morphodynamic equilibrium* a state such that the longitudinal bottom profile of the channel does not undergo net variations within a tidal cycle.

A number of ingredients may affect the establishment of such an equilibrium state.

The first ingredient is the nature of sediment transport, which is also related to the nature of the sediments present in the channel bed. Below, we consider the case of cohesionless sediments, which describes satisfactorily the characteristics of the tidal channels of Venice Lagoon [*Cola and Simonini*, 2002], the type of environment we ultimately wish to analyze. Moreover, we assume the size of sediments to be small enough for transport to occur both as bed load and as suspended load.

The second important ingredient controlling the establishment of equilibrium is the geometry of the channels. Tidal channels are typically landward convergent and meandering. We will indeed account for the effect of channel convergence while we will ignore the effects of variable curvature. The latter feature is quite important to determine the lateral equilibrium configuration of the bed [*Solari et al.*, 2002] but is likely to play a less important role in the establishment of the longitudinal equilibrium of the laterally averaged bed profile.

The third ingredient to be included is the forcing effect of the sea at the channel inlet. In fact, the sea is characterized by a given tidal oscillation of the free surface, the amplitude and harmonic content of which determines the hydrodynamic boundary condition for the tidal wave propagating along the channel. Moreover, the ability of the sea to exchange sediments with the channel through the inlet is essentially determined by the geometry of the inlet itself as well as by the sediment concentration at 'infinity' (i.e. far from the inlet section) which is in turn affected by the presence of littoral currents. The hydrodynamics of Venice inlets was investigated in detail by *Blondeaux et al.* [1982] assuming the bed to be fixed and plane. No attempt has been made to the authors' knowledge to extend the latter treatment to the case of

erodible beds. Below, we will employ a simple scheme to get some estimate of the effect of sediment exchange through the inlet, leaving to a future more detailed work an analysis of such effect based on a mobile bed extension of the work of *Blondeaux et al.* [1982].

A further ingredient plays an important role, namely the presence of tidal flats adjacent to the channel: we will leave aside the analysis of such effect. In fact, though the hydrodynamic effect of tidal flats on tide propagation in tidal channels may be simply accounted for in a 1D context following the treatment of e.g. *Speer and Aubrey* [1985], *Jay* [1991] and *Shetye and Gouveya* [1992], however the exchange of sediments between the channel and the adjacent flats is crucially dependent on the nature of flow in tidal flats. Tidal currents may indeed be too weak to be able to carry sediments in suspension, but resuspension may be typically driven by the action of wind waves. An analysis of such delicate mechanism cannot be investigated within the framework of a 1D model.

Finally, we will also ignore the possible effects that repetitive bar forms of the kind investigated by *Seminara and Tubino* [2001], possibly present on the channel bed, might induce on the establishment of an equilibrium bed profile.

The present work extends a recent analysis of *Lanzoni and Seminara* [2002] on the same topic. There, it was shown that, starting from an initially horizontal bed profile, a sediment wave develops in the channel carrying sediments landward and leading to deposition at the inner boundary until the bed emerges in the inner portion of the channel. A final equilibrium profile is established which is concave seaward and slightly convex landward. Furthermore, an equilibrium depth is reached in the inlet section which depends only on channel geometry and tidal forcing. However, the latter work was based on the following simplifying assumptions:

- sediment transport was assumed to be in equilibrium with the local and instantaneous hydrodynamic conditions;
- such assumption was applied at any cross section of the channel, including the inlet, thus preventing the possibility to account for the effect of a sediment exchange through the inlet, forced by concentration boundary conditions imposed by the sea state;
- the harmonic content of the tidal oscillation was assumed to consist of a single harmonic (M_2).

In the present contribution we wish to remove the latter restrictions. In fact, we will account for the effect of spatial and temporal variations of the

hydrodynamics on the dynamics of suspended load. This will be achieved with the help of a model of transport in suspension recently developed by the present author [*Bolla Pittaluga and Seminara*, 2002] and fully described in the previous chapter: such tool, suitable to flow fields which are slowly varying in space and time, provides a direct procedure to evaluate the suspended load for given hydrodynamic conditions. This is essential to the present calculations as solving the classical advection - diffusion equation for concentration to evaluate transport in suspension throughout each tidal cycle would make computations of long term equilibrium prohibitively heavy. We will also take into account the ebb - flood asymmetry of sediment transport at the inlet: this will be achieved through a simple model whereby the sediment flux during the ebb phase will be assumed to be controlled by the transport capacity of the flow in the channel, while, during the flood phase, the sediment flux will be taken to be forced by some externally driven concentration. Determining the latter accurately would require to solve for the flow field in the inlet region as pointed out above. In the present contribution we will simply stipulate that the externally driven concentration takes some given value and explore the consequences of such asymmetric condition, an exercise which proves instructive.

Finally, we will investigate the effects of overtides contributing to the forcing tidal oscillation, accounting for both the effects of their amplitude and of their phase relative to the dominant harmonic. Each of the latter effects turns out to affect significantly the long term morphodynamic evolution of tidal channels; however, it will appear that none of them prevents channels from reaching equilibrium.

Note that the subject of long term 1D equilibrium of tidal channels has also been investigated by the Utrecht group led by H. de Swart [*Schuttelaars and de Swart*, 1996, 2000]. For a discussion of the approach employed by the latter authors, the reader is referred to *Lanzoni and Seminara* [2002].

In the next chapter [but see also *Tambroni, Bolla Pittaluga and Seminara*, 2003] our theoretical findings are substantiated through the results of a laboratory investigation. It appears that observations do support the evolutionary picture arising from the computations. Moreover, they show that bedforms of different scales form in the channel, a non surprising feature based on the recent theoretical investigations of *Seminara and Tubino* [2001]. Finally, some interesting observations on the morphodynamic of the inlet region arise: in particular it turns out that the unsteady jet forming in the inlet region during the ebb phase leads to the excavation of a submerged channel, which in turn somewhat modifies the inlet hydrodynamics and morphodynamics. The latter observation confirms that, in order to evaluate the sediment exchange through the inlet with sufficient accuracy, an extension

of the work of *Blondeaux et al.* [1982] such to account for the mobile nature of the bed will eventually be needed.

2.2 Mathematical Formulation of the Hydrodynamic Problem

The hydrodynamics of tide propagation in convergent channels has been widely investigated. We follow, in particular, the mathematical formulation of *Lanzoni and Seminara* [1998, 2002] which will be briefly summarized below.

We refer to a straight tidal channel of length L_C^* (hereafter a star apex will denote dimensional quantities) closed at the landward end. The channel cross section will be effectively treated as rectangular, with channel width B^* varying landward according to the classical exponential law:

$$B^* = B_0^* \exp\left(-\frac{x^*}{L_b^*}\right), \tag{2.1}$$

where L_b^* is the so called *convergence length*, B_0^* is the channel width at the inlet and x^* is the longitudinal coordinate of the channel axis with origin at the channel inlet and pointing landward.

In the context of a 1D model the motion of the fluid phase is governed by the classical continuity and de Saint Venant equations, which express the principles of mass and momentum conservation. A dimensionless form of the latter equations was formulated by *Lanzoni and Seminara* [1998]. Below t^* denotes time, D^* is the flow depth averaged over the cross section, H^* is the water surface elevation, U^* is the longitudinal flow speed averaged over the cross section, g is gravity and C is the dimensionless Chezy coefficient, i.e. the flow conductance. The relevant flow variables are scaled as follows:

$$t^* = \omega^{*-1} t; \qquad (D^*, H^*) = D_0^*(D, H); \qquad U^* = U_0^* U;$$

$$C = C_0 c; \qquad x^* = L_0^* x, \tag{2.2a-e}$$

In (2.2) ω^{*-1} denotes the angular frequency of the tidal wave, U_0^* and C_0 are typical values of the longitudinal averaged speed and flow conductance respectively while L_0^* is the longitudinal spatial scale, whose value depends on the dynamic balance prevailing in the momentum equation for the particular tidal flow considered. With the latter notations the governing equations read:

$$\frac{1}{\epsilon} D_{,t} + \mathcal{F}\,(UD)_{,x} - \mathcal{K} U D = 0, \tag{2.3}$$

$$\mathcal{S}U_{,t} + \epsilon\mathcal{S}\mathcal{F}UU_{,x} + \frac{1}{\epsilon}H_{,x} + \mathcal{R}\frac{U|U|}{c^2 D} = 0. \tag{2.4}$$

In (2.3, 2.4) various dimensionless parameters appear which read:

$$\epsilon = \frac{a_0^*}{D_0^*}; \qquad \mathcal{F} = \frac{1}{\epsilon}\frac{U_0^*}{\omega^* L_0^*}; \qquad \mathcal{K} = \frac{1}{\epsilon}\frac{U_0^*}{\omega^* L_b^*}; \tag{2.5}$$

$$\mathcal{S} = \frac{F_0^2}{\epsilon}\frac{\omega^* L_0^*}{U_0^*}; \qquad \mathcal{R} = \frac{F_0^2}{\epsilon}\frac{L_0^*}{C_0^2 D_0^*}. \tag{2.6}$$

Here a_0^* represent the amplitude of the tidal wave at the mouth and F_0 denotes a typical value of the Froude number.

We recall that $\mathcal{S}$ and $\mathcal{R}$ weigh the importance of local inertia and friction relative to gravity respectively. Depending on the values attained by the ratio $\mathcal{R}/\mathcal{S}$ $(= U_0^*/\omega^* C_0^2 D_0^*)$, estuaries can be classified as strongly $(\mathcal{R}/\mathcal{S} \gg 1)$ or weakly dissipative $(\mathcal{R}/\mathcal{S} \ll 1)$: a wide variety of typologies are found in nature [*Lanzoni and Seminara*, 1998].

The latter equations must be supplemented by appropriate boundary conditions. At the channel mouth we set

$$H|_{x=0} = 1 + \alpha\left[\cos\ t + \beta\cos\ 2(t-\phi)\right]. \tag{2.7}$$

The latter assumption will allow us to investigate the role of an M_4 overtide of amplitude β and phase lag ϕ relative to a dominant M_2 component.

The landward boundary condition requires more care. In the initial phase of the morphodynamic evolution, when the bed keeps submerged throughout the whole channel, we set:

$$U|_{x=1} = 0 \tag{2.8}$$

As the deposition process close to the landward boundary leads to the formation of a shoal where the flow depth approaches a vanishing value, an appropriate treatment is needed for the dry and wet region where the shoreline oscillates backward and forward. Denoting the longitudinal coordinate of the shoreline by $x_{sh}(t)$, the exact boundary condition replacing (2.8) reads:

$$U|_{x_{sh}(t)} = \dot{x}_{sh}(t). \tag{2.9}$$

Implementing numerically the latter boundary condition is a somewhat difficult job (see for instance *Pritchard and Hogg* [2002]). Herein we have developed a method based on a lagrangian approach which is capable to follow the dry/wet front. An alternative approach, used by *Lanzoni and Seminara* [2002] is to assume the whole domain to be permanently covered with water, the dry region being modelled as a region where the fluid keeps confined

within the interstices of the roughness elements [e.g. *Defina*, 2000]. The latter approach is widely employed in numerical codes dealing with drying and wetting problems.

In the present contribution a front tracking technique is pursued, based on the introduction of a Riemann problem at the edge between the 'last wet grid' point N and the 'first dry grid' point $N+1$ [*Toro*, 2001]. Being the solution at time step n piecewise constant, the hyperbolic character of the governing equations gives rise to the generation of waves leaving from the discontinuity between two adjacent grid points, say j and $j+1$. It is well known that such waves, depending upon the solution at time step n, can be either 'rarefaction' or 'shock' waves: the former arise from an expansion of characteristics which determines the so called 'fan region', the latter is generated by the intersection of characteristics leaving from two adjacent cells.

In the present problem we introduce a Riemann problem for the last wet grid point, with initial conditions:

$$D(x,0) = \begin{cases} D_N & x \leq x_{sh}^n \\ 0 & x > x_{sh}^n \end{cases} \tag{2.10}$$

$$U(x,0) = \begin{cases} U_N & x \leq x_{sh}^n \\ 0 & x > x_{sh}^n \end{cases} \tag{2.11}$$

where the longitudinal coordinate of the dry/wet front is denoted by x_{sh}^n.

In this case, since no water is present on the right of the discontinuity, no wave can propagate through, hence the solution contains only a rarefaction associated with the backwards characteristics C_- and a contact discontinuity of speed $S_N^* = U_N + 2c_N$ that coincides with the tail of the rarefaction, with $c_N = \sqrt{gD_N}$. On the other hand, the head of the rarefaction propagates with speed $S_N = U_N - c_N$.

Three different possible cases arise time stepping the solution from n to $n+1$. Initially it is necessary to evaluate whether the first dry point becomes wetted at time step $n+1$. In order for the latter argument to apply, the tail of the rarefaction has to reach the grid point $N+1$ which, in this case, becomes the last wet grid point of the computational domain at time step $n+1$. In this case the solution within the 'fan region', and consequently in the wetted point', is easily determined via the Riemann invariants (figure 2.1).

Alternatively, the last wet point N keeps unchanged time stepping from n to $n+1$. In this case if the head of the 'fan region' propagating with speed $S_N = U_N - c_N$ reaches the grid point N at time step $n+1$ then the solution in the last wet point is determined via the Riemann invariants along a suitable C_- characteristic (figure 2.2). Otherwise two scenarios are possible

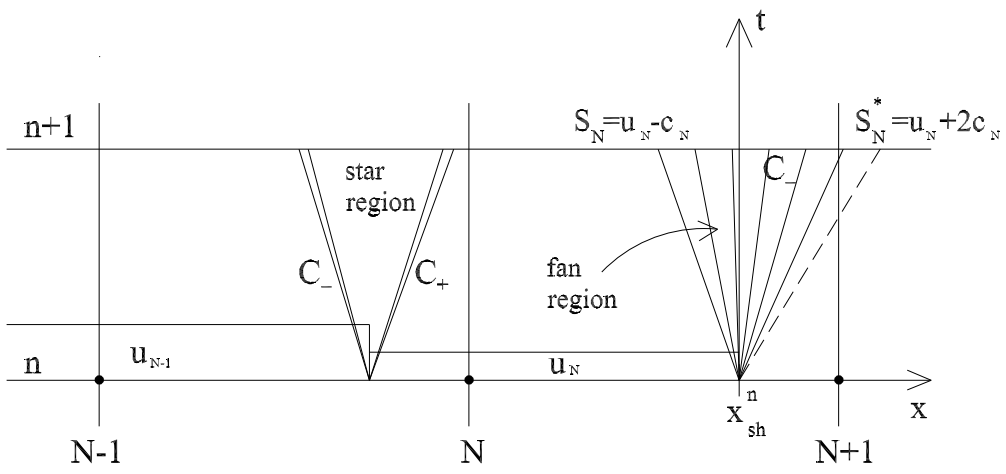

Figure 2.1: Riemann problem at the edge between the 'last wet grid' point N and the 'first dry grid' point $N+1$. The tail of the 'fan region' reaches the grid point $N+1$ at time $n+1$.

depending upon the propagation of the C_+ characteristic wave leaving from the discontinuity between grid points $N-1$ and N. If such a wave does not reach the grid point N at time step $n+1$ then the solution at that point keeps unchanged (figure 2.3), otherwise is is necessary to compute the solution in the so called 'star region' delimited by backward and forward characteristics (figure 2.4).

2.3 Mathematical Formulation of the Problem of Morphodynamics

In a channel with erodible bed, flow depth and free surface elevation are independent variables. Hence, the system (2.3, 2.4) is a system of two differential equations in the three unknowns U, H, D. In order to close the mathematical formulation we need to couple the hydrodynamics with the morphodynamics. Accounting for the effect of local variations of the averaged sediment concentration on the sediment balance (a contribution usually neglected), the evolution equation of the bed interface, i.e. the 1D equation of the mass conservation of sediments [*Exner*, 1925] reads:

$$(1-p)B^*\left(D^*\overline{C}_{,t^*}+\eta^*_{,t^*}\right)+\left(B^*q_s^*\right)_{,x^*}=0, \tag{2.12}$$

where η^* is the local and instantaneous value of the bed elevation averaged over the cross section, $\overline{C}$ is the sediment concentration averaged over the cross

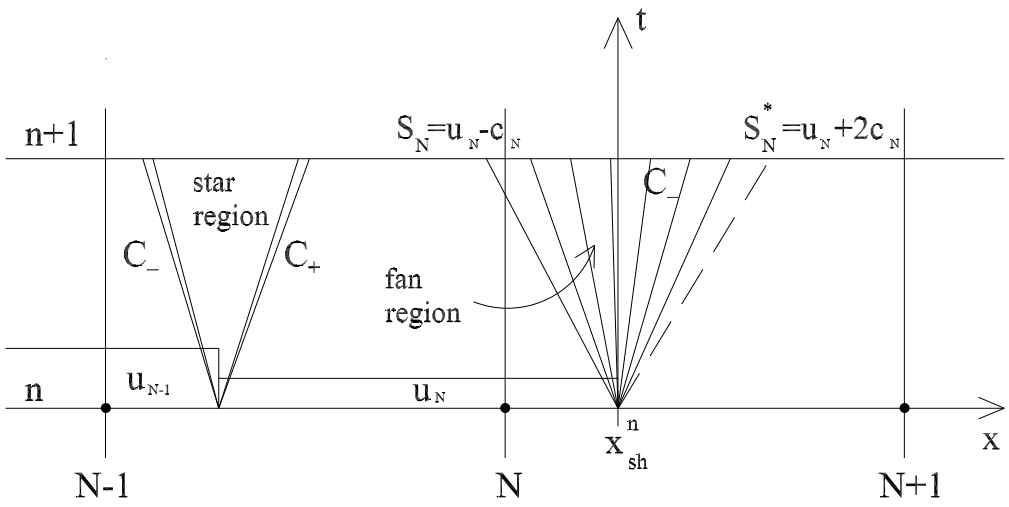

Figure 2.2: Riemann problem at the edge between the 'last wet grid' point N and the 'first dry grid' point $N+1$. The tail of the 'fan region' does not reach the grid point $N+1$ at time $n+1$. The last grid wet point N falls within the 'fan region' at time $n+1$.

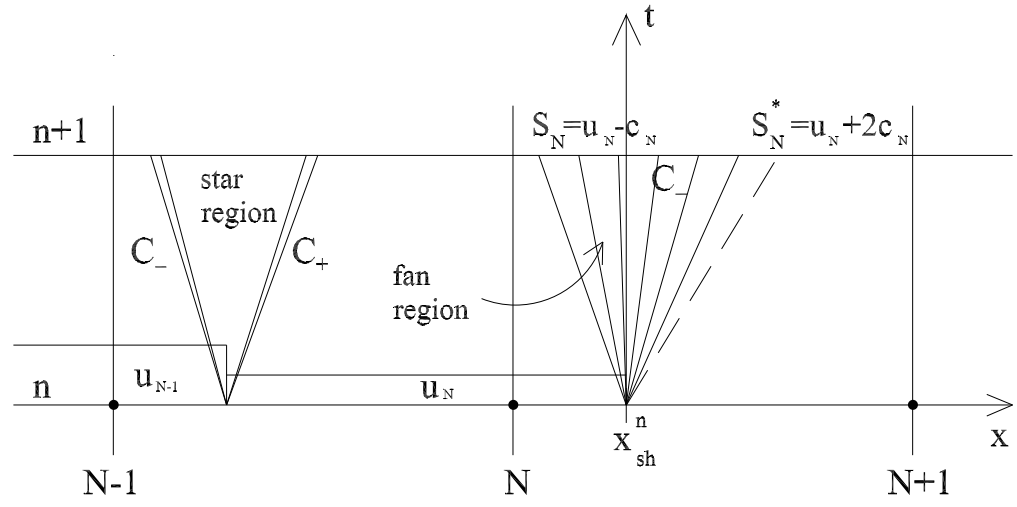

Figure 2.3: Riemann problem at the edge between the 'last wet grid' point N and the 'first dry grid' point $N+1$. The last grid wet point N does not fall within either the 'fan region' or the 'star region' at time $n+1$. The values of the variables at grid point N keep unchanged at time step $n+1$.

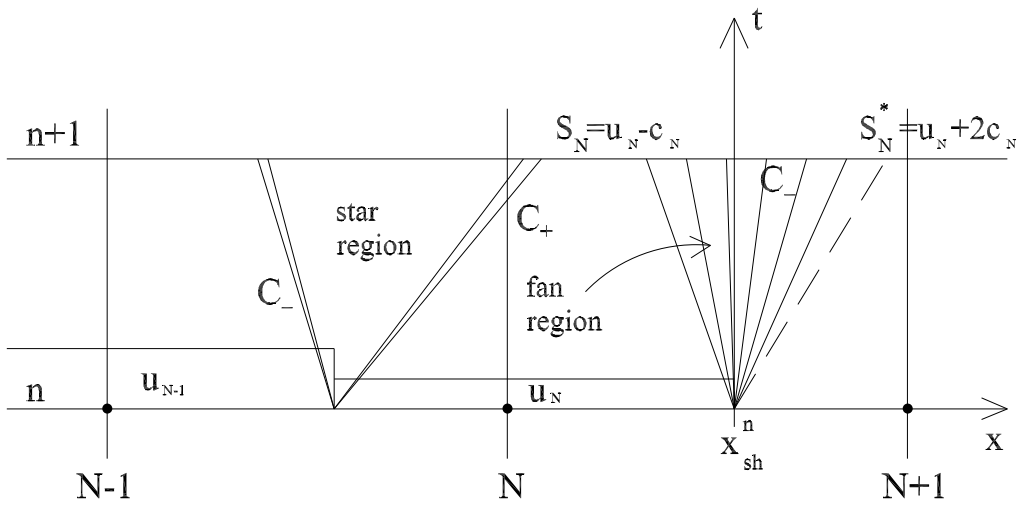

Figure 2.4: Riemann problem at the edge between the 'last wet grid' point N and the 'first dry grid' point $N+1$. The last grid wet point N does not fall within the 'fan region'. The C_+ wave leaving the discontinuity between the variables u_N and u_{N-1} reaches the grid point N.

section, p is sediment porosity and q_s^* is the sediment flux per unit width. Note that the latter equation accounts for the main mechanisms contributing to determining the sediment balance in a tidal channel, namely the transport of sediments as bed load and suspended load in a convergent channel. On the contrary, the exchange of sediments between the channel and the adjacent flats is not incorporated in equation (2.12). As discussed in the Introduction, describing such effect will require the development of a model of sediment deposition and resuspension in tidal flats due to the action of tidal currents and wind waves. It is convenient to make the relevant variables dimensionless as follows:

$$t^* = \mathcal{T}_0^* \tau; \qquad \eta^* = D_0^* \eta; \qquad q_s^* = \sqrt{\Delta g d_s^{*3}}\, q_s;$$
$$\mathcal{T}_0^* = \frac{(1-p)\, D_0^* L_0^*}{\sqrt{\Delta g d_s^{*3}}}; \qquad \Delta = \frac{\rho_s - \rho}{\rho}, \tag{2.13a-e}$$

with $\mathcal{T}_0^*$ morphological time scale, d_s^* grain size, ρ and ρ_s water and sediment densities respectively. The evolution equation of the bed interface (2.12) then becomes:

$$D\overline{C}_{,\tau} + \eta_{,\tau} + \left(q_{s,x} - \frac{\mathcal{K}}{\mathcal{F}}\, q_s \right) = 0 \tag{2.14}$$

Note that the latter form of the evolution equation differs from the corresponding form employed by *Lanzoni and Seminara* [2002, equation 14] for

the inclusion of the first term in the left hand side. As mentioned above such term is usually neglected in the morphodynamic literature without justification. We show below that its effect is negligible in the present context.

The next ingredient needed to make any progress with the latter formulation is some description of the dynamics of sediments transported as bed load and as suspended load which allows one to evaluate the total load q_s. *Lanzoni and Seminara* [2002] employed the simplest approach, based on the assumption that sediment transport keeps in equilibrium with the local and instantaneous hydrodynamic conditions. Such assumption allowed the latter authors to make use of fairly established semi-empirical relationships available from the fluvial literature. These relationships were extended to tidal channels simply relating the total load to the instantaneous value of the Shields stress ϑ and to the particle Reynolds number R_p respectively defined as follows:

$$\vartheta = \frac{\tau_0^*}{(\rho_s - \rho) g d_s^*}; \qquad R_p = \frac{\sqrt{\Delta g d_s^{*3}}}{\nu}, \tag{2.15}$$

τ_0^* being the local and instantaneous value of the laterally averaged bottom stress. We have shown in the previous chapter that, as regards suspended load, such approach may be rationally substantiated as being equivalent to truncating at the leading order of approximation an expansion of the averaged sediment concentration in terms of the small parameter δ defined in the form:

$$\delta = \frac{D_0^*}{L_0^*} \frac{U_0^*}{W_s}, \tag{2.16}$$

having denoted by W_s the settling speed of sediment particles. Physically, the latter approach essentially assumes that, locally and instantaneously, the vertical flux associated with particle settling balances that driven by vertical turbulent diffusion. Longitudinal advection, as well as local variations of concentration and longitudinal diffusion are then neglected.

In the present contribution, the total sediment flux per unit width q_s^* instantaneously transported by the tidal current at a given location is calculated as the sum of a bedload component q_{sb}^* and a suspended load component q_{ss}^*.

Various relationships have been proposed in the literature to quantify the bedload transport rate per unit width associated with steady unidirectional streams [e.g. *Meyer-Peter and Müller*, 1948; *van Rijn*, 1984a]. In tidal environments flow unsteadiness may in principle lead to non equilibrium effects. Though this is a fairly unexplored subject, it seems unlikely that non equilibrium effects may be significant in tidal contexts as long as bedload

transport is concerned. In fact, the time scale of particle saltation, i.e. of the process of bedload transport, is of the order of seconds, hence many orders of magnitude smaller than the tidal period. We then neglect non equilibrium effects and estimate the bedload flux per unit width employing the equilibrium formula of *Meyer-Peter Müller* [1948] which reads:

$$q^*_{sb} = 8(\vartheta - \vartheta_c)^{3/2}\sqrt{\Delta g d^{*3}_s} \tag{2.17}$$

As far as suspended load is concerned, in order to determine the flow conditions for initiation of suspension we follow *van Rijn*'s [1984b] criterion, which reads

$$\frac{u_*}{W_s} = N \tag{2.18}$$

where

$$\begin{cases} N = 4R_p^{-2/3} & (1 \leq R_p^{2/3} \leq 10) \\ N = 0.4 & (R_p^{2/3} > 10) \end{cases} \tag{2.19}$$

The suspended flux per unit width q^*_{ss} is evaluated using the formulation of the transport of suspended sediment by slowly varying flows reported in the previous chapter.

Hence, we write:

$$\boxed{q^*_{ss} = q^*(x,t)\,\psi(x,t)}\,, \tag{2.20}$$

where q^* is the local flow discharge per unit width and the function ψ has the form

$$\psi(x,t) = \psi_0 + \delta\psi_1 + O(\delta^2), \tag{2.21}$$

$$\psi_0 = \frac{\sqrt{C_{f0}}}{k} C_e \left[I_{02} + K_1 I_{01}\right]\ , \tag{2.22}$$

$$\psi_1 = \frac{\sqrt{C_{f0}}}{k}\left[D\frac{\partial \overline{C}_0}{\partial t}\ q_{s11} + \overline{U}D\frac{\partial \overline{C}_0}{\partial x}\ q_{s12} + \frac{\partial \eta}{\partial t}\overline{C}_0\ q_{s13} + \frac{\partial D}{\partial t}\overline{C}_0\ q_{s14}\right], \tag{2.23}$$

Here $I_{0j}(j = 1, 2)$ and $q_{s1j}(j = 0, 3)$ are integrals whose analytical expressions are reported in (1.86, 1.87) and C_e is the reference concentration evaluated at the conventional elevation a^*. All the above coefficients are functions of the parameters $\zeta_R (= a^*/D^*)$ and Z. In order for the relationships (2.20, 2.21, 2.22, 2.23) to provide a simple tool to be incorporated into numerical models of morphodynamic evolution, appropriate analytical forms for such coefficients are needed. They were derived by the author by suitably interpolating the exact values. A simple analytical approach is thus available to

evaluate the flux of suspended sediment in slowly varying flows with applications to a variety of morphodynamic contexts including tidal and fluvial environments. Needless to say, such approach still has to rely on empirical expressions to evaluate the reference quantities C_e and a^*. They typically correlate C_e with the Shields stress ϑ and the particle Reynolds number R_p. In the present contribution we follow *van Rijn* [1984b] and write:

$$C_e = 0.015 \frac{d_{50}^*}{a^*} \frac{T^{1.5}}{R_p^{0.2}} \tag{2.24}$$

$$a^* = \begin{cases} e_r^* & (e_r^* \geq 0.01 D^*) \\ 0.01 D^* & (e_r^* < 0.01 D^*) \end{cases} \tag{2.25}$$

where d_{50}^* is the average grain size, $T = (\vartheta' - \vartheta_c)/\vartheta_c$ is a transport stage parameter and θ' is the frictional component of the Shields stress. The total roughness height e_r^* depends on the presence of small scale bedforms on the bed and can be estimated by means of the following relationship:

$$\begin{array}{cc} \epsilon_r^* = 3 d_{90}^* & (T \geq 25) \\ \epsilon_r^* = 3 d_{90}^* + 1.1 A^* [1 - \exp(-25 A^*/L^*)] & (0 < T < 25) \end{array} \tag{2.26}$$

where d_{90}^* is the grain size such that 90% of the sediment is finer and A^* and L^* are dune amplitude and wavelength, respectively given in the form:

$$\begin{array}{c} L^* = 7.3 D^* \\ A^* = 0.11 \; D^* \left(d_{50}^*/D^*\right)^{0.3} [1 - \exp(-T/2)](25 - T) \end{array} \tag{2.27}$$

Note that within a neighborhood of the instant of flow reversal no bedload transport occurs as θ does not exceed θ_c. Similarly, when θ falls below the threshold value θ_{cs} for particle entrainment in suspension only sediment deposition occurs. Such effects have not been accounted for as this would require a detailed evaluation of the temporal evolution of the concentration profile close to flow reversal.

The relationships (2.17) and (2.20-2.27) allow one to evaluate the total sediment flux to be fed in the bottom evolution equation (2.14).

In order to complete the formulation of the morphodynamic problem an appropriate boundary condition must be associated with equation (2.14). As mentioned in the Introduction, in order to account for the ebb - flood asymmetry of sediment transport at the inlet we employ a simple model: the sediment flux during the ebb phase is assumed to be controlled by the transport capacity of the flow in the channel, while, during the flood phase, the sediment flux is taken to be forced by some 'sea' concentration which is given some prescribed value. Exploring the consequences of such asymmetric

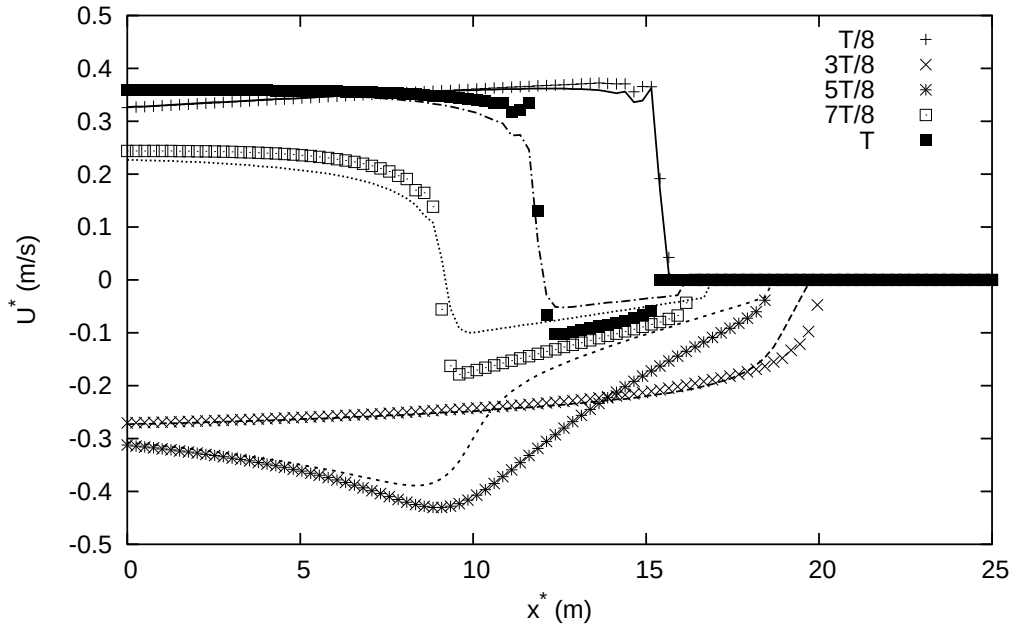

Figure 2.5: Snapshots of the free surface elevation at different times calculated using the 'front-tracking' method (points) and the LS (2002) model (lines).

condition is an exercise which will prove instructive and will provide some qualitative understanding of the process as a good premise to more accurate predictions that will require detailed solutions of the flow field in the inlet region.

2.4 Numerical tests

In order to test the 'front-tracking' method introduced in the previous section a comparison with a different numerical approach has been performed. In particular we tested the model proposed with the one used in *Lanzoni and Seminara* [2002] (hereafter referred to as LS (2002)) which was obtained reformulating the differential equations governing the flow and the sediment balance over partially wet elements by introducing a sub-grid model based on the statistics of bottom topography [*Defina et. al*, 1994; *Defina*, 2000].

Initially a validation of the fixed bed model has been performed in order to illustrate that wave run-up on a sloping beach was properly reproduced by the two models. The typical parabolic like water profile was observed during the wave run-up as reported in Figure 2.5 showing snapshots of the free

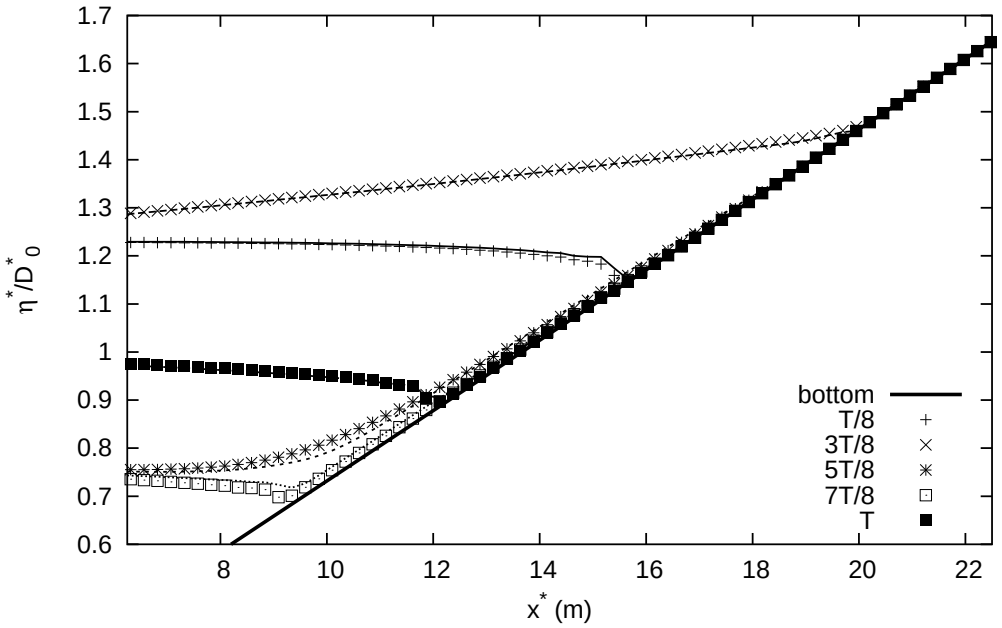

Figure 2.6: Snapshots of the velocity along the beach at different times calculated with the 'front-tracking' method (points) and with the LS (2002) model (lines).

surface elevation at different times calculated using the two models. Note that the agreement between the two approaches seems to be satisfactory. Velocities calculated during the wave run-up appear to be quite close in the two models while some difference can be detected during the wave run-down (Figure 2.6) close to the wave front.

A comparison between the two models has also been performed evaluating the difference between the morphodynamic evolution of a tidal channel closed at one end and connected to a tidal sea at the other end. It is well known that, starting from a flat bed, the system evolves toward an equilibrium configuration characterized by vanishing net sediment flux over a tidal cycle. Figure 2.7 reports a comparison between the equilibrium longitudinal profiles calculated employing the two methods and shows that the agreement is poor only within a limited portion of the channel.

Differences are emphasized considering the evolution of a sloping beach subjected to the action of wave motion. Starting from a bottom profile characterized by an upper portion which is not wetted even at high water, the system evolves toward an equilibrium configuration which is degraded in the case of the model of LS (2002) compared to the other (Figure 2.8). In fact the former models the entire computational domain to be permanently

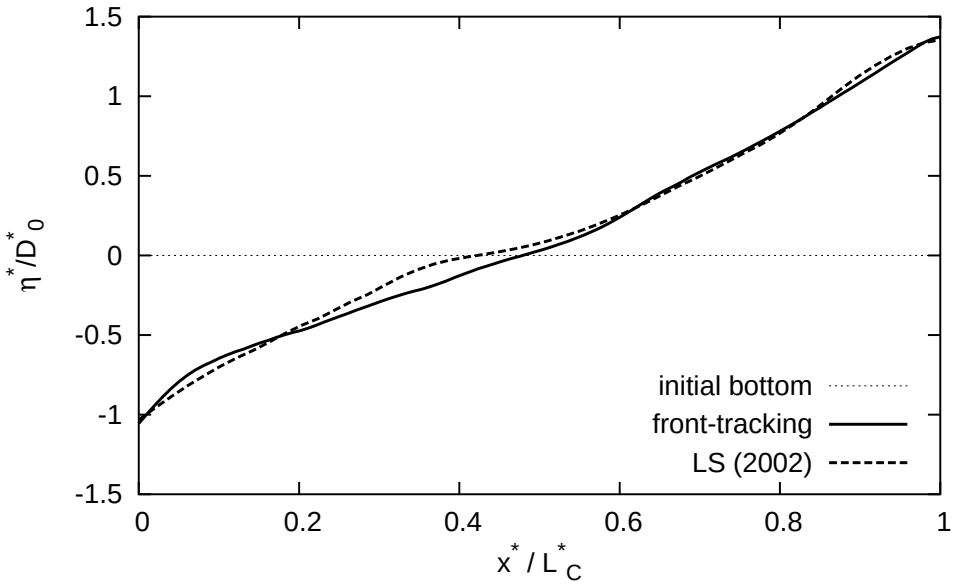

Figure 2.7: Comparison between the equilibrium configuration of a tidal channel calculated with the 'front-tracking' method and with the LS (2002) model. The initial bottom configuration is flat.

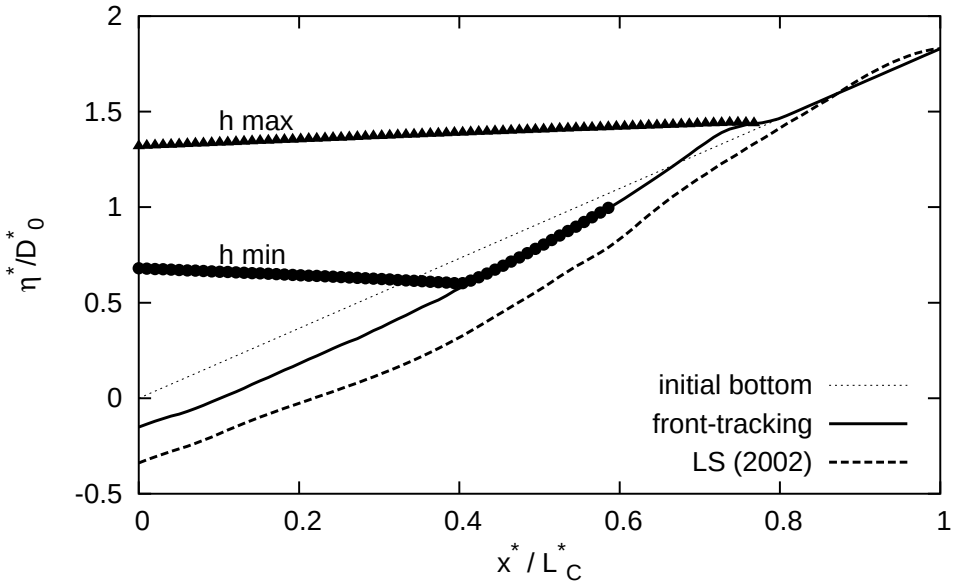

Figure 2.8: Comparison between the equilibrium configuration of a tidal channel calculated with the 'front-tracking' method and with the LS (2002) model. Initial bottom configuration was a sloping beach with the upper part emerged even at high water.

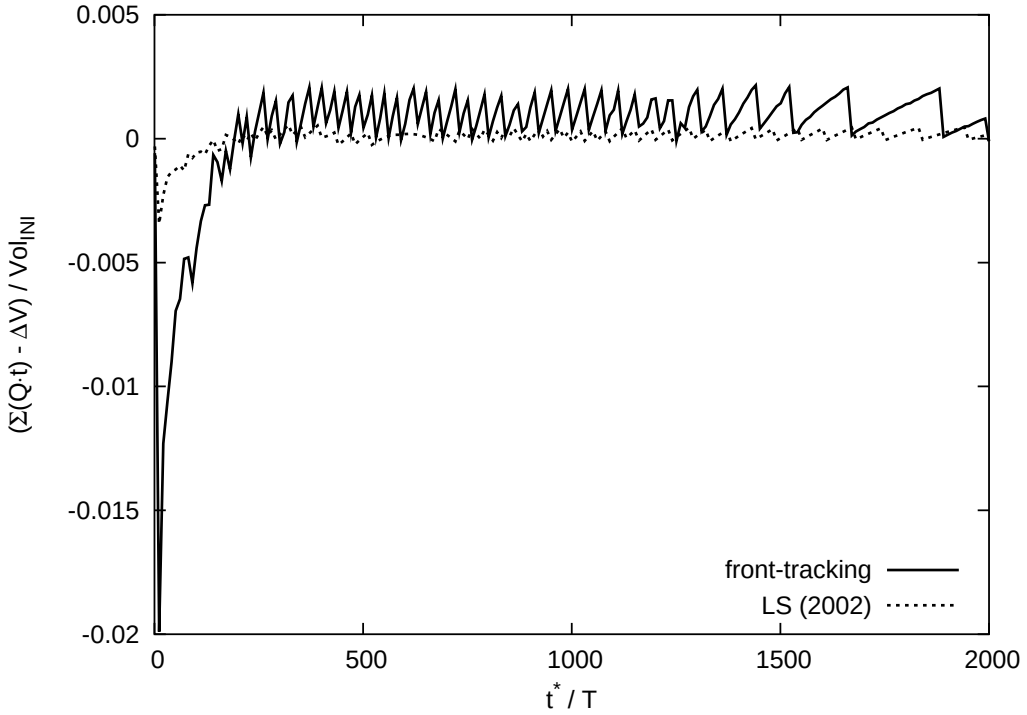

Figure 2.9: Difference between the volume of water exchanged at the inlet cross section every tidal cycle and the variation in a tidal cycle of the water volume stored in the channel. Volumes are scaled by the volume of water initially stored in the channel.

covered by water independently by the fact that the actual water level would be lower than the bottom elevation. As a consequence in this case the upper portion of the channel undergoes an evolution which is not physically based since water never gets that portion wet.

It is known from the literature that numerical models can be affected by problems related to mass conservation. In fact, though the equation solved in the numerical models are based on conservation principles, they can give rise to unphysical losses of water and sediment. Figure 2.9 shows the difference between the volume of water exchanged at the inlet cross section every tidal cycle (the channel is closed at the landward end) and the variation in a tidal cycle of the water volume stored in the channel. It appears that the LS' (2002) approach is slightly more accurate in terms of water conservation: in fact, the front-tracking approach displays a loss rangign about 0.1% which is exceeded only at the beginning of the experiment when the loss reaches a value ranging about 2%.

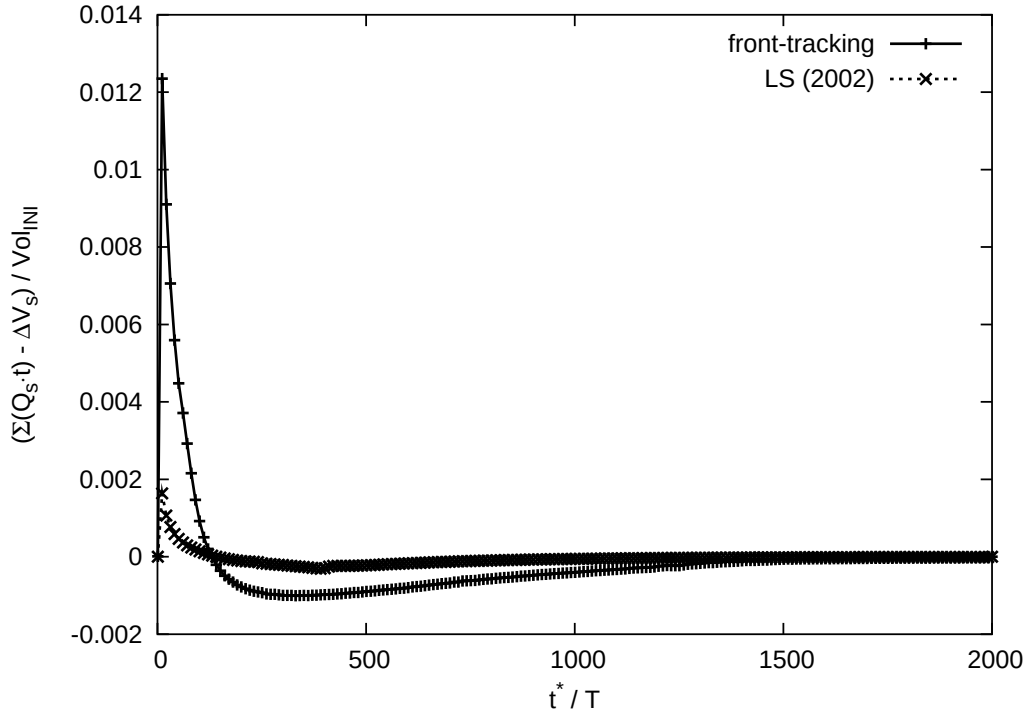

Figure 2.10: Difference between the volume of sediment exchanged at the inlet cross section every tidal cycle and the variation in a tidal cycle of the sediment volume stored in the channel. Volumes are scaled by the volume of water initially stored in the channel.

The same features are revealed by Figure 2.10 which shows a comparison between the volume of sediment exchanged at the inlet cross section every tidal cycle and the variation in a tidal cycle of the sediment volume stored in the channel.

2.5 Results: effects of overtides

Since many features of the response of estuarine channels to tidal forcing are revealed by the first harmonic [*Speer and Aubrey*, 1985; *Parker*, 1991], *Lanzoni and Seminara* [2002] focused their attention on a tidal forcing at the channel inlet which was assumed to consist of a single semidiurnal M_2 tide. However it is well known that the the effect of overtides may alter the character of tide propagation in the channel, which may turn from flood- into ebb- dominant. Typically overtides are present at the inlet of the channel when the offshore shelf is wide and flat [*van Dongeren and de Vriend*, 1994].

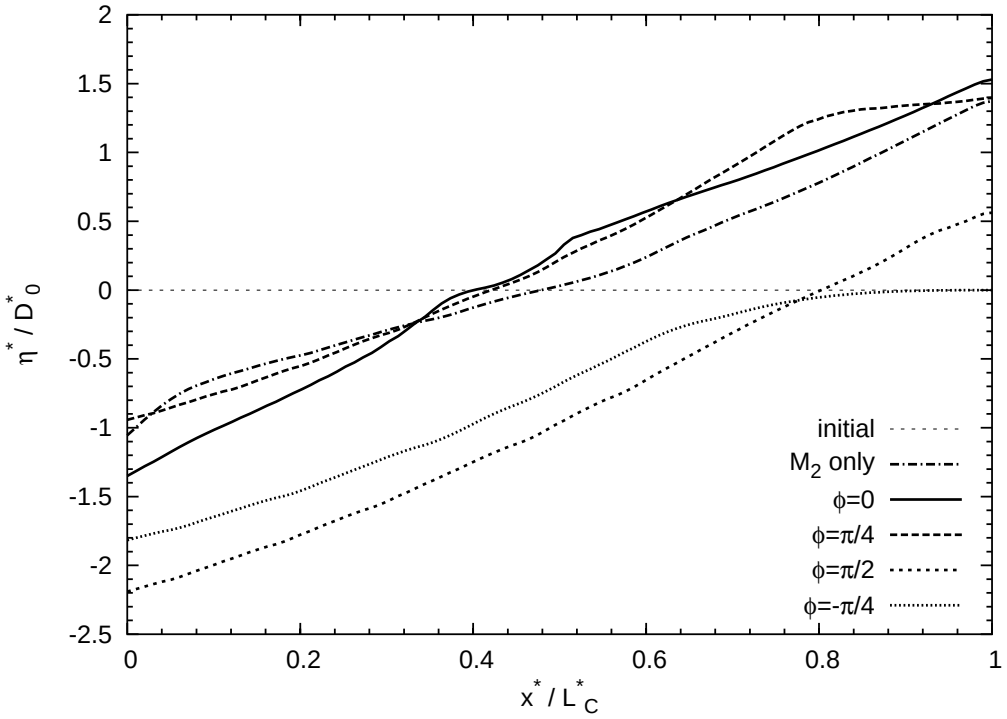

Figure 2.11: Equilibrium configurations of a tidal channel for different values of the phase lag ϕ between the M_2 and the M_4 components of the tidal oscillation at the sea. The ratio between the amplitudes of the M_2 and the M_4 components is 0.2.

In the present context we investigated the case of tidal oscillations in the sea containing an additional contribution from an overtide M_4 besides the dominant harmonic M_2, since higher armonics usually play a negligible role in the morphological evolution of tidal channels. The form of the imposed oscillation is in equation 2.7. We investigated how such additional contribution affects the morphodynamic evolution of a tidal channel.

Indeed, the equilibrium configuration of the channel turns out to be significantly affected by such contributions: this is shown in Figure 2.11 for different values of the phase lag between the M_2 and M_4 components and for a given ratio between the two amplitudes ($\alpha = 0.2$). In particular, the equilibrium profiles for the cases $\phi = \pi/2$ and $\phi = -\pi/4$ appear to have led to strong degradation of the channel compared with the others. An explanation of such findings can be easily given in terms of flood- or ebb- dominance. In fact, a glance at Figure 2.12, which reports the maximum and minimum velocities calculated at the inlet cross section shows that the above extreme

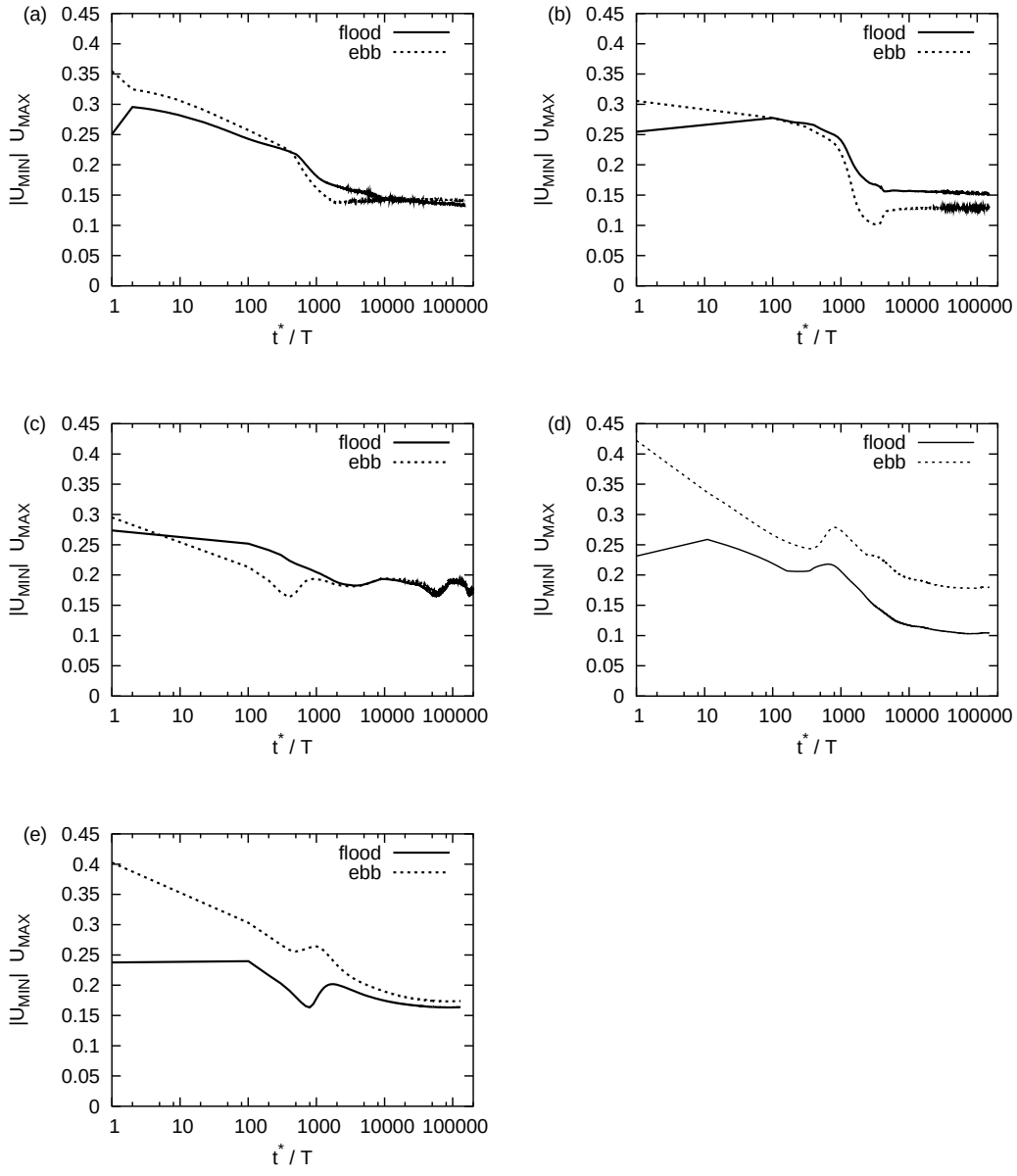

Figure 2.12: Comparisons between the maximum velocity during the flood and ebb phases at the inlet of a tidal channel for different values of the phase lag ϕ between the M_2 and the M_4 components of the tidal oscillation at the sea. The ratio between the amplitudes of the M_2 and the M_4 components is 0.2. (a) M_2 only, (b) $\phi = 0$, (c) $\phi = \pi/4$, (d) $\phi = \pi/2$, (e) $\phi = -\pi/4$.

degradation is associated with a marked ebb-dominance at the inlet which persists during the evolution of the channel. Ebb-dominance in the seaward portion of the channel and flood-dominance in the landward portion of the channel are features often recurring in flat channels as shown in Figure 2.13 reporting the velocities calculated along the channel at the initial stage of the experiment when the bed was still horizontal. Once equilibrium is reached such distinction is typically less marked and the degree of ebb/flood dominance as well as velocity diminish (Figure 2.14).

Figure 2.15 represents a comparisons between the maximum Shields stress over a tidal cycle at the equilibrium configuration for different values of the phase lag ϕ between the M_2 and the M_4 components of the sea oscillation. The ratio between the amplitudes of the M_2 and the M_4 components is again $\alpha = 0.2$. Notice that, at equilibrium, sediment transport is still present and sediments can even be transported in suspension in the case of $\phi = -\pi/4$. The present plot reports results which have been obtained using a domain discretization involving 100 nodal points. Further mesh refining would be required in order to smooth out the discontinuities in the longitudinal derivative of the maximum Shields stress which appear in the latter plot, but this would make the computation extremely heavy. The above results confirm the conclusion of *Lanzoni and Seminara* [2002] who definied morphodynamic equilibrium as a dynamic state such that the longitudinal bottom profile of the channel does no longer undergo net variations within a tidal cycle, a condition which does not necessarily imply vanishing sediment discharge at every instant of the tidal cycle nor it prevents the development and migration of tidal bedforms.

The present model cannot describe the hydrodynamics of the flow field in the region close to the inlet, which is known [*Blondeaux et al.*, 1982] to have a nearly irrotational 2D character during the flood phase and the structure of an unsteady turbulent jet during the ebb phase. This notwithstanding, an attempt to account in a simple form for the effects of such hydrodynamic asymmetry on the exchange of sediments between the channel and the sea has been made through a simple scheme whereby the sediment flux leaving the channel during the ebb phase has been assumed to be controlled by the transport capacity of the stream at the inlet section of the channel, while the sediment flux entering the channel during the flood phase has been assumed to be driven by some fixed sea sediment concentration. Most of the results presented below have been obtained assuming that the sea sediment concentration is in equilibrium with the local hydrodynamic conditions. Neglecting the possible presence of overtides in the tidal forcing and assuming an 'equilibrium' sediment concentration in the sea, as discussed above, the model suggests that the inlet reaches equilibrium when the bottom shear

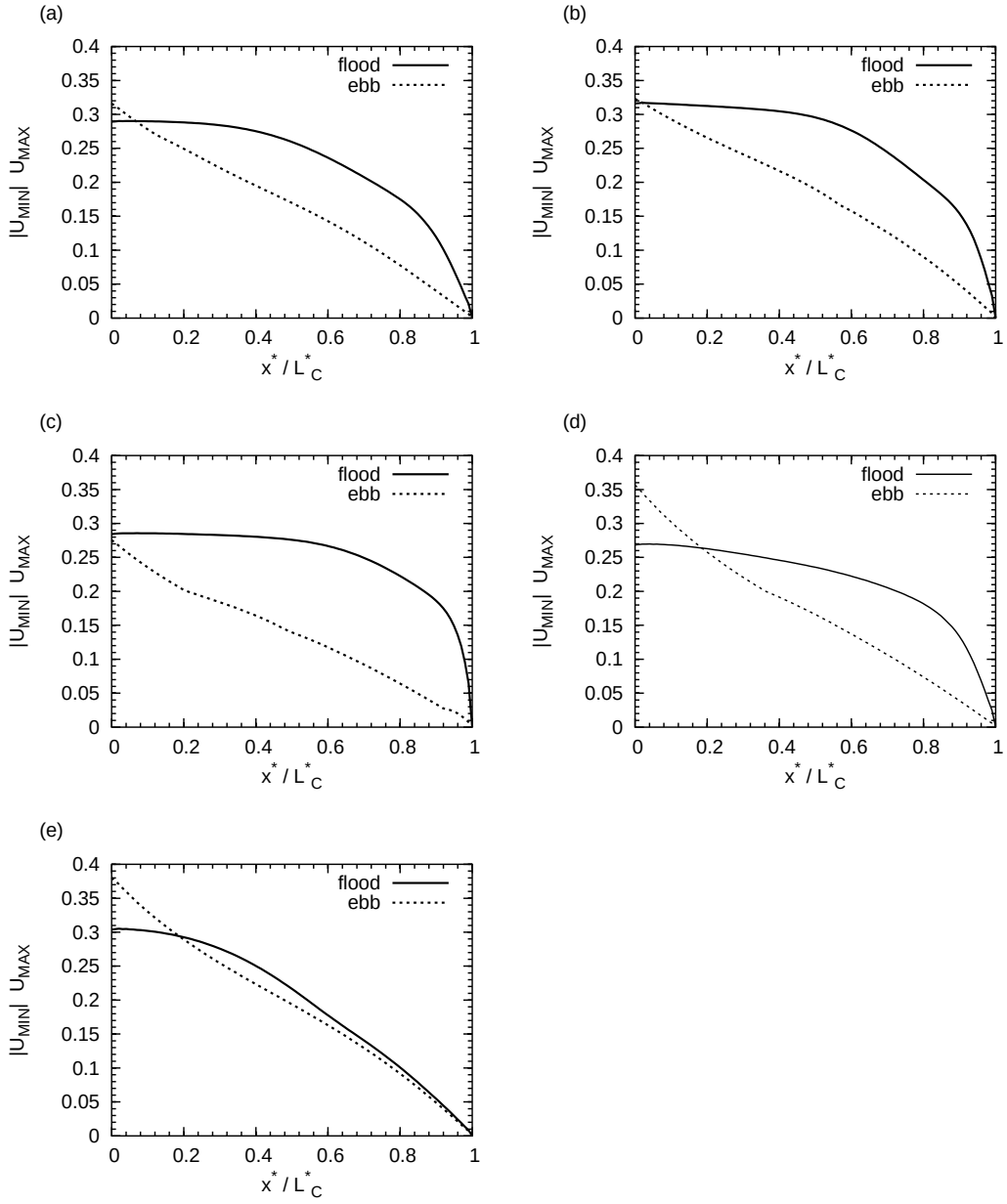

Figure 2.13: Comparisons between the maximum velocity during the flood and ebb phases in the initial flat configuration of a tidal channel for different values of the phase lag ϕ between the M_2 and the M_4 components of the tidal oscillation at the sea. The ratio between the amplitudes of the M_2 and the M_4 components is 0.2. (a) M_2 only, (b) $\phi = 0$, (c) $\phi = \pi/4$, (d) $\phi = \pi/2$, (e) $\phi = -\pi/4$.

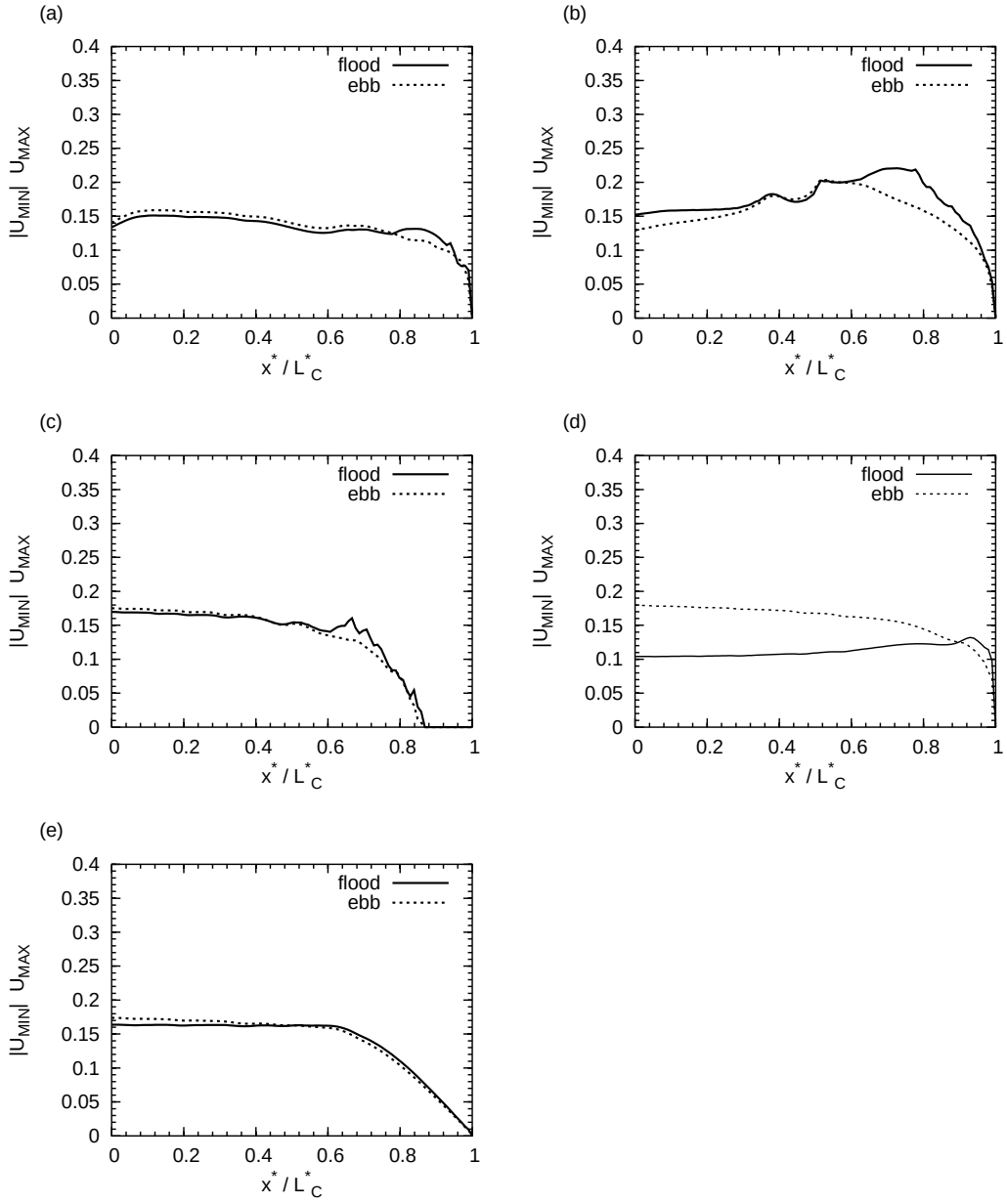

Figure 2.14: Comparisons between the maximum velocity during the flood and ebb phases at the equilibrium configuration of a tidal channel for different values of the phase lag ϕ between the M_2 and the M_4 components of the tidal oscillation at the sea. The ratio between the amplitudes of the M_2 and the M_4 components is 0.2. (a) M_2 only, (b) $\phi = 0$, (c) $\phi = \pi/4$, (d) $\phi = \pi/2$, (e) $\phi = -\pi/4$.

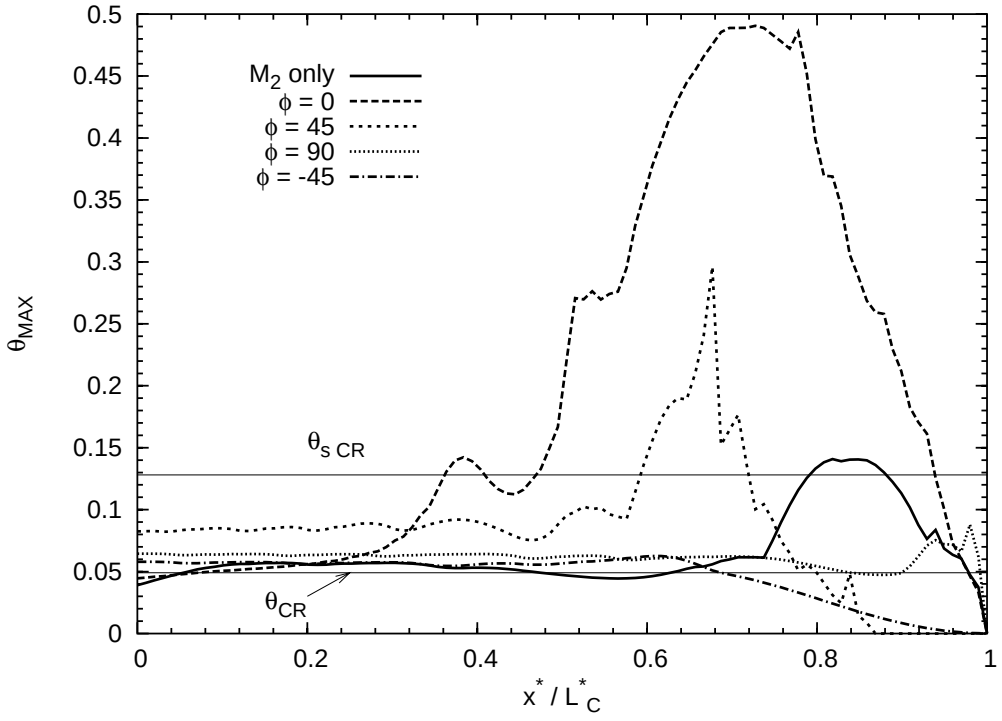

Figure 2.15: Comparisons between the maximum Shields stress over a tidal cycle at the equilibrium configuration of a tidal channel for different values of the phase lag ϕ between the M_2 and the M_4 components of the tidal oscillation at the sea. The ratio between the amplitudes of the M_2 and the M_4 components is 0.2.

stress attains the threshold conditions for sediment motion in accordance with *Marchi*'s [1990] assumption. However, the effect of overtides as well as of an excess of sediment supply as discussed below, may alter the above picture. In fact, Figure 2.15 shows that for $\phi = \pi/4$, $\phi = \pi/2$ and $\phi = -\pi/4$ the maximum Shields stress at the inlet over a tidal cycle falls above the threshold conditions for sediment motion.

2.6 Results: the settling lag effect

As pointed out previously, we have employed a model of transport in suspension, described in the previous chapter, suitable to flow fields which are slowly varying in time and space.

In order to fully appreciate the role of non equilibrium of sediment transport, a simple application of this approach to an idealized context, consisting of a frictionless tidal channel closed at one end and subject to tidal forcing at the inlet, proves instructive.

More precisely, in order to make quantitative estimates, let us consider a channel with length $l^* = 10\ km$, constant mean depth $D_0^* = 5\ m$ and median grain size $d_{50} = 0.1\ mm$. The channel, closed at the landward end, is forced by a semidiurnal tide of amplitude $a^* = 1.4\ m$ at the mouth.

The solution of the 1D continuity and momentum equations, linearized assuming small tidal oscillations and vanishing friction, takes the following simple analytical dimensionless form:

$$h(x^*, t^*) = \frac{h^*(x^*, t^*)}{D_0^*} = 1 + \frac{a^*}{D_0^*} \cos(\omega t^*) \frac{\cos[k(x^* - l^*)]}{\cos(kl^*)} , \quad (2.28)$$

$$U(x^*, t^*) = \frac{U^*(x^*, t^*)}{U_0^*} = \sin(\omega t^*) \frac{\sin[k(x^* - l^*)]}{\cos(kl^*)} , \quad (2.29)$$

where k is the tidal wave number $(2\pi/L)$, with L wave length, ω $(= 2\pi/T)$ is the angular frequency of the tidal wave, with T tidal period, x^* is a landward oriented axis with origin at the inlet, t^* is time and the scale used for the averaged flow velocity reads:

$$U_0^* = \frac{a^*}{D_0^*} \sqrt{g D_0^*} . \quad (2.30)$$

Figure 2.16 shows the dimensionless water surface elevation and the averaged flow velocities at different cross sections. Notice that the amplitude of the tidal wave does not increase significantly landward due to the small value attained by the ratio between the channel length and the tidal wave length

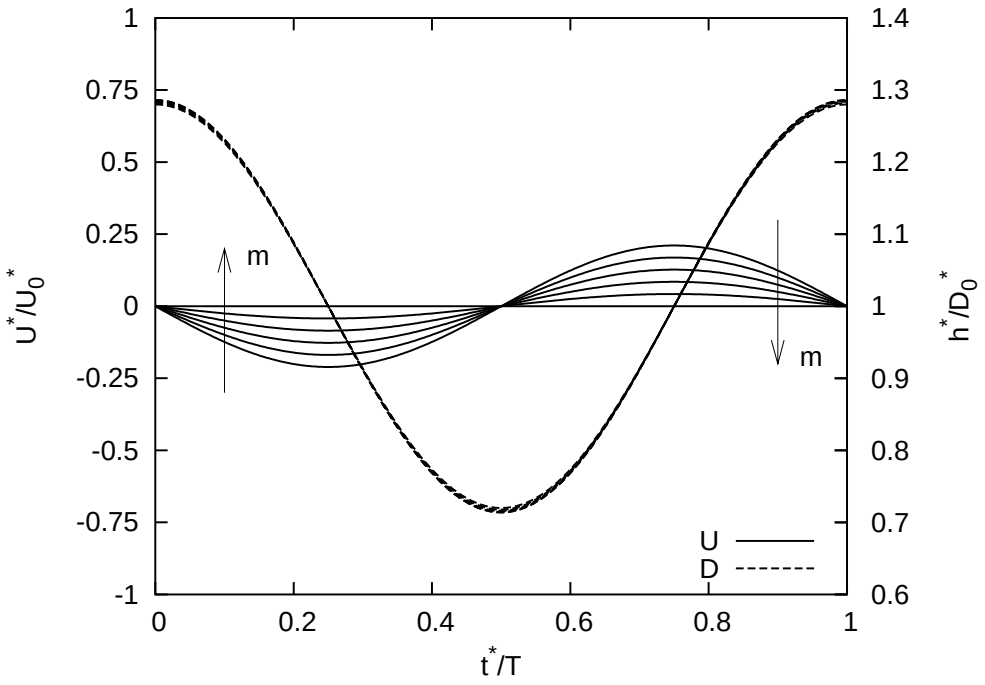

Figure 2.16: Dimensionless water depth (dashed lines) and dimensionless averaged flow velocity (continuous line) at distances $x^*/l^* = m/5$ $(m = 0, 5)$ from the inlet of the tidal channel.

$(l^*/L = 0.03)$. On the other hand, the averaged flow velocity decreases landward to reach a vanishing value at the landward cross section.

With the latter solution for the hydrodynamics, it is straightforward to derive the distribution of concentration using the approach described in the previous chapter. Figures 2.17 and 2.18 show a comparison between the vertical distribution of sediment concentration at the leading and first order approximations at different times. Note that, close to the instant where the sediments start to be driven into suspension by the current, the deviation from the Rouse profile is significant (Figure 2.17(a)) and decreases gradually during the ebb phase. On the contrary, Figures 2.18, referring to the flood phase, show that the deviation from the Rouse profile increases gradually throughout the flood phase. We have then evaluated the temporal distribution of the suspended sediment flux at the leading (q_{s0}) and first order of approximation $(q_{s0} + \delta q_{s1})$ at different cross sections. Figure 2.19 shows the values attained by the two contributions at the inlet cross section of the tidal channel. Note that, during the ebb phase the instantaneous value of the sediment flux is smaller than the 'equilibrium' suspended sediment flux. On the other hand, during the flood phase, the situation is reversed: the flux of sed-

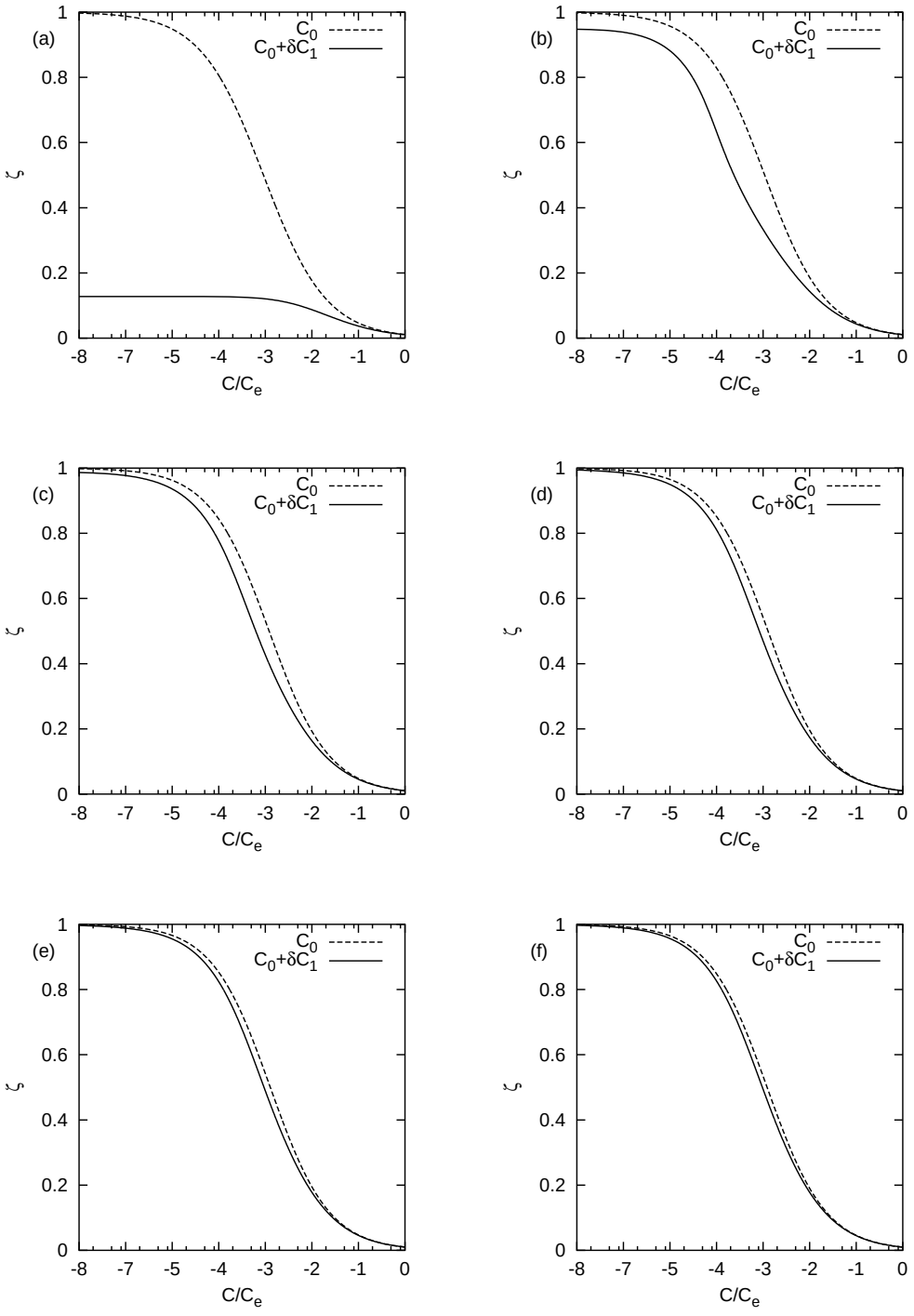

Figure 2.17: Vertical distributions of sediment concentration at leading and first order of approximations during the ebb phase at (a) $t^*/T = 0.194$, (b) $t^*/T = 0.208$, (c) $t^*/T = 0.222$, (d) $t^*/T = 0.236$, (e) $t^*/T = 0.25$, (f) $t^*/T = 0.264$.

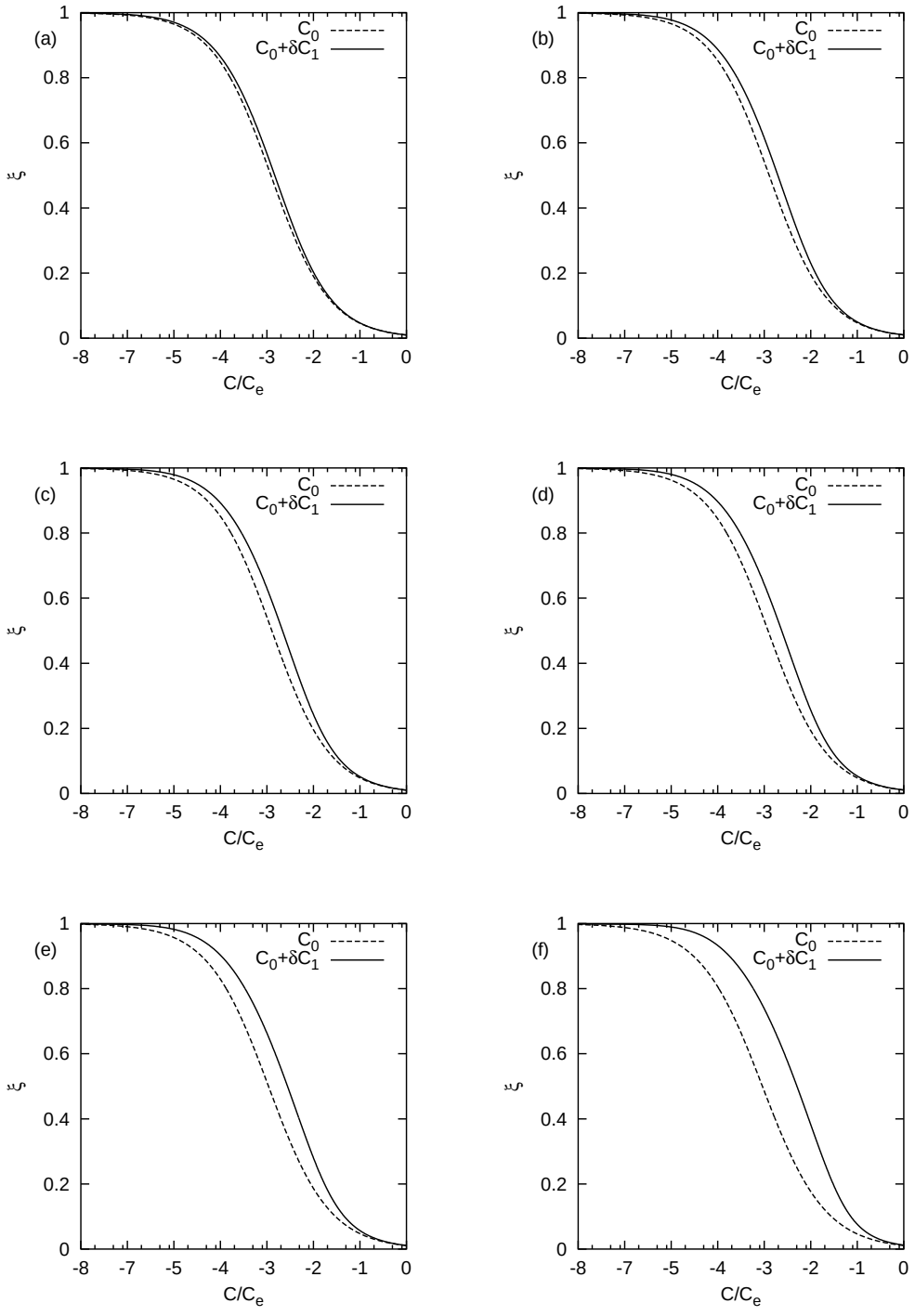

Figure 2.18: Vertical distributions of sediment concentration at leading and first order of approximations during the flood phase at (a) $t^*/T = 0.736$, (b) $t^*/T = 0.75$, (c) $t^*/T = 0.764$, (d) $t^*/T = 0.778$, (e) $t^*/T = 0.792$, (f) $t^*/T = 0.806$.

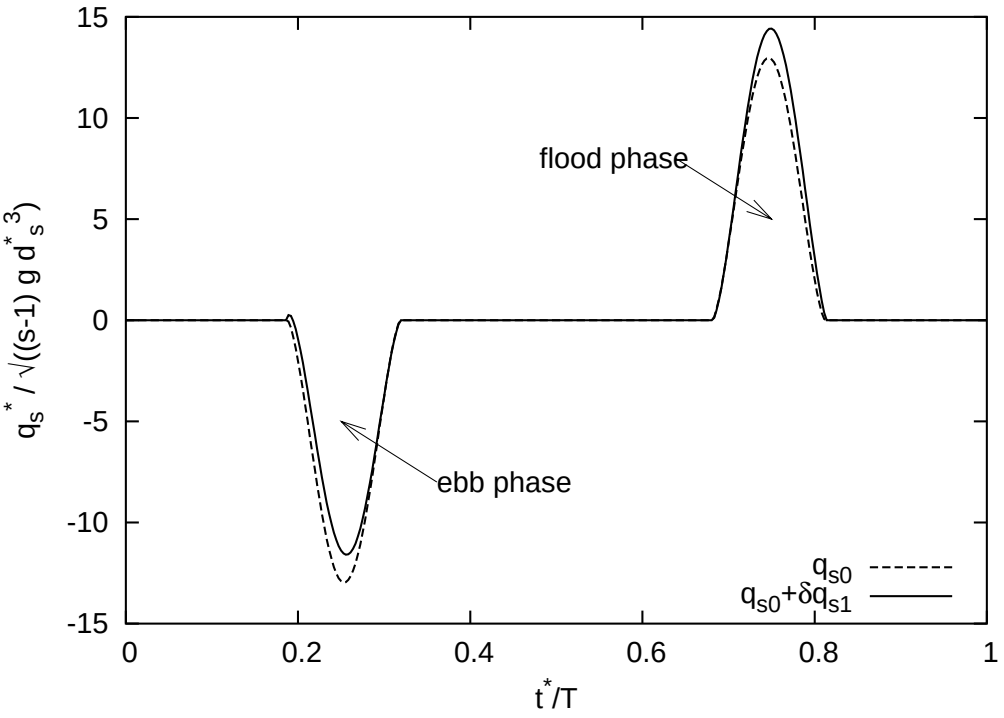

Figure 2.19: Comparison between the dimensionless suspended sediment flux per unit width at the leading (q_{s0}) and first order of approximation ($q_{s0}+\delta\ q_{s1}$) evaluated at the inlet cross section of the tidal channel.

iments is greater than the value attained under an 'equilibrium' assumption. Such asymmetry of the sediment flux gives rise to a net sediment flux over a tidal cycle which would not arise in the context of a scheme based on the classical 'equilibrium' assumption. Such findings are reported in Figure 2.20 which shows a comparison between the volume per unit width exchanged at the inlet cross section at the leading ($O(\delta^0)$) and first order of approximation ($O(\delta)$). Note that the net sediment flux ($< q_{s0} >$) vanishes at leading order, while the $O(\delta)$ corrections give rise to a landward directed net sediment flux in a tidal cycle. Also note that the most relevant contribution to the deviation from the equilibrium sediment flux is due to the spatial variation of the average concentration (Figure 2.21). One may envisage that such effect, though small ($O(\delta)$), can play a significant role when investigating the long term morphodynamic equilibrium of tidal channels, whenever the channel does not exhibit a significant flood or ebb dominant character, like in the simple model discussed above. On the contrary, the application of the model of transport in suspension to another simple idealized context, consisting of a frictionless infinite tidal channel subject to tidal forcing at the inlet, leads

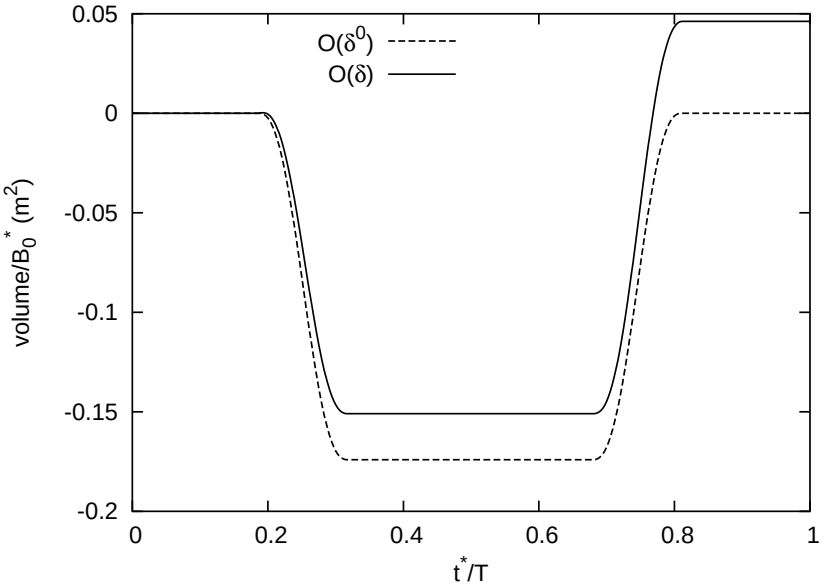

Figure 2.20: Comparison between the temporal evolution of the sediment volume per unit width exchanged at the inlet cross section of the tidal channel at the leading ($O(\delta^0)$) and first order of approximation ($O(\delta)$).

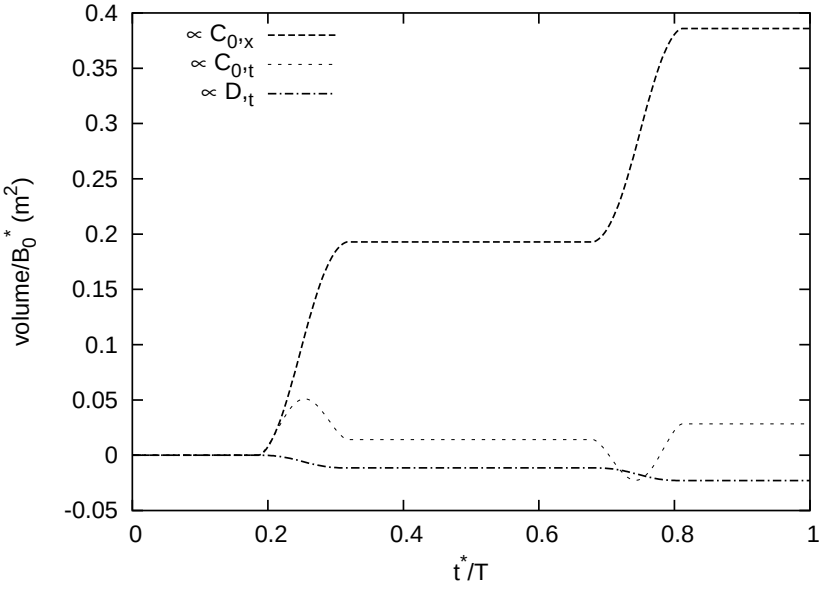

Figure 2.21: Contribution to the deviations from the equilibrium suspended sediment flux (see equation 2.23) at the inlet cross section of the tidal channel.

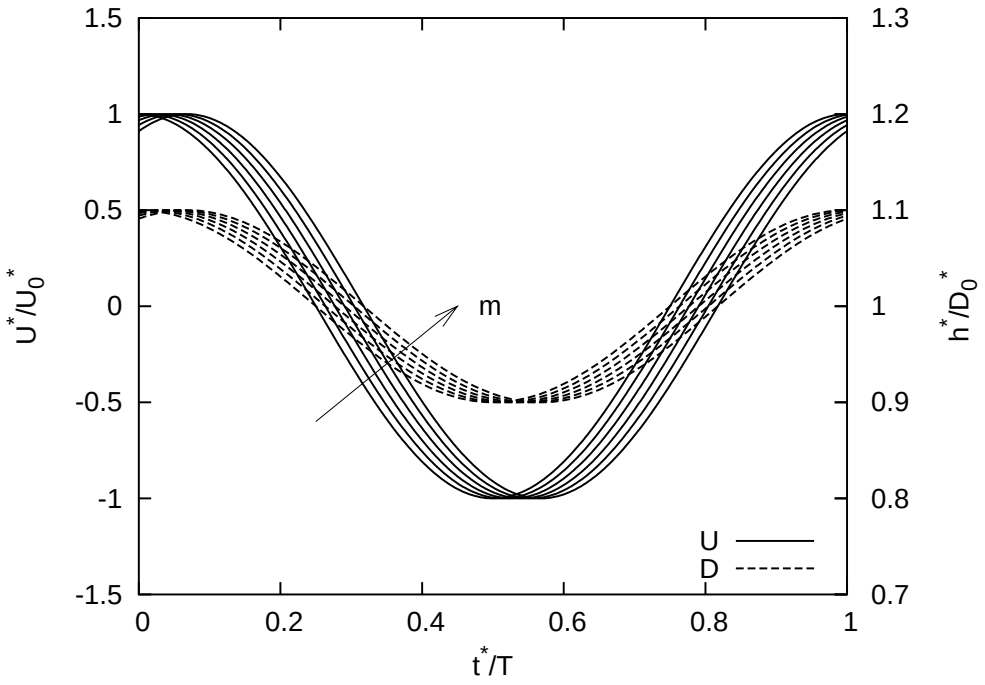

Figure 2.22: Dimensionless water level (dashed lines) and dimensionless averaged flow velocity (continuous line) at different distances from the inlet cross section of the tidal channel [$x^* = m * 10km$ $(m = 0, 5)$].

to a different picture.

Again, in order to make quantitative estimates, let us consider the tide propagation of a frictionless infinite tidal channel with constant mean depth $D_0^* = 30\ m$, median grain sediment size $d_{50} = 0.1\ mm$ forced by a semidiurnal tide of amplitude $a^* = 3\ m$ at the mouth.

The solution of the 1D continuity and momentum equations, linearized assuming small tidal oscillations and vanishing friction, takes the following simple analytical dimensionless form:

$$h(x^*, t^*) = \frac{h^*(x^*, t^*)}{D_0^*} = 1 + \frac{a^*}{D_0^*} \cos(\omega t^* - k x^*) \ , \tag{2.31}$$

$$U(x^*, t^*) = \frac{U^*(x^*, t^*)}{U_0^*} = \cos(\omega t^* - k x^*) \ . \tag{2.32}$$

Figure 2.22 shows the dimensionless water surface elevation and averaged flow velocities at different cross sections. Notice that the amplitude of the tidal wave keeps unchanged propagating landward and the water surface elevation is in phase with the averaged flow velocity. Clearly the channel does

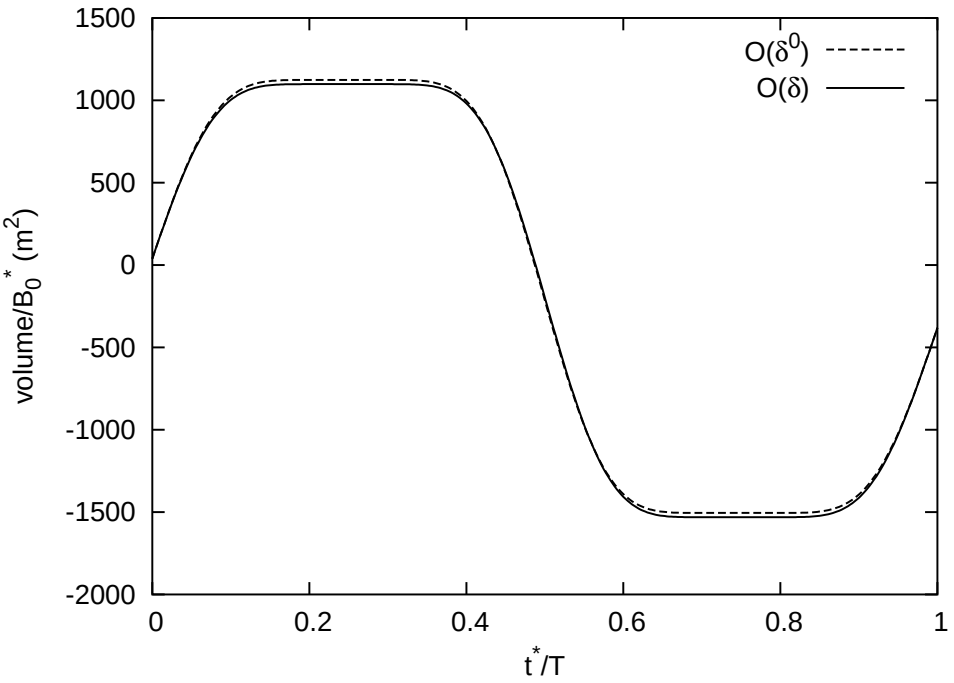

Figure 2.23: Comparison between the sediment volume per unit width exchanged at the inlet cross section of the tidal channel at the leading ($O(\delta^0)$) and first order of approximation ($O(\delta)$).

not exhibit either a flood or ebb dominant character, like in the simple model discussed above, but the symmetry of the flood and ebb phases does not apply to Shields stress due to the weak dependence of the latter on the flow depth. In fact, during the ebb phase, the Shields stress attains a greater value than in the flood phase, determining a net flux of suspended sediment over a tidal cycle even at the leading order of approximation (Figure 2.23). Consequently, in this case, the corrections to the equilibrium suspended sediment flux does not play a crucial role in terms of net sediment flux and just contribute to decrease the amount of sediment entering the channel during the flood phase and increasing the amount of sediment flux leaving the channel during the ebb phase.

Finally, the application of the model to the long term morphodynamic equilibrium of tidal channels confirms the above picture. Figure 2.24 shows a comparison between the longitudinal bottom profiles of the channel at different times both in the case when the effects of settling-lag and local variation of concentration are accounted for and when they are neglected. It is apparent that, in this case, non-equilibrium effects play a negligible role

throughout the evolution of the channel and simply lead to a weaker erosion of the channel inlet compared with that predicted using a Rousean approach. This result is not surprising as we have seen that tide propagation in such channels exhibits a marked ebb dominant character in its seaward portion and flood dominance landward. Hence, a significant net sediment flux in a tidal cycle arises at leading order and the order δ corrections turn out to be negligible. On the other hand, approaching equilibrium, both $< q_{s0} >$ and $< q_{s1} >$ tend to vanish and the O(δ) contributions are again negligible.

2.7 Results: sediment exchange at the inlet

The exchange of sediments through channel inlets in the field results from a complex phenomenon where various factors may play a significant role. In particular, let us mention two of them, which seem to be of prevailing importance:

1. the hydrodynamics of the inlet region and in particular its ebb-flood asymmetry, which strongly depends on the inlet shape;

2. the availability of sediment in the far field, a feature depending on the wave climate and on the presence of littoral currents.

Evaluating the above effects requires the development of a complete morphodynamic model of the inlet region, a goal which we intend to pursue in the near future through the extension to the mobile bed case, of the fixed bed approach developed by *Blondeaux et al.* [1982].

In the present model we have attempted to get some semiquantitative estimate of the exchange of sediments between the channel and the sea and its effect on the long term equilibrium of tidal channels through a simplified model, already described above, whereby the sediment flux during the ebb phase is assumed to be determined by the transport capacity of the stream at the inlet section, while the sediment flux during the flood phase is simply driven by some fixed sea concentration. Most of the results presented below have been obtained assuming that the sea sediment concentration is in equilibrium with the local hydrodynamic conditions; a different choice will be explicitly specified.

Figure 2.25 represents the effect of an excess or defect of sediment supply from the sea on the long term equilibrium of tidal channels. In the case of defect of sediment supply from the sea, it has been assumed that, during the flood phase, there was no sediment flux fed from the sea, imposed by setting the sea concentration to vanish. In nature, this situation could be

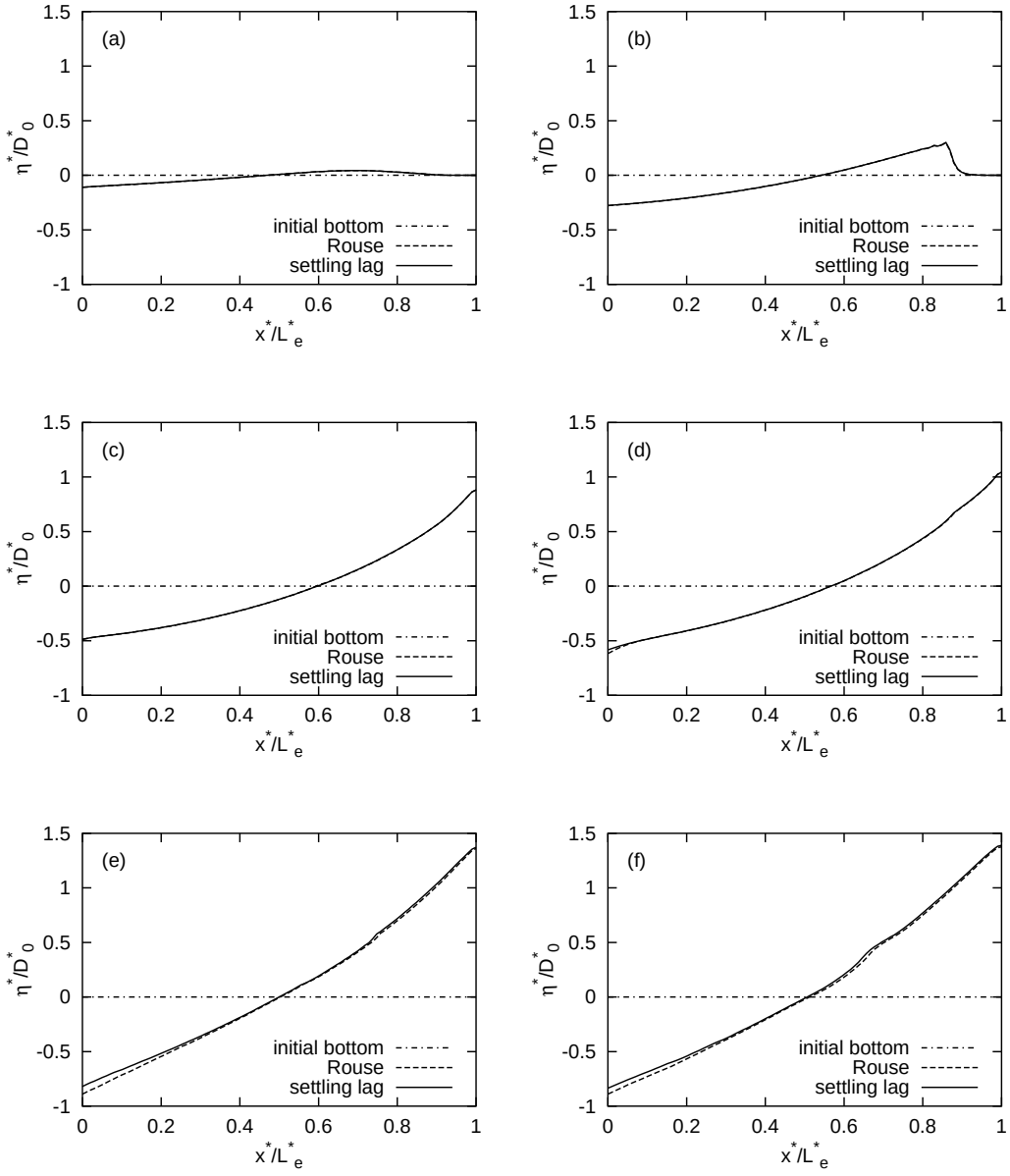

Figure 2.24: Comparison between the longitudinal bottom profiles of the channel at different times in the case in which the effects of settling-lag and local variation of concentration are accounted for (solid lines) or neglected (dotted lines). (a) $t^* = 20\,T$, (b) $t^* = 100\,T$, (c) $t^* = 500\,T$, (d) $t^* = 1000\,T$, (e) $t^* = 5000\,T$, (f) $t^* = 20000\,T$.

representative of a tidal environment connected to the sea through inlets protected by jetties which extend to deep water where currents induced by the wave motion are too weak for sediment transport to occur. On the other hand, an excess of sediment supply from the sea has been modelled stipulating that the sediment flux from the sea was slightly greater than the equilibrium sediment flux corresponding to the initial state. Such constraint was imposed by setting the sea concentration at a fixed value, greater than the value attained by the peak concentration in equilibrium with the local hydrodynamics during the first tidal cycle. Note that an excess of sediment supply from the sea induces sediment deposition but does not prevent the channel to reach a new equilibrium configuration. On the other hand, a deficient exchange of sediments with the sea leads to an equilibrium profile quite close to that obtained on the basis of the equilibrium assumption.

Figure 2.26 shows the maximum Shields stress over a tidal cycle at the equilibrium configuration in the case of an excess or defect of sediment supply from the sea. Notice that, assuming an 'equilibrium' sea sediment concentration and neglecting overtides in the tidal forcing, the model suggests that inlet equilibrium is reached when the bottom shear stress attains the threshold conditions for sediment motion in accordance with *Marchi*'s [1990] assumption. However, an excess of sediment supply as well as the effect of overtides as discussed in previous sections, may alter the above picture. In fact in the case of an excess of sediment supply from the sea the maximum Shields stress over a tidal cycle falls above the threshold conditions for sediment motion at the inlet.

Examples of potential applications of the present model to realistic situations are reported in the Figures 2.27 and 2.28 showing respectively the effects of a sudden increase or decrease of sediment supply from the sea starting from an equilibrium bottom profile. In nature, the situation reported in Figure 2.27 could be representative of jetty removal or reshaping of the inlet in order to increase the sediment supply to the tidal channel during the flood phase. Note that the new equilibrium configuration is characterized by an intense deposition along the channel reaching its maximum value at the inlet section where the aggradation is of the same order of magnitude of the mean flow depth D_0^*. The time scale of such phenomenon is of the order of hundreds of years.

The reversed situation is reported in Figure 2.28 showing the effects of a sudden decrease of sediment supply from the sea starting from an equilibrium bottom profile. In nature, such situation could be representative of the construction of jetties or reshaping the inlet such to decrease the sediment supply to the tidal channel during the flood phase or increasing the depth at the inlet for navigation purposes. As expected, the new equilibrium configu-

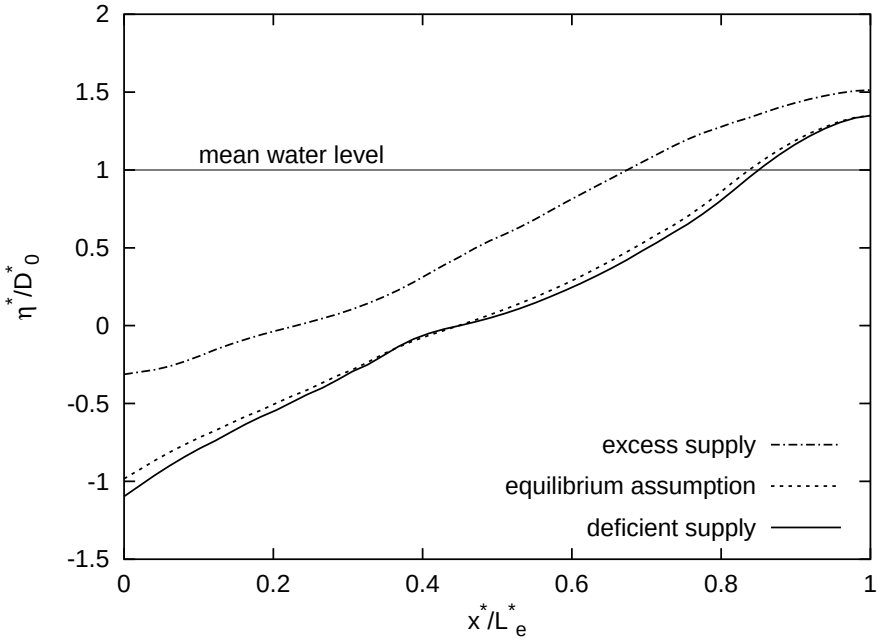

Figure 2.25: Effect of an excess or defect of sediment supply from the sea on the long term equilibrium of tidal channels.

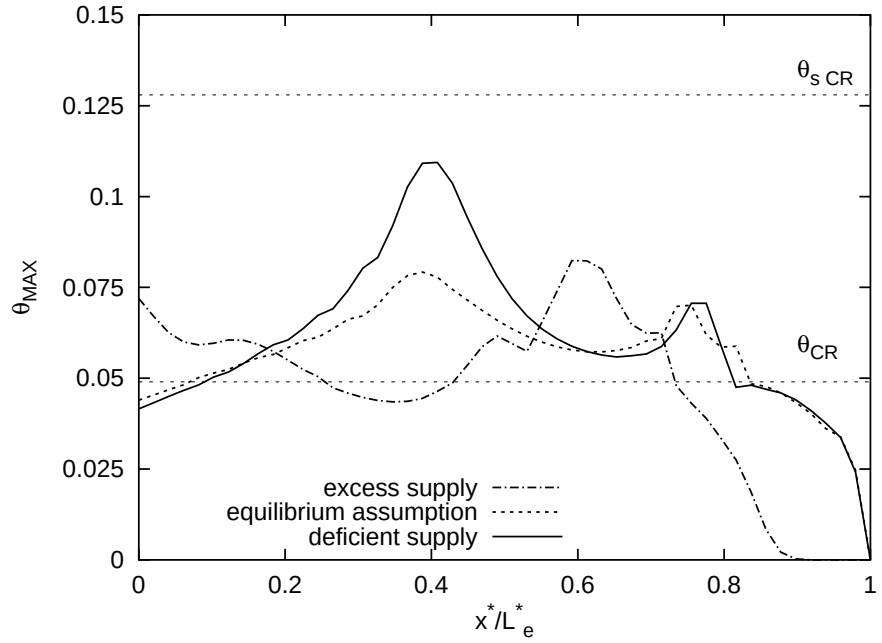

Figure 2.26: Effect of an excess or defect of sediment supply from the sea on the maximum Shields stress over a tidal cycle at the equilibrium configuration of a tidal channel.

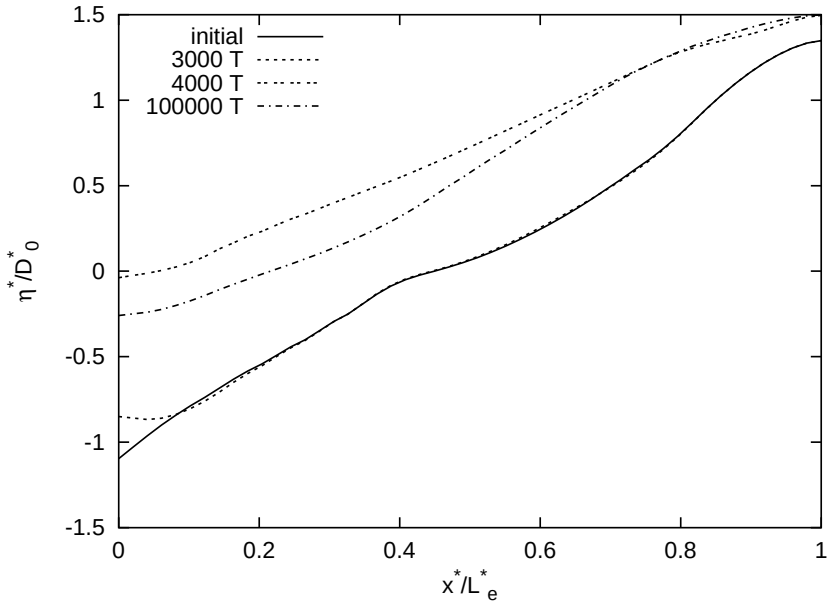

Figure 2.27: Effect of an excess of sediment supply from the sea on the long term equilibrium of tidal channels starting from an equilibrium profile which was determined imposing a defect of sediment supply at the inlet.

ration is characterized by scouring along the channel showing its maximum value at the inlet section. Again the time scale of the erosive phenomenon is of the order of hundreds of years.

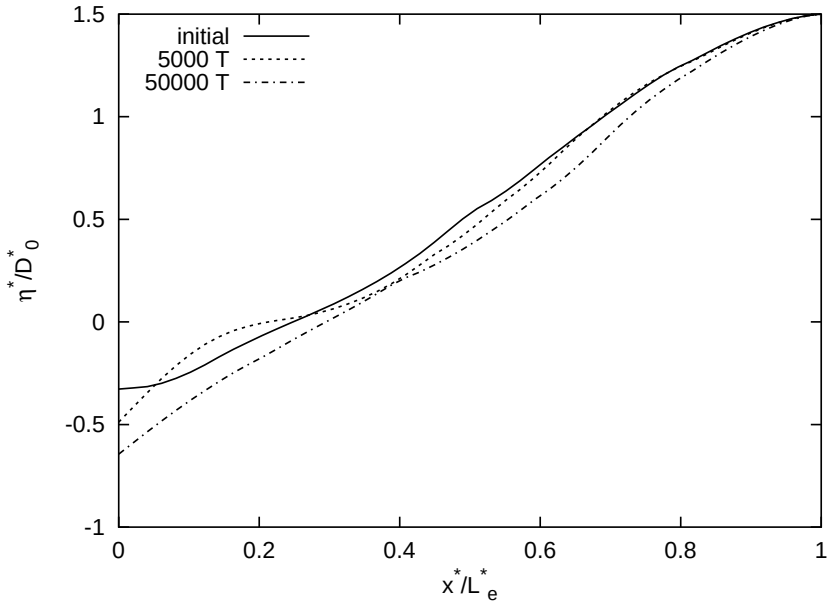

Figure 2.28: Effect of a deficient sediment supply from the sea on the long term equilibrium of tidal channels starting from an equilibrium profile which was determined imposing an excess sediment supply at the inlet.

Chapter 3

Long term morphodynamic equilibrium of tidal channels. Laboratory observations

The chapter reports on a laboratory investigation of the process whereby an equilibrium bed profile is established in tidal erodible channels. The recent theoretical results of *Lanzoni and Seminara* [2002] and those discussed in the previous chapter, (but see also *Bolla Pittaluga* [2003]) suggest that tidal channels closed at one end and connected at the other end with a tidal sea can achieve a morphodynamic equilibrium characterized by an upward concave bed profile seaward and by a convex profile landward, vanishing net sediment flux in a tidal cycle at each cross section and the formation of a 'beach' close to the landward end of the channel. Such results are confirmed by the present laboratory observations. The morphodynamic evolution and equilibrium of the inlet is also investigated and appears to be strongly affected by its shape. Sharp inlets give rise to strong ebb currents able to excavate a submerged channel which affects the flow field, modifying its quasi-2D irrotational character during the flood phase, i.e. reducing the degree of the ebb - flood flow asymmetry observed and predicted in the fixed bed case by *Blondeaux et al.* [1982]. On the contrary, smoothly diverging inlets appear to give rise to the mechanism typically associated with shallow flows with diverging streamlines: a large depositional area, i.e. a sort of elongated central bar in the form of a 'delta', develops in the 'sea' region close to the inlet. Further interesting observations emerge on the formation of large and small scale bedforms. In particular, the formation of tidal ripples is observed both in the channel and in the 'sea basin': scaling arguments indicate that the observed forms are indeed ripples (rather than dunes) and suggest their 'fluvial' rather than 'coastal' nature. Free bars, i.e. a class of those large scale

forms called 'repetitive barforms' by *Dalrymple and Rhodes* [1995], form in the channel close to the tidal inlet in each experiment, in accordance with recent theoretical predictions of *Seminara and Tubino* [2001].

3.1 Introduction

While attempts to determine the long term morphodynamic equilibrium of tidal channels on a theoretical basis have recently been proposed [*Schuttelaars and de Swart*, 1996, 2000; *Lanzoni and Seminara*, 2002; *Bolla Pittaluga*, 2003; Chapter 2], no attempts to pursue the same goal on the basis of controlled laboratory observations are known to the present author. This is not surprising as the time scale of morphodynamic evolution is typically much larger than the hydrodynamic time scale. Moreover, the evolution becomes slower and slower as equilibrium is approached: hence, as it will appear from the scaling arguments and from the experimental observations discussed below, the time required to approach conditions sufficiently close to equilibrium in the laboratory is of the order of days or weeks.

Nonetheless, in spite of its complexity, such experimental exercise proves worth pursuing. In fact, it allows to check, under controlled conditions referring to simple channel geometries, the main mechanisms controlling the morphodynamic evolution of tidal channels emerged from the theoretical works mentioned above, a goal quite difficult to achieve on the basis of field observations whose interpretation is generally complicated by the simultaneous presence of a variety of further natural features whose role cannot be readily isolated.

Let us then recall some of the recent theoretical predictions that require some experimental verification.

We move from results obtained in *Lanzoni and Seminara* [2002] as well as by [*Bolla Pittaluga*, 2003; Chapter 2] where the morphodynamics of a straight, convergent channel closed at one end and connected at the other end with a tidal sea, has been investigated theoretically. The analyses lead to establishing some apparently well defined results, which can be summarized as follows.

1. Starting from an initially flat bed profile such that the tidal motion is able to transport sediments, a slow evolution of bottom topography occurs due to the feedback effect of the latter on the shape of the tidal wave: a sharp front forms, migrates landward and leads to the emergence of the bed at the inner boundary with the formation of a dry and wet region. Eventually, an equilibrium bed profile is reached, which is upward concave seaward and slightly convex landward.

2. Equilibrium is associated with vanishing net sediment flux in a tidal cycle at any cross section but this does not imply that the instantaneous sediment flux vanishes, though transport is generally very weak at equilibrium. As the latter conditions are reached a linear relationship of Jarret type between minimum cross sectional area and tidal prism is found to hold throughout the channel [*Lanzoni and Seminara*, 2002].

3. The equilibrium depth established at the inlet cross section depends only on channel geometry and tidal forcing.

4. The role of overtides possibly present in the tidal forcing may affect significantly the equilibrium profile, depending on their amplitude and phase relative to the fundamental component [*Bolla Pittaluga*, 2003; Chapter 2].

5. The exchange of sediments forced by the inlet hydrodynamics also affects the equilibrium configuration significantly and points out the important role played by the inlet geometry.

6. The role of non equilibrium of sediment transport does not appear to be crucially important [*Bolla Pittaluga*, 2003]. In other words the assumption employed by *Lanzoni and Seminara* [2002], whereby sediment transport was taken to be in equilibrium with the local and instantaneous hydrodynamic conditions is not found to be too severe.

A second set of theoretical predictions are relevant to the present laboratory observations. In a recent paper [*Seminara and Tubino*, 2001] the mechanism which controls the formation of free bars, i.e. those large scale bedforms observed in estuaries and lagoons called repetitive bar forms by *Dalrymple and Rhodes* [1995], were investigated. In particular, it turned out that the formation of tidal bars arises from an instability of the cohesionless bed, conceptually similar to the well known mechanism underlying the formation of fluvial bars. The unsteady, oscillatory character of tidal flow prevents bar migration, except for a weak propagation possibly driven by the presence of residual currents. Essentially, bars form whenever the aspect ratio of the channel exceeds a threshold value depending mainly on the intensity of sediment transport measured by the so called Shields parameter. In the tidal case the threshold value of the aspect ratio ranges about few units. The theory is also able to predict the most unstable bar wavelength, which ranges typically about few channel widths.

At a smaller scale, the present laboratory observations also allow to observe the formation of tidal ripples. The actual nature of such forms, in other

words the fact that they must be identified as ripples rather than dunes, will be discussed below. Moreover, it will appear that ripples are washed out when suspended load reaches its peak while their presence persists throughout the tidal cycle when transport is weaker and dominantly occurs as bedload.

Finally, the two experiments described below show that the inlet morphodynamics is strongly dependent on the inlet geometry. Sharp inlets give rise to a strong ebb current, characterized by large scale coherent structures arising from a quasi 2D instability of the shear layer. The current is able to excavate a submerged channel which affects the flow field modifying its quasi - irrotational character during the flood phase, thus reducing the degree of the ebb - flood flow asymmetry observed and predicted in the fixed bed case by *Blondeaux et al.* [1982]. On the contrary, smoothly diverging inlets give rise to a depositional process typical of shallow flows with diverging streamlines: such process leads to the development of a large scale elongated bar, a sort of 'delta', in the 'sea' region close to the inlet. The morphodynamic evolution of the inlet region affects significantly also the morphodynamic evolution of the channel: in fact, it will appear that a net flux of sediments is exchanged through the inlet throughout the experiment. This has some implications, discussed below, on the boundary conditions required in analytical models of the morphodynamic evolution of tidal channels.

The theoretical foundation of the scaling arguments underlying the physical conditions reproduced in the experiments are discussed in the next section. Sect. 3.3 is devoted to a brief description of the experimental apparatus, while sect. 3.4 reports results of the first experiment, performed on a constant width channel with a sharp inlet. The distinct effect of channel divergence and of the smooth shape of the inlet are reproduced in the second experiment, which is discussed sect. 3.5. Sect. 3.6 concludes the chapter with some discussion and concluding remarks.

3.2 Scaling arguments and similarity rules.

Physical models are based on scaling rules constructed by imposing that all the relevant dimensionless parameters governing the phenomenon keep the same value in the model and in the prototype. Referring to the dimensionless formulation of the hydrodynamic and morphodynamic problems reported in the previous chapter, scaling factors can be introduced as follows (the apex refers to the model):

$$\lambda = \frac{D_0^*}{D_0^{*\prime}}; \qquad \varphi = \frac{U_0^*}{U_0^{*\prime}}; \qquad \tau = \frac{t^*}{t^{*\prime}}; \qquad \lambda_b = \frac{L_b^*}{L_b^{*\prime}}; \tag{3.1}$$

$$\delta = \frac{d_s^*}{d_s^{*\prime}}; \qquad \sigma = \frac{s-1}{s'-1}; \qquad \chi = \frac{C_0}{C_0{}'}, \tag{3.2}$$

where λ, φ, τ represent the length, velocity and time scales respectively, λ_b is the scale of the 'convergence' length, δ is the scale of grain size, σ is the scale of relative density and χ is the scale of flow conductance. The reader will note that the model considered herein is necessarily distorted: distortion is required as it proves impossible to find cohesionless natural sediments as small as it would be required if the same scaling factor λ characterizing the spatial scales involved in the hydrodynamics were used for sediment size. The size distortion will be somehow compensated by a simultaneous distortion of the relative density of sediments, achieved by choosing a granular material much lighter than quartz. In the present experiments we have employed crashed hazelnuts shells ($s = 1.4$).

It is convenient at this stage to distinguish between the scaling rules appropriate to model strongly ($\mathcal{R}/\mathcal{S} \gg 1$) and weakly ($\mathcal{R}/\mathcal{S} \ll 1$) dissipative tidal channels.

3.2.1 Weakly dissipative tidal channels

Tidal channels characterised by large flow depths and low friction coefficients, are not uncommon in nature. This limiting behaviour is mathematically described by the condition that $\mathcal{R} \ll \mathcal{S}$, which implies that gravity, driving the tidal wave, must be dominantly balanced by local inertia, the effect of friction (and often also of convective inertia) being negligible.

Let us then go back to eq. 2.4. Here, the contribution of spatial variations of H is of order ϵ, hence the latter balance is achieved by setting $\mathcal{S}$ equal to one and expressing the $\mathcal{F}$ parameter as a function of $\mathcal{S}$ as follows:

$$\mathcal{F} = \frac{F_0^2}{\epsilon^2} \cdot \frac{1}{\mathcal{S}} = \frac{F_0^2}{\epsilon^2} \ . \tag{3.3}$$

Dynamic similarity then requires:

$$\frac{\mathcal{F}}{\mathcal{F}'} = \frac{F_0^2}{F_0{}'^2} \cdot \frac{\epsilon'^2}{\epsilon^2} = \frac{\varphi^2}{\lambda e^2} = 1 \ . \tag{3.4}$$

A complete dynamic similarity would also require that the dimensionless parameter ($\epsilon\mathcal{S}\mathcal{F}$) multiplying the convective term in the momentum equation be also conserved. We cannot impose such further constraint, but we rely on the fact that convective effects play usually (though not always) a fairly minor role in tide propagation: hence, a rough reproduction of such effects is unlikely to modify the similarity of the morphodynamic pattern significantly.

Sediment transport similarity also requires:

$$\frac{\vartheta}{\vartheta'} = \frac{\varphi^2}{\chi^2 \sigma \delta} = 1 \ , \qquad \frac{R_p}{R_p{}'} = \sigma^{1/2} \delta^{3/2} = 1 \ . \tag{3.5}$$

The reader should note that, keeping the Shields parameter ϑ and the particle Reynolds number R_p constant in the model and in the prototype, automatically insures that the Rouse number Z is also conserved. In fact, the latter dimensionless parameter can be readily written in the form:

$$Z = \frac{W_s}{k u_*} = \frac{\widehat{W}_s}{k \sqrt{\vartheta}} \ , \tag{3.6}$$

having set

$$\widehat{W}_s = \frac{W_s}{\sqrt{(s-1)\, g d_s^*}} \tag{3.7}$$

Since the dimensionless form of the settling speed W_s, defined by equation (3.7), is known to be a function of particle Reynolds number, it follows that Z is essentially the ratio between a function of R_p and the square root of the Shields stress ϑ. The relationships (3.4) and (3.5) can be rearranged in the form:

$$e\sqrt{\lambda} = \chi \sigma^{1/3} \ , \qquad \varphi = \chi \sigma^{1/3} \ , \qquad \delta = \sigma^{-1/3} \ . \tag{3.8}$$

A further constraint should be strictly imposed: in order to insure that advective effects be equally small both in the model and in the prototype, the parameter δ defined by equation (2.16) should also be conserved, which would require that $\varphi = w$, having denoted by w the scaling factor for the settling speed. Such constraint is clearly redundant, which implies that some distortion of advective effects is unavoidable in the model. However, such approximation does not appear to be too severe in the light of the observations made at the end of the last Chapter, which suggest the relatively minor role of sediment advection. Sediments used in our model are characterised by a median grain size $d_{50}^* = 0.31\ mm$ and density of 1480 kg/m^3. Hence, assuming $\chi = 1$ (a reasonable assumption according to our experimental observations), from the relations (3.8) we find:

$$e\sqrt{\lambda} = 1.51 \ , \qquad \varphi = 1.51 \ , \qquad \delta = 0.66 \ . \tag{3.9a-c}$$

Once a scale factor λ has been chosen, the equation (3.9a) sets the ratio between the relative amplitudes of the forcing tide in the model and in the prototype: for example choosing a value of λ about 150, it follows that the dimensionless amplitude in the model is roughly 8 times larger than in the

prototype ($e = 0.123$). In other words, non linearity of the tidal wave in the prototype is much weaker than in the model.

Moreover, the exact reproduction of dissipative effects sets the scaling factor for the tidal period. In fact, recalling equations (2.6), we find:

$$\frac{\mathcal{R}/\mathcal{S}}{\mathcal{R}'/\mathcal{S}'} = \frac{\varphi\tau}{\lambda\chi^2} = 1 \ , \qquad \text{i.e.} \quad \tau = \frac{\lambda\chi^2}{\varphi} \ . \tag{3.10}$$

Unfortunately, the periods employed in the model are often constrained by the characteristics of the tide generating system. In particular, setting $\lambda = 150$ and $\chi = 1$, (3.10) would require $\tau = 100$, i.e. a period in the model of 430 s would be needed to reproduce an M_2 tide. We were unable to achieve sufficiently intense tidal currents with such a period and were then forced to use lower periods ($T = 180\ s$, $\tau = 240$) in the first experiment and $T = 120\ s$, $\tau = 360$ in the second experiment) which implies a distortion of the relative importance of dissipative effects in the model. In other words, a weakly dissipative model like that reproduced in our experiments corresponds to a moderately dissipative prototype.

Finally, the reproduction of the convergence of the tidal channel requires the further following condition:

$$\frac{\mathcal{K}}{\mathcal{K}'} = \frac{\lambda_b e}{\varphi\tau} = 1 \ , \qquad \text{i.e.} \quad \frac{\lambda_b}{\lambda} = \frac{\tau}{\sqrt{\lambda}} \ . \tag{3.11}$$

Using equation 3.11 the value of the convergence length characteristic of the model $\text{L}^{*\prime}_b$ can be determined.

3.2.2 Strongly dissipative tidal channels

Though our model of a tidal channel can be classified as weakly dissipative, it may be of interest to consider also the scaling rules applying to the strongly dissipative limiting case, as tidal channels characterised by low flow depths and large friction coefficients are most common in nature. This limiting behaviour is mathematically described by the condition ($\mathcal{R}/\mathcal{S} \gg 1$), which states that gravitational effects on tide propagation must be dominantly balanced by friction, while the effect of local inertia is negligible at leading order. The latter balance can be described by setting $\mathcal{R}$ equal to one and expressing the $\mathcal{F}$ parameter as follows:

$$\mathcal{F} = \frac{F_0^2}{\epsilon^2} \cdot \frac{U_0}{\omega^* D_0^* C_0^2} \cdot \frac{1}{\mathcal{R}} = \frac{F_0^2}{\epsilon^2} \cdot \frac{U_0}{\omega^* D_0^* C_0^2} \ . \tag{3.12}$$

Dynamic similarity then requires:

$$\frac{\mathcal{F}}{\mathcal{F}'} = \frac{\varphi^3 \tau}{\lambda^2 e^2 \chi^2} = 1 \ . \tag{3.13}$$

The latter relationships, along with those which insure the similarity of sediment transport give:

$$\tau = \frac{e^2 \lambda^2}{\chi \sigma} \ ; \qquad \varphi = \chi \sigma^{1/3} \ ; \qquad \delta = \sigma^{-1/3} \ ; \tag{3.14}$$

Using (3.14) one readily shows that the ratio $(\mathcal{R}/\mathcal{S}) \,/\, (\mathcal{R}'/\mathcal{S}')$ is typically greater than one: hence, if the model is strongly dissipative, the prototype is also strongly dissipative.

Observations similar to those made for the weakly dissipative case apply to the constraint concerning the need to reproduce the relative role of advection on the spatial and temporal distribution of the average concentration of suspended sediments.

Finally, the reproduction of the convergence of the tidal channel requires the further following condition:

$$\frac{\mathcal{K}}{\mathcal{K}'} = \frac{\lambda_b e}{\varphi \tau} = 1 \ , \qquad \text{i.e.} \quad \frac{\lambda_b}{\lambda} = \frac{e \lambda}{\sigma^{2/3}} \ . \tag{3.15}$$

Using equation 3.15 the value of the convergence length characteristic of the model $L^{*\prime}_b$ can be determined.

3.3 Experimental apparatus.

Experiments were carried out in the laboratory of the Department of Environmental Engineering of the University of Genova (Italy), on a large indoor platform 29.6 m long and 2.3 m wide. Above the platform a straight channel was built using a plastic material. The channel was closed at one end and connected at the other end to a rectangular basin representing the sea. Finally, an oscillating discharge was supplied to the basin from a feeding tank (1.50 x 3.08 x 1.76 m) in which the apparatus for tidal wave generation was installed. The latter consisted of a cylinder, with length of 2.8 m and diameter of 1.1 m (Fig. 3.1), set in motion by a piston held by a steel frame and controlled by an oleodynamic mechanism driven by a control system, which generated the desired law of motion. Such a law was first predicted theoretically by solving the differential equation:

$$A \frac{dh}{dt} = -\Omega(z) \frac{dz}{dt} + Q_{channel} \tag{3.16}$$

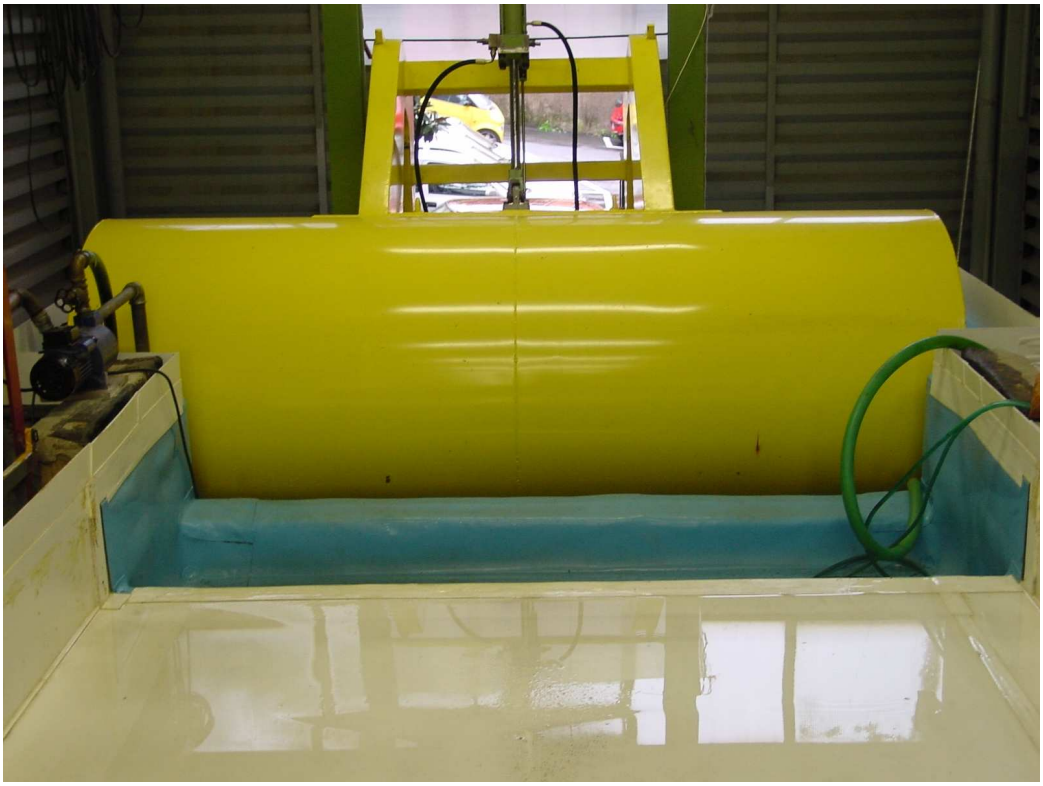

Figure 3.1: The floating cylinder and the adjacent 'sea basin'.

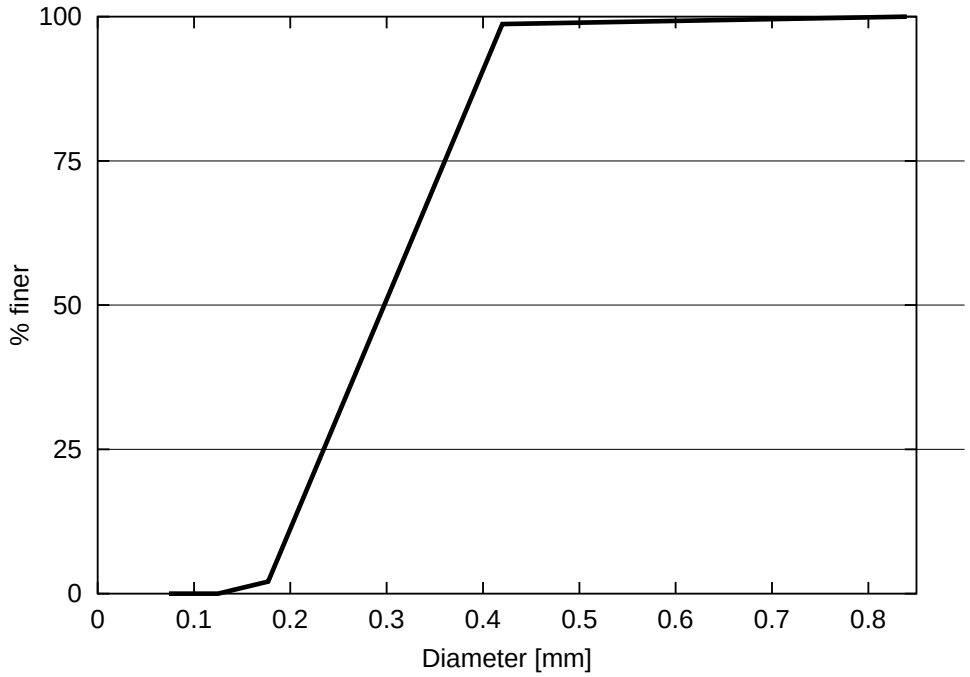

Figure 3.2: The grain size distribution of crashed hazelnuts employed as sediments in the physical model.

where A is the area of the free surface of the basin, Ω is the area of the intersection between the floating cylinder and the free surface of the basin, z is the elevation of the cylinder axis and $Q_{channel}$ is the flow discharge entering the basin through the channel inlet. The latter quantity was evaluated using a numerical solution of the hydrodynamic equations [*Lanzoni and Seminara*, 2002; *Bolla Pittaluga*, 2003]. The equation (3.16) was then solved numerically for $z(t)$ assuming the desired law $h(t)$ for the free surface oscillation in the basin. The required law of motion of the cylinder thus determined was then imposed through the control system.

A layer of cohesionless granular material of sufficient thickness was laid down on the bottom of both the flume and the basin. The granular material was chosen light enough to be entrained into suspension throughout most of the tidal cycle with the values of friction velocity typically generated in the present experiments. The final choice was to use crushed hazelnut shells characterised by a density of 1480 kg/m^3 and median grain size $d_{50}^* = 0.31\ mm$. The grain size distribution of such material was measured by sieving and is reported in Fig. 3.2. Tests were also made to ascertain the absence of cohesive effects.

Two experiments were performed using different geometrical settings for

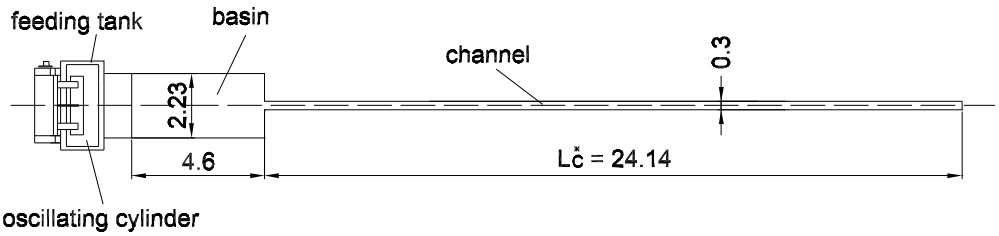

Figure 3.3: Sketch of the apparatus in the first experiment.

the channel and for the basin as well as different hydrodynamic conditions.

3.3.1 Experiment 1: straight channel with constant width and sharp inlet.

In the first experiment the length of the basin was set equal to 4.6 m and the length of the flume was constrained by the length of the platform to attain the value of 24.14 m (Fig. 3.3). While the width of the basin was set at its maximum possible value, constrained by the width of the platform (2.23 m), the width of the channel was chosen small enough (0.3 m) to limit the effect of the confinement that the side walls of the 'sea' basin induce on the ebb stream issued from the inlet.

In the first run our original aim was to be able to investigate the equilibrium bed profile in the absence of further large scale features of the bottom configuration, which could alter the picture expected on the basis of theoretical investigations where the presence of bars was ignored. As mentioned in the Introduction, the crucial parameter controlling free bar formation is the aspect ratio β defined as the ratio between half channel width and average flow depth. For the set of values of the relevant parameters corresponding to our experimental conditions, the theory of *Seminara and Tubino* [2001] suggests that the critical value of β ranges about few units. Hence, we could not avoid bar formation for depths greater than few centimetres and indeed bars were observed in the first experiment. Moreover smaller scale forms (ripples) formed on the top of bars.

The initially constant value of the mean flow depth D_0^* as well as the amplitude a_0^* and the period T of the forcing harmonic oscillation in the basin were chosen on the basis of preliminary numerical experiments performed using the models for the hydrodynamics and sediment transport discussed in the previous chapter. The aim was to generate a flow field able to mobilize sediments both as bedload and as suspended load throughout a large part of

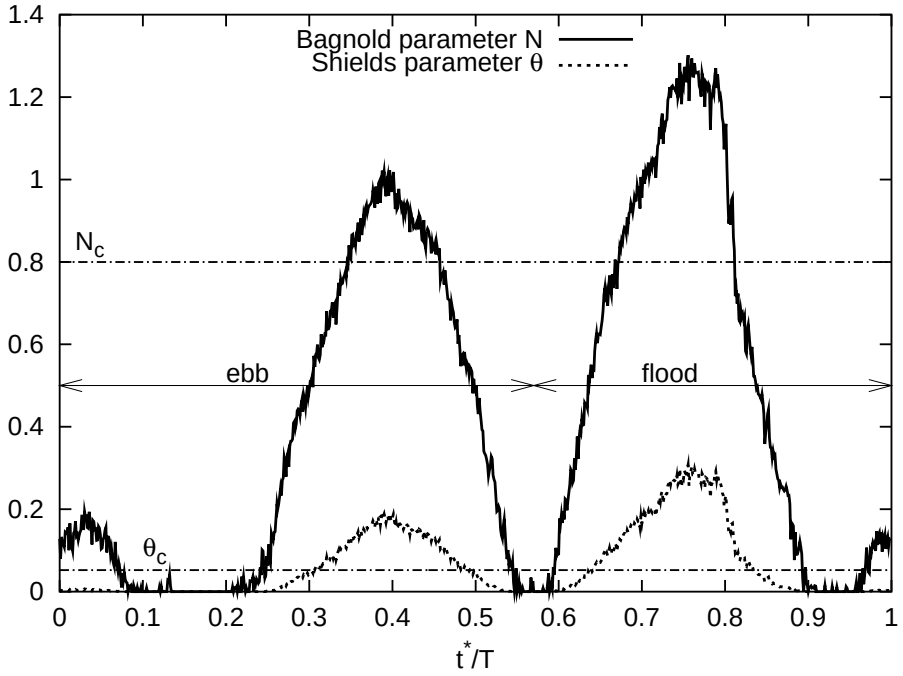

Figure 3.4: Initial temporal distributions of the Shields parameter ϑ and of the Bagnold parameter $N(= u_*/W_s)$ at the inlet. Also shown are the critical values of the former parameter (denoting incipient bedload transport) and of the latter parameter (denoting incipient transport in suspension).

the tidal cycle.

Such preliminary numerical experiments led to the following final choice of the above parameters:

$$D_0^* = 0.082 \text{ m} ; \qquad a_0^* = 0.024 \text{ m} ; \qquad T = 180 \text{ s} . \tag{3.17}$$

The initial temporal distribution of the average flow speed at the inlet under the latter conditions gives rise to distributions of the Shields stress ϑ and of the Bagnold parameter $N(= u_*/W_s)$ such that the stream is able to mobilize sediments throughout most of the tidal cycle (Fig. 3.4). The shape of the inlet was sharp, with the walls of the channel joining the basin walls at 90°. As a result, flood currents led to flow separation close to the entrance and the strong flow acceleration induced by streamline convergence gave rise to deep scour holes at the inlet. The height of the channel walls in the first experiment (0.30 m) was not large enough to allow for the use of a sufficiently thick sediment layer such to prevent the scour hole from reaching the underlying platform. Such undesired feature was then present but was removed in the second experiment.

During the experiments the water surface elevation was continuously monitored in five cross sections along the channel by means of ultrasound probes. A whirl probe was used to measure the local velocity in the absence of sediments during the preliminary experiments, while the surface velocity field of the basin has been estimated using a particle tracking technique.

The bottom evolution at a fixed location of the channel axis of a cross section 12 m far from the inlet was monitored in time for about 4 hours using a profile indicator. The aim was to detect the passage of small scale bedforms. Moreover, bottom topography of both the channel and the basin, was scanned at different times by means of a laser system. Scanning was performed on a sequence of cross sections distant 5 cm from one another along the channel. At each cross section measurements of bottom elevation were performed every 0.5 cm. The mean longitudinal channel profile was obtained calculating the average bottom elevation by averaging the data referring to each cross section. Since the analysis of small scale bedforms required more accuracy, at each stage of the experiment a more detailed longitudinal survey of bottom elevation was also performed taking 5 measurements at each cross section, with 1 cm distance between adjacent cross sections.

3.3.2 Experiment 2: straight landward convergent channel with smooth inlet.

In the second experiment the length of the basin was increased to 6.6 m: this variation was aimed at insuring that the ebb jet would dissipate before reaching the end of the basin. The width of the basin was kept unaltered. Though a wider basin would have been needed in order to prevent any significant interaction between the large scale ebb vortices generated in the basin and the confining walls, however, as discussed below, results of the second experiment appear to be weakly affected by the effect of confinement of the ebb jet. The length of the flume was reduced to the value of 21.4 m. The width of the channel was chosen such to satisfy the exponential law (2.1), with a value of the width at the entrance equal to 0.4 m and a convergence length L_b equal to 30.8 m (Fig. 3.5). The initially constant value of the mean flow depth D_0^* as well as the amplitude a_0^* and the period T of the forcing harmonic oscillation in the basin were again chosen on the basis of preliminary numerical experiments with the following final choice:

$$D_0^* = 0.09 \text{ m} ; \qquad a_0^* = 0.36 \cdot D_0^* = 0.032 \text{ m} ; \qquad T = 120 \text{ s} . \tag{3.18}$$

As a result, the initial value of the aspect ratio of the channel was close to its critical value for bar formation. As discussed below, bars were again observed

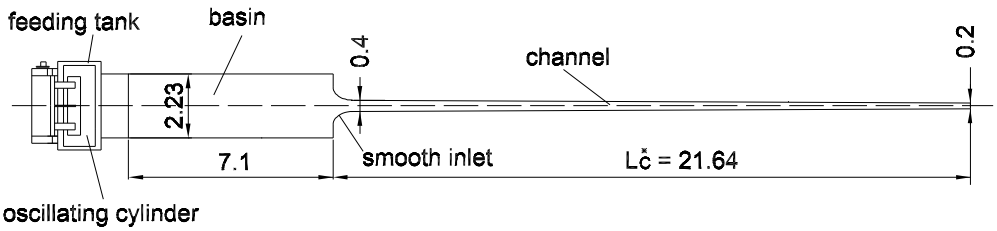

Figure 3.5: Sketch of the apparatus in the second experiment.

Figure 3.6: The smooth shape of the inlet walls in the second experiment.

in the channel at some stage, though the fairly low values attained by the aspect ratio of the channel prevented them from attaining large amplitudes. The height of the channel walls was increased to 0.4 m allowing for a thicker layer of sediments (0.2 m) such that the scour holes at the inlet were no longer able to reach the platform. Furthermore, the shape of the inlet was modified by smoothing out the junctions between the walls of the channel and the basin walls (Fig. 3.6). As a result, the streamline divergence of ebb currents led to sediment deposition in the basin with the formation of an elongated central bar, a delta - like pattern somehow distinct from the pattern observed in the previous experiment.

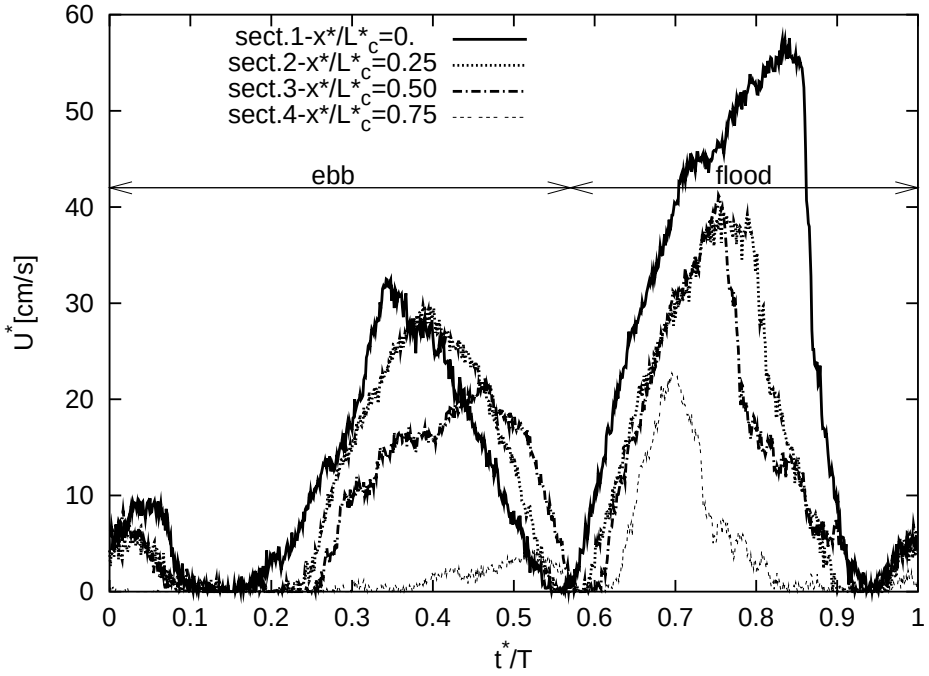

Figure 3.7: The temporal distribution of the cross sectionally averaged speed measured at the initial stage of the morphodynamic evolution is shown at different cross sections and displays the flood dominant character of tide propagation.

3.4 Results of the first experiment.

We now outline some significant observations on the morphodynamic evolution observed both in the channel and in the basin.

3.4.1 Evolution of the bed profile.

The major fact observed in the experiment is that sediments were scoured in the seaward portion of the channel, driven landward and deposited in the inner part of the channel. This mechanism is associated with the flood dominant character of the flow field in the initial stage of the morphodynamic evolution process. In fact, Fig. 3.7 shows that the temporal distribution of the cross sectionally averaged flow speed is increasingly asymmetric proceeding from the inlet landward, with the ebb phase longer than the flood phase and the flood maximum invariably larger than the ebb maximum. As a result, a fairly sharp front forms in the bed profile and migrates landward. Once the front reaches the inner end of the channel, the formation of a dry and wet region starts and leads eventually to the development of a 'beach'. The

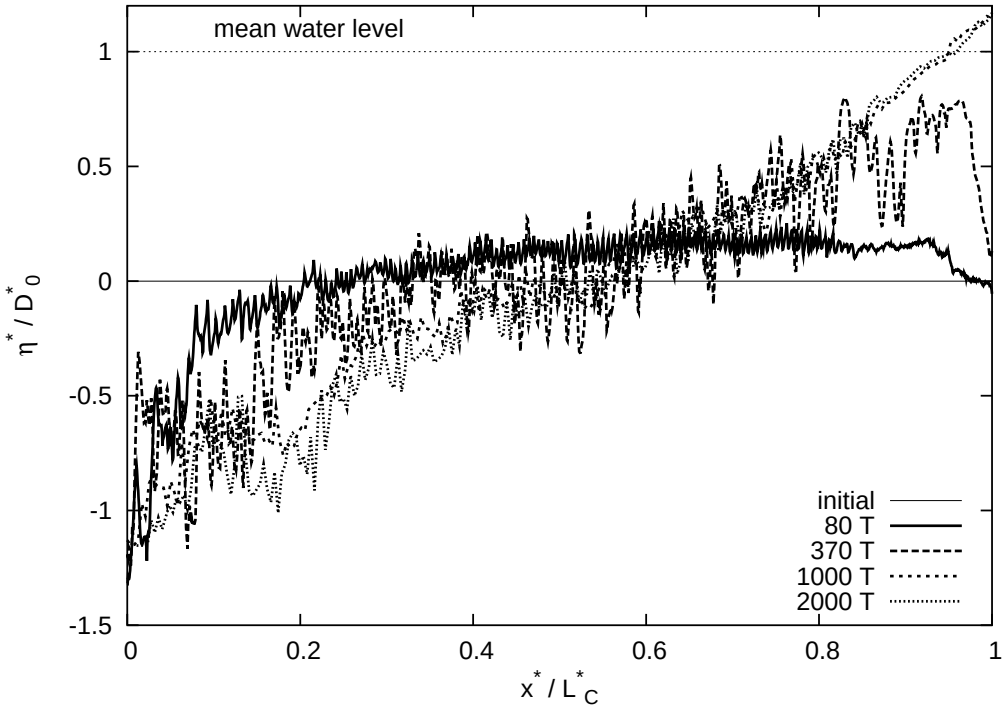

Figure 3.8: Temporal evolution of the cross sectionally averaged bed profile in the first experiment.

temporal evolution of the cross sectionally averaged bed profile is plotted in Fig. (3.8). The experiment lasted about 100 h corresponding roughly to 2000 tidal cycles, i.e about 3 years in the prototype. Comparison between the bed profiles at 1000 and 2000 cycles shows that the pattern reached at the end of the experiment was likely not far from equilibrium (Fig. 3.9). However, the reader should note that, approaching equilibrium, the net sediment flux in a tidal cycle, which controls bed evolution, progressively decreases, hence the evolution process increasingly slows down. In other words, further improving the degree of closeness of the bed profile to equilibrium would require prohibitively large times even in the laboratory. In fact, though weak, bedload transport was still present at the final stage of the experiment, as evidenced by the migration of ripples.

The formation of the beach was fairly rapid, as a region emerging at low water was already present after 400 cycles.

Finally, note that the 'equilibrium' bottom profile was slightly concave seaward and slightly convex landward, consistently with field observations concerning tidal channels and with the theoretical findings [*Lanzoni and Sem-*

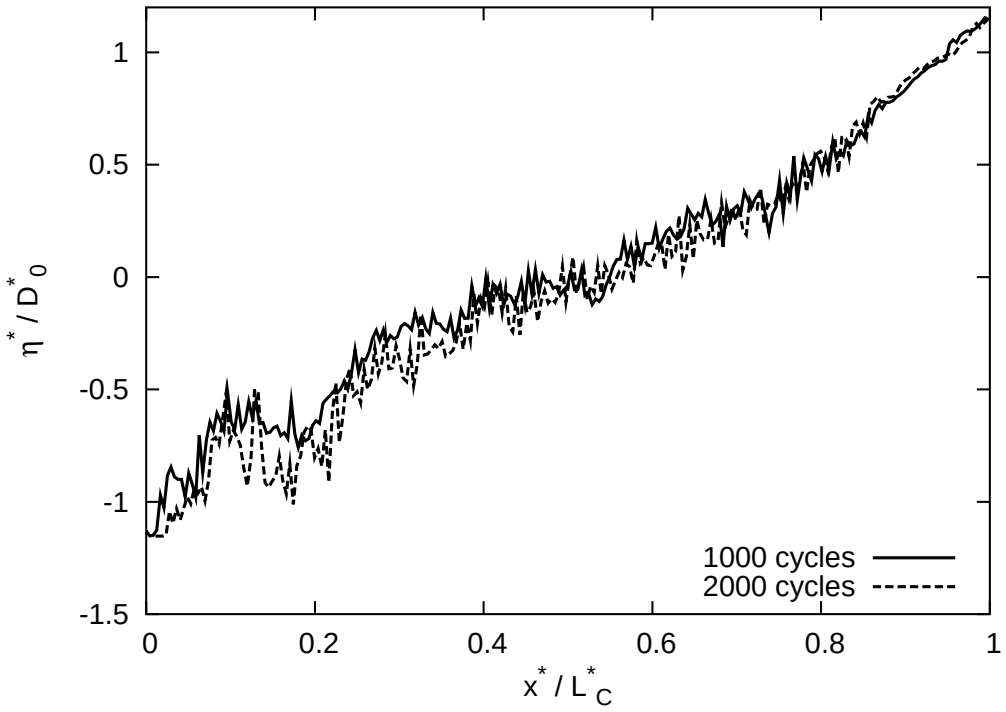

Figure 3.9: Comparison between the bed profiles at 1000 and 2000 cycles.

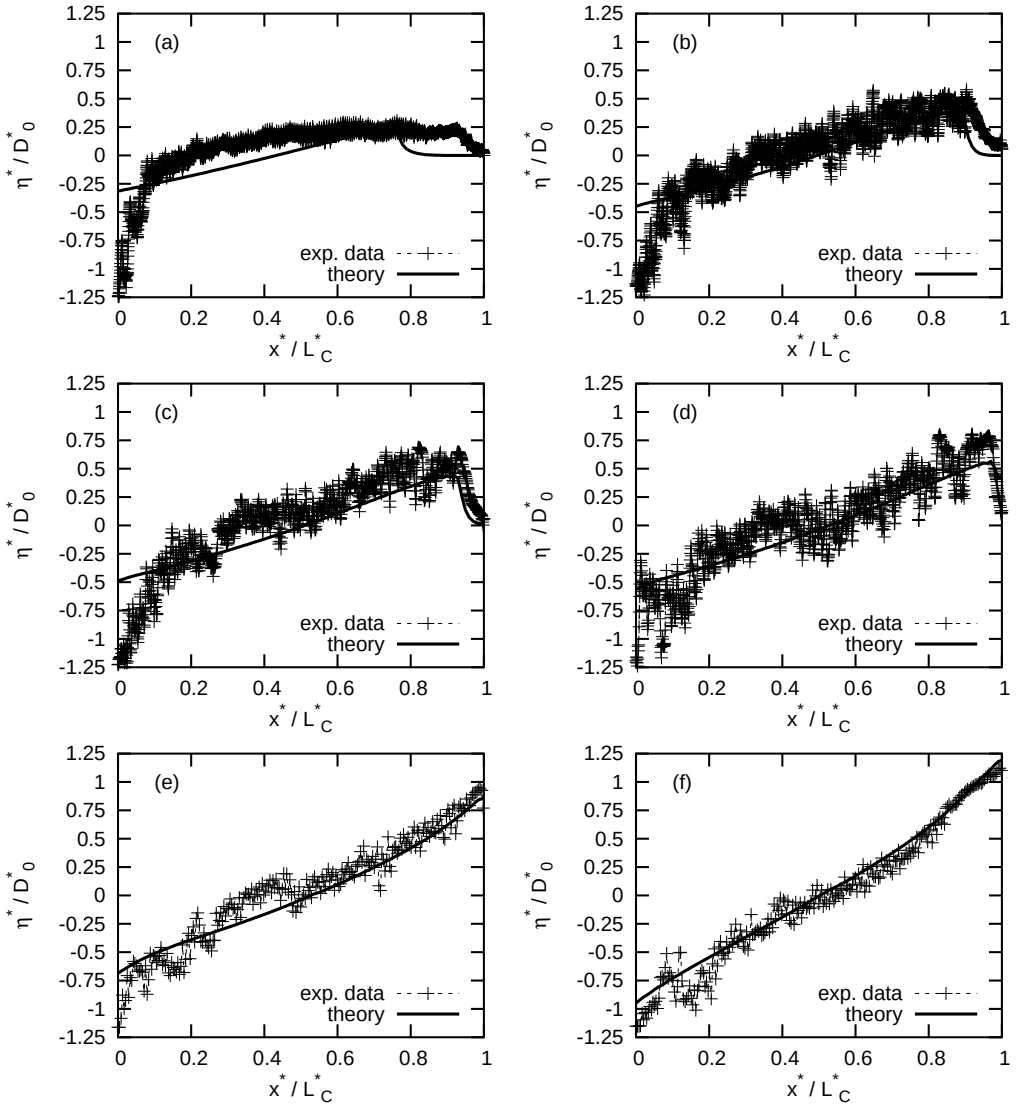

Figure 3.10: Comparison between the cross sectionally averaged bed profiles observed in experiment 1 at different times and those calculated by the approach developed in Chapter 2. (a) $t^* = 80\,T$, (b) $t^* = 200\,T$, (c) $t^* = 250\,T$, (d) $t^* = 370\ T$, (e) $t^* = 570\ T$, (f) $t^* = 2000\ T$.

inara, 2002; *Bolla Pittaluga*, 2003; Chapter 2].

Figure 3.10 shows a detailed comparison between the observed bed profiles and the profiles calculated by the approach developed in Chapter 2 at different times. Various observations arise from such a comparison:

- though the general trend of the evolution process seems adequately

reproduced in the physical model, however the observed bed profile tends to equilibrium faster than the calculated one: such discrepancy arises from the presence (see Fig. 3.11 and the discussion below) of a net exchange of sediments between the channel and the basin. The latter was driven by the inlet hydrodynamics and cannot be described in the context of a 1D model;

- the above discrepancy tends to be reduced in the course of the experiment; this is reflected in the fact that the equilibrium configuration predicted theoretically is quite close to the experimental observations, except close to the channel inlet where the 1D model is obviously unable to reproduce the effect of streamline convergence occurring in the flood phase which leads to pronounced localized scour: such discrepancy has been sharply reduced in the second experiment where the shape of the inlet has been smoothed out;

- the noise superimposed on the average bed profile is due to the presence of small scale forms (ripples, as discussed below) which formed during the early stage of the experiment and persisted throughout;

- in the first experiment, large scale forms, i.e. bars were also observed.

The temporal evolution of the net exchange of sediments between the channel and the adjacent basin is shown in Fig. 3.11. Note that the net exchange is invariably positive (from the basin into the channel). In particular, Fig. 3.11, where the ratio between the net volume of sediments exchanged and the maximum between the volume of sediments associated with landward aggradation in the channel and seaward scouring in the channel is plotted at different times, suggests that the observed bed evolution was only partly the result of a rearrangement of the sediments stored in the channel bed, which degraded seaward and aggraded landward: part of the evolution was driven by the net exchange of sediments between the channel and the basin. However, the final equilibrium was only slightly affected by such exchange (roughly 10 % of the total aggradation originates from the net exchange of sediments with the adjacent basin). Note also that the observed net exchange of sediments between the channel and the adjacent basin in the experiment differs significantly from the one calculated by means of the theoretical model in the initial stage of the experiment to attain a similar value at the end of the experiment (Figure 3.12).

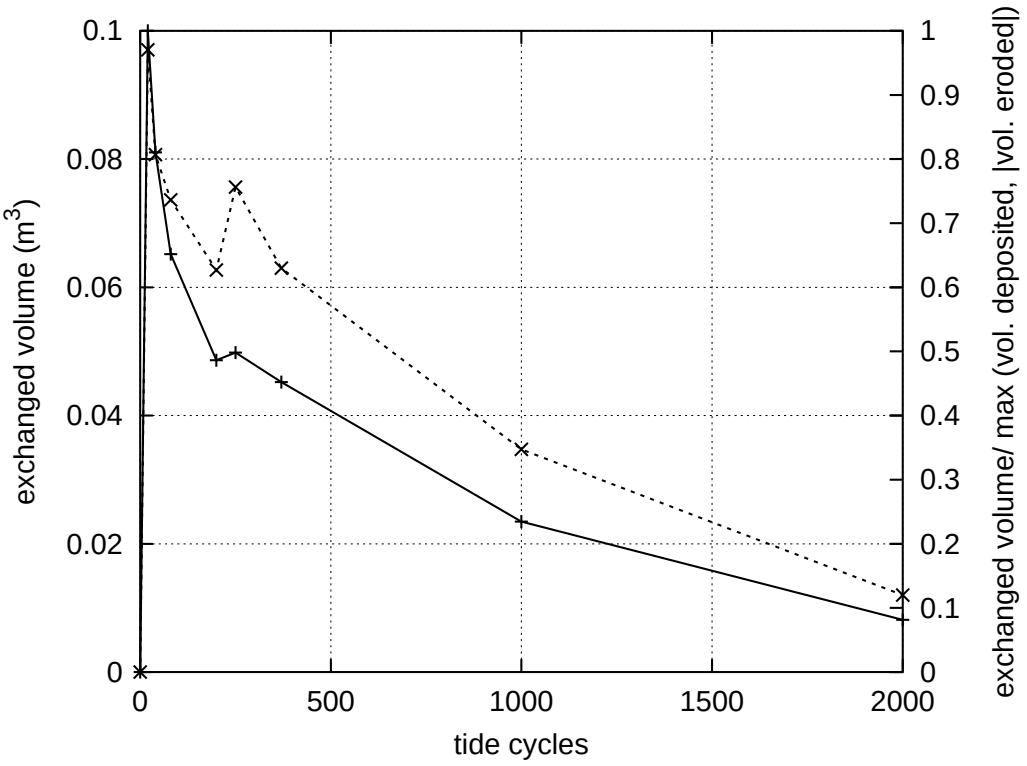

Figure 3.11: The volume of sediments exchanged by the channel with the 'sea' basin (dotted line) and the ratio between the exchanged volume and the maximum between the volume of sediments deposited in the inner part of the channel and the volume of sediments eroded in the seaward part of the channel (continuos line), is plotted at different times.

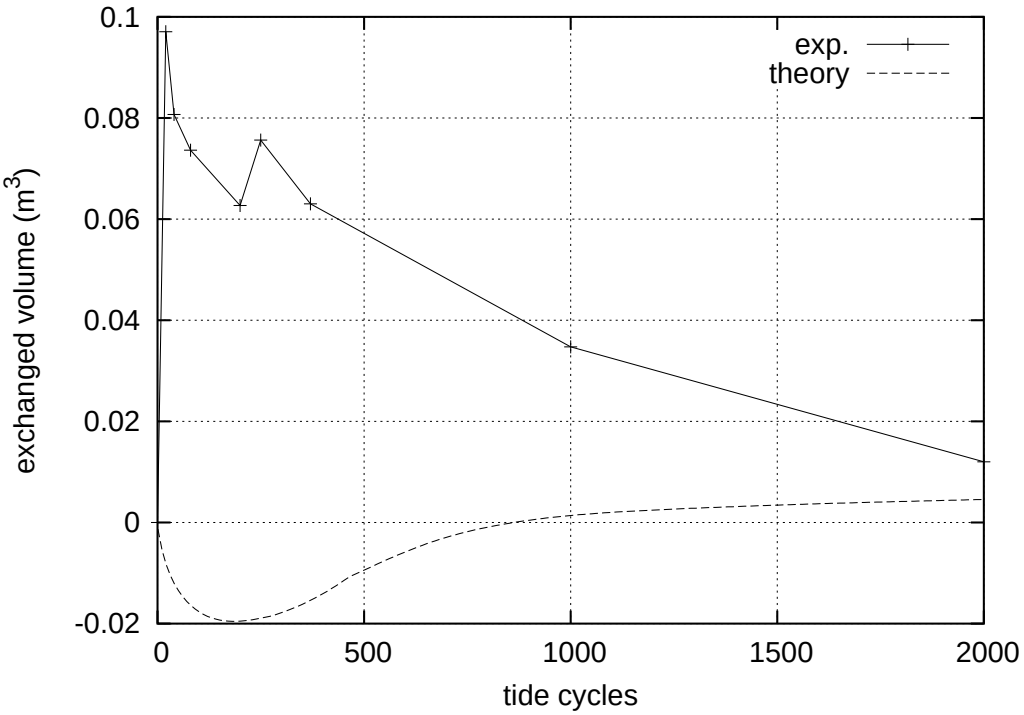

Figure 3.12: The observed volume of sediments exchanged by the channel with the 'sea' basin in the experiment 1 is compared with that calculated by means of the theoretical model at different times.

3.4.2 Morphodynamic evolution of the inlet region.

We know from the early work of *Blondeaux et al.* [1982], referring to the fixed bed case, that at the initial stage, when the bed is flat everywhere, the flow field in the 'sea' region around the channel inlet is highly asymmetric throughout the tidal cycle. In fact, during the flood phase, the channel effectively acts as an unsteady sink which gives rise to a nearly irrotational 2D flow pattern; on the contrary, during the ebb phase, vorticity is continuously shed from the separation points at the sharp edges of the inlet and gives rise to an unsteady turbulent jet characterized by the formation of a large scale recirculating cell consisting of a pair of counterrotating vortices which leaves the generation area under the effect of the induced velocity that each vortex determines on the other. The formation of this cell emerges clearly in the satellite pictures of the flow issuing from the inlets of Venice lagoon (Fig. 3.13). *Blondeaux et al.* [1982] modelled such a complex flow field as 2D irrotational in the flood phase and as inviscid rotational during the ebb phase. Moreover, using vortex shedding techniques, they were able to reproduce successfully the formation of the recirculating cell, which was also observed in fixed bed experiments performed at the Laboratory of DIAM (formerly, the Hydraulic Institute) of the University of Genova. In Fig. 3.14 the surface velocity measured in the basin at different times of the initial phase of the present experiment using the particle tracking techique is shown and displays the asymmetry just mentioned. *Blondeaux et al.* [1982] argued that such asymmetry, along with the role of littoral currents, is responsible for a continuous renewal of the water stored in the lagoon as most of the water entering the lagoon during the flood phase differs from the water that had just left the lagoon in the previous ebb phase.

In the present context our interest is concentrated on the exchange of sediments and on the mobile character of the bed. The latter has a profound effect both on the inlet hydrodynamics and morphodynamics. In fact, the strong seaward current that the counterrotating vortices generate close to the channel axis leads to an intense scour of the bed and to the generation of a submerged channel which progresses seaward until it reaches a quasi - equilibrium conditions. Simultaneously, the sediments entrained by the scouring action of the vortices deposit laterally, giving rise to the formation of sort of submerged levees confining the submerged channel. This is shown in Figures 3.15a, b where the bed elevation measured at two different cross sections of the sea basin, located at increasing distances from the inlet, is reported. Note that the bed evolution displays a somewhat oscillating and fairly unstable character: this feature arises from the complex interaction between the large scale coherent structures generated by the shear layer issued

Figure 3.13: A Landsat picture of the jets issuing from the inlets of Venice lagoon, displaying the formation of the recirculating cell shed from the inlet edges predicted by *Blondeaux et al.* [1982].

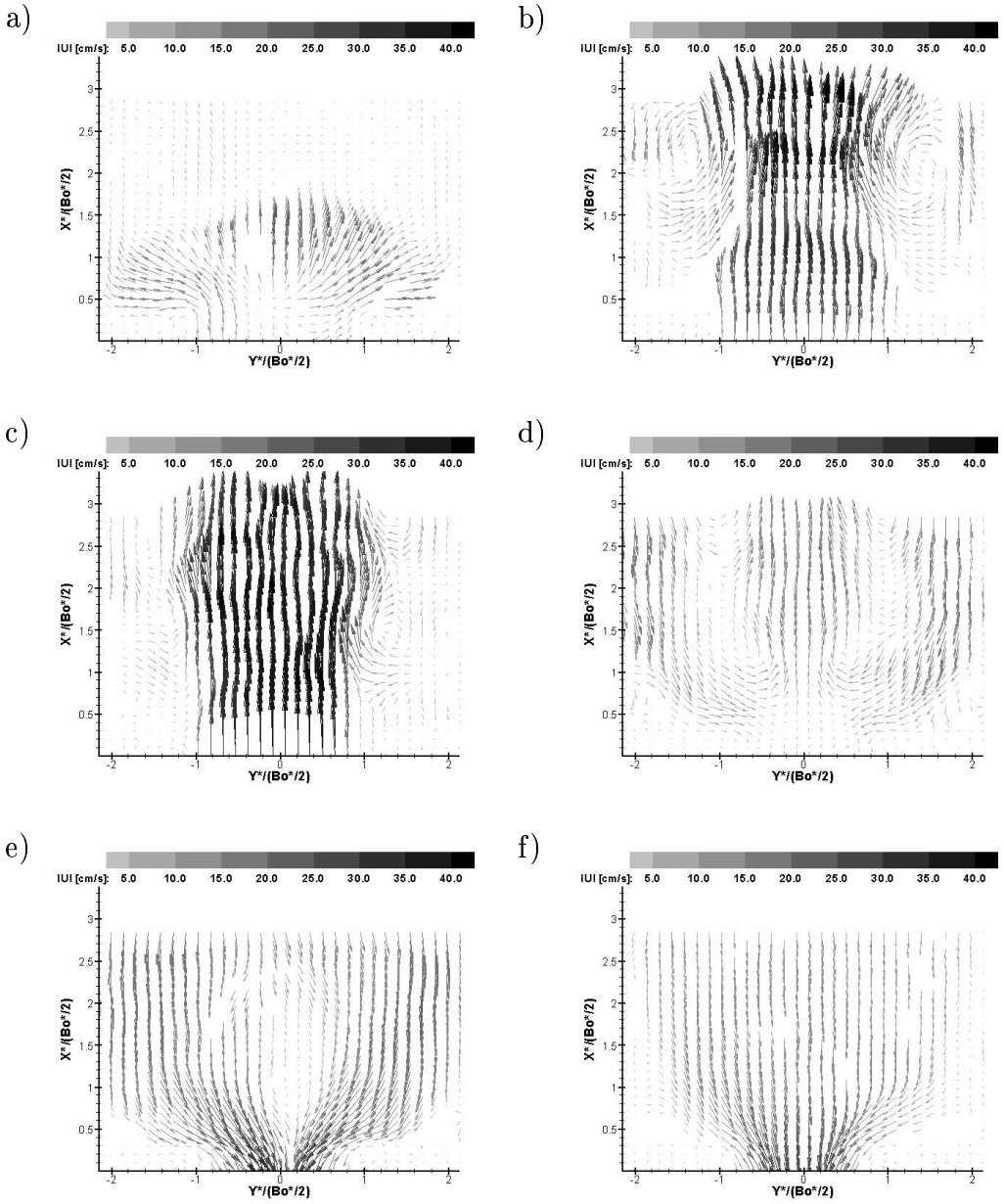

Figure 3.14: Surface velocity measured in the basin in the initial stage of experiment 1, when the bed was still flat, showing the asymmetry between the ebb and the flood flow fields. $t^*/T = m/6$ (a) $m = 0$; (b) $m = 1$; (c) $m = 2$; (d) $m = 3$; (e) $m = 4$; (f) $m = 5$;

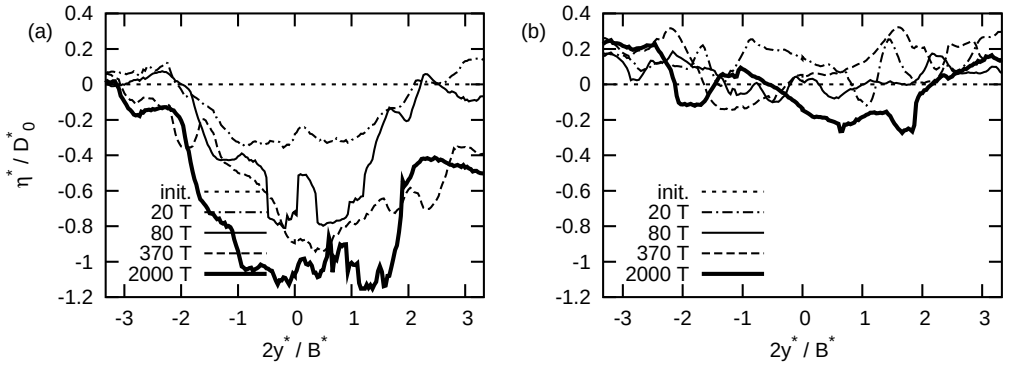

Figure 3.15: Evolution of the bed elevation measured at two different cross sections of the sea basin, located at increasing distances from the inlet. (a) $2x^*/B^* = -1$, (b) $2x^*/B^* = -3$.

from the sharp edges of the inlet and the mobile bed. This is clarified by the sequence of topography fields measured at different times in the basin using the laser scanner device described in sect. 3.3 (Fig. 3.16 a,b,c). An important feedback of the morphodynamic evolution of the inlet region is a significant reduction of the ebb - flood flow asymmetry: in fact, the formation of the submerged channel acts in the flood phase such to keep the current more aligned with the channel axis. This is shown in Fig. 3.17, where the surface velocity in the basin measured during the flood phase at an advanced stage of the morphodynamic evolution is compared with the corresponding pattern detected at the initial stage.

3.4.3 The pattern of bedforms.

Immediately after the start of the experiment ripples were observed to form throughout the whole length of the channel (Fig. 3.18). The fact mentioned in sect. 3.1 that such forms are to be interpreted as fluvial type ripples rather than dunes requires to be substantiated. The formation criterion for fluvial ripples can be written in the form [*Sumer and Bakioglu*, 1984]:

$$\frac{k_s u_*}{\nu} < 57.5 \tag{3.19}$$

where k_s is the absolute bed roughness, which can be estimated as $(2.5\ d^*_{50})$ (Figure 3.19). At incipient sediment transport, when ripples form, the friction velocity of experiment 1 can be estimated to range about $2{\cdot}10^{-3}\ m/s$, hence the parameter $(k_s u_*)\,/\nu$ ranges about 1.5, well within the range of the formation criterion (3.19). The most unstable wavelength L_r predicted by

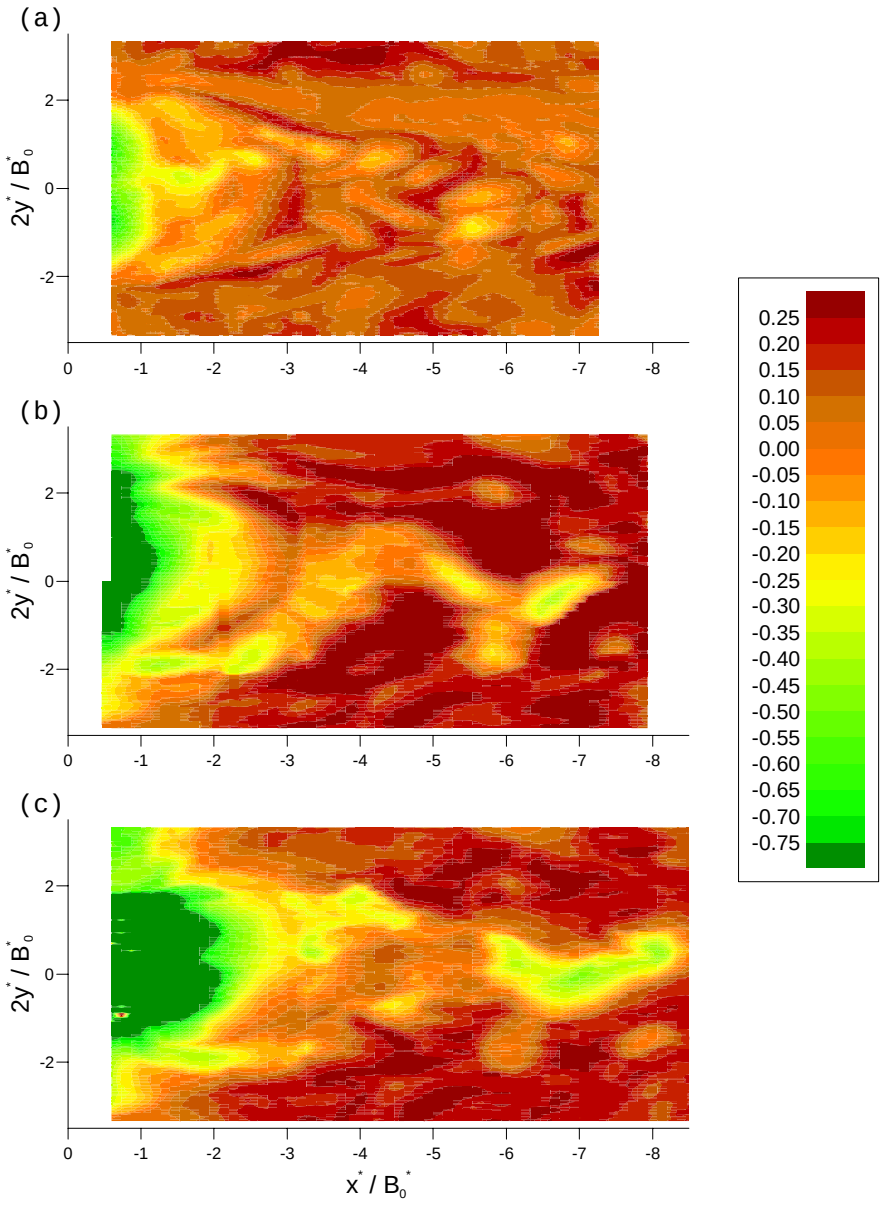

Figure 3.16: Topography fields measured at different times in the inlet region using the laser scanner device. They show localized patches of scour and deposition driven by the interaction between the large scale coherent structures generated by the instability of the shear layers shed by the inlet edges and the mobile bed. Bottom elevation is made dimensionless with the initial flow depth. (a) $t^* = 20\ T$, (b) $t^* = 370\ T$, (c) $t^* = 2000\ T$.

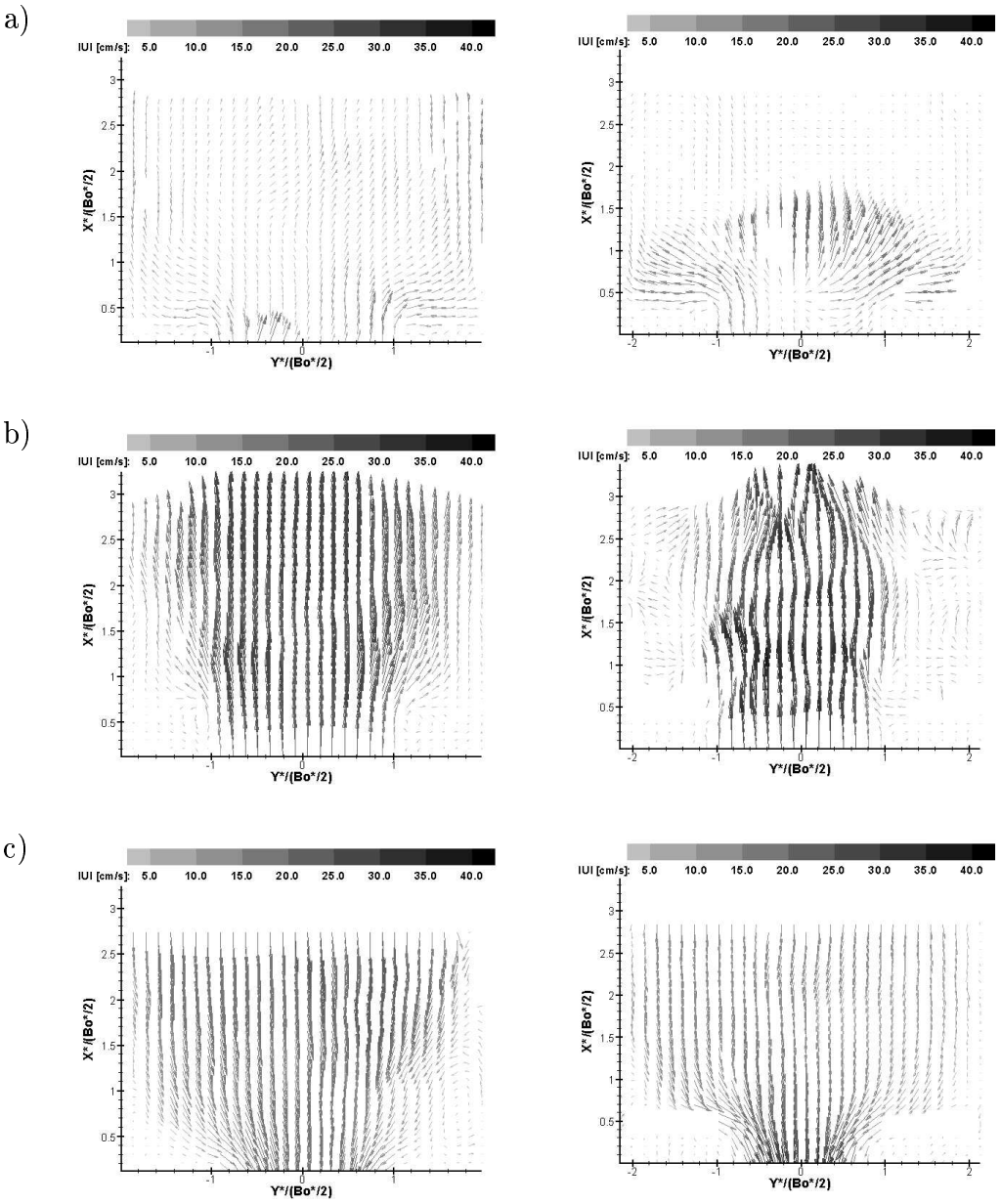

Figure 3.17: The surface velocity measured in the inlet region at an advanced stage ($t^* = 26\ T$) during the flood phase (left) is compared with the corresponding pattern detected at the initial stage ($t^* = 0\ T$) (right) showing the feedback of morphodynamics on inlet hydrodynamics. $t^*/T = m/4$ (a) $m = 0$; (b) $m = 1$; (c) $m = 3$.

Figure 3.18: A picture of the ripple pattern observed along the channel in the initial phase of experiment 1.

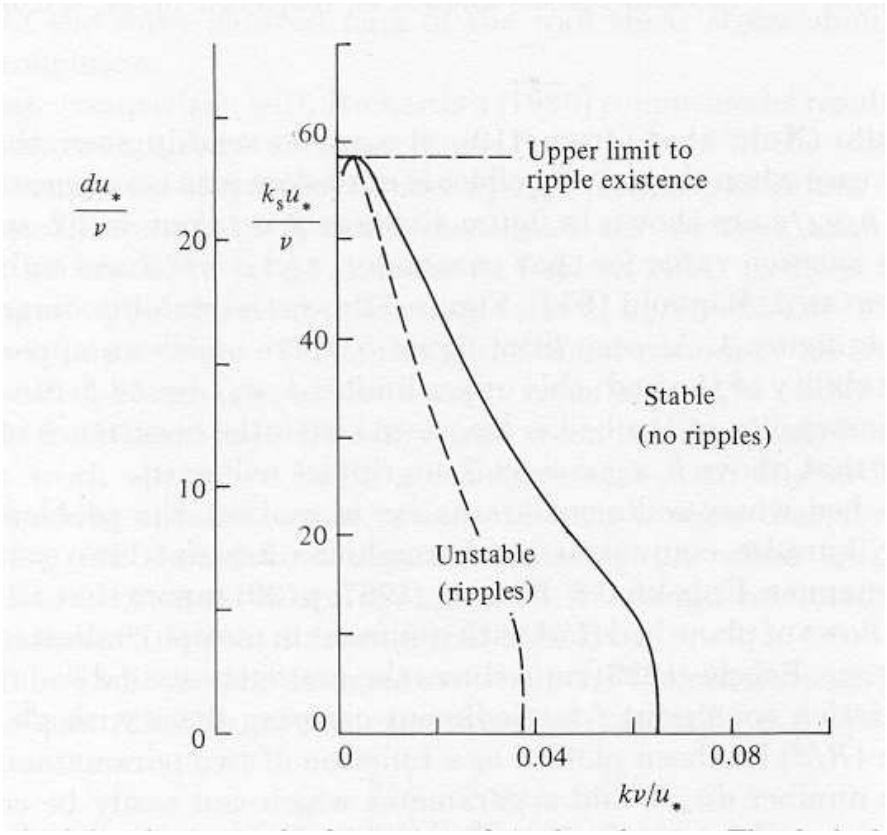

Figure 3.19: Marginal stability curve for fluvial ripples ($k_s = 2.5\ d_{50}^*$, $k = 2\pi/L_r$). The dashed curve corresponds to the fastest growing wavenumber. [*Sumer and Bakioglu*, 1984]

Sumer and Bakioglu [1984] is known to underestimate the wavelength of fluvial ripples experimentally observed. With the present values of the relevant parameters the theoretical value of L_r is equal to 170 ν/u_*, and ranges about 8 cm, while the value experimentally observed falls in the range (15 - 20 cm). The amplitude of ripples observed in the experiment attained values ranging about 1 cm. Ripple amplitude as well as ripple wavelength exhibited some fluctuations along the channel, but did not show any correlation with flow depth, as one would expect if such bedforms were interpreted as dunes. This will be better demonstrated in the discussion of results of experiment 2 (Fig. 3.32).

Ripples displayed initially a quasi 2D pattern (Fig. 3.18). Moreover, they seemed to respond to variations of the hydrodynamic conditions and of sediment transport. In particular, the damping effect of suspended load on ripple development was clearly detected, since during the flood phase ripples were washed out to form again during the ebb phase which was characterised by lower values of suspended load. Such a behaviour deserves some explanation. In fact, it suggests that, under the experimental conditions, the time scale of ripple growth is much smaller than the tidal period. In other words, ripples adjust, with some delay, to the instantaneous hydrodynamic conditions: in these terms they may be described as having a 'fluvial', rather than 'coastal' nature.

As the experiment proceeded and equilibrium was approached, the intensity of sediment transport decreased: as a result, ripples persisted throughout the tidal cycle. This allowed to follow ripple development in detail and ascertain that ripples migrated landward during the flood phase and seaward during the ebb phase. However, the former prevailed on the latter, hence a net landward migration was detected, a feature readily explained as a consequence of the flood dominant character of tide propagation. Fig. 3.20, which shows the temporal development of bed elevation in the middle of a cross section located at a distance of 12 m from the channel inlet, displays the passage of four ripples characterized by a net migration speed ranging about 20 m/h.

The quasi 2D ripple pattern was replaced by complex 3D patterns in the landward portion of the channel after the first hours of experiment (Fig. 3.21).

Bars.

Figure 3.22 shows the pattern of bed topography in the seaward half of the channel at different times, showing the presence of alternate bars. Notice that in this and in the following plots the cross sectionally averaged bed

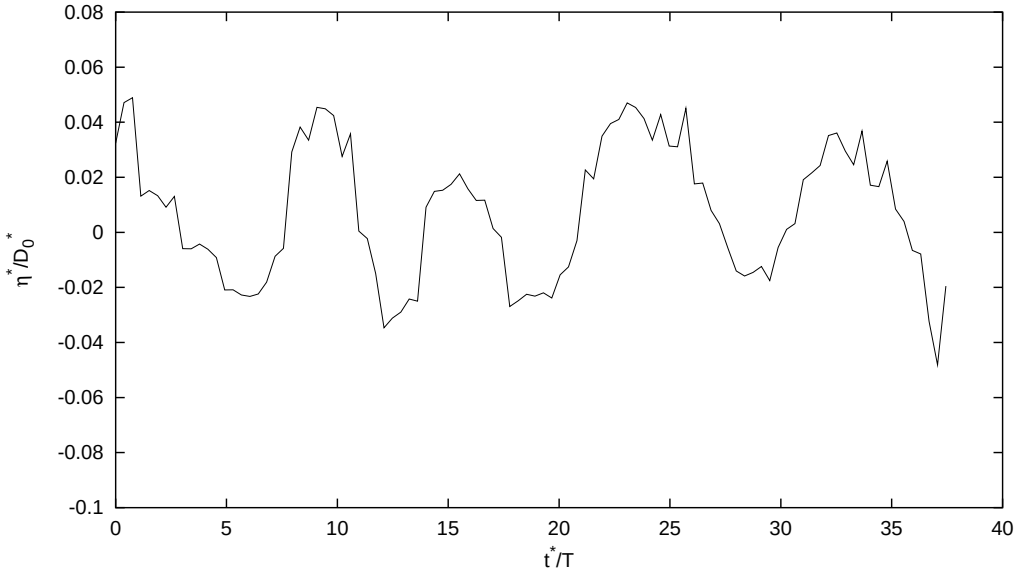

Figure 3.20: Temporal development of bed elevation at a cross section located at a distance of 12 m from the channel inlet showing the passage of four ripples migrating landward.

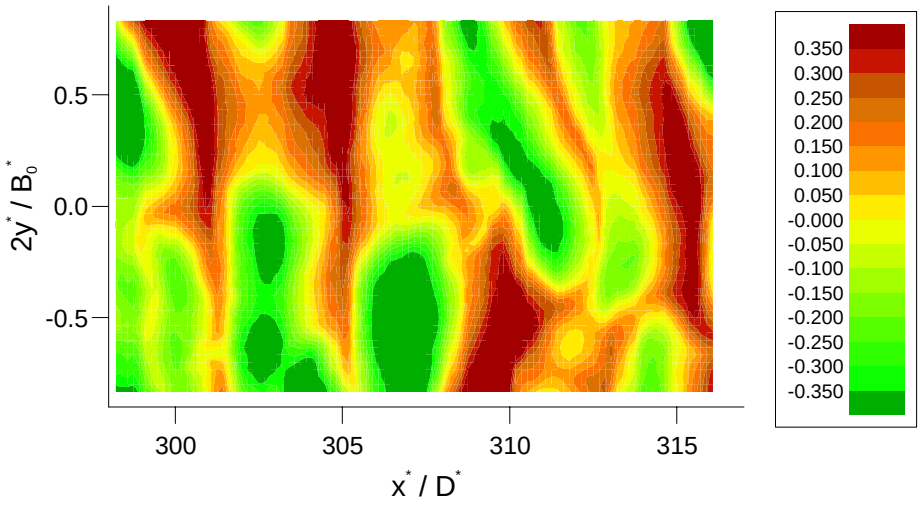

Figure 3.21: 3D ripples pattern in the landward portion of the channel after the first hours of experiment.

profile has been filtered out. A similar plot referring to the landward half of the channel is given in figure 3.23, while a more detailed picture of the bed pattern referring to the seaward portion of the channel close to the inlet is given in Figure 3.24.

A comparison between the bar features observed in the experiment and theoretical predictions of *Seminara and Tubino* [2001] are reported in sect. 3.5 in the context of the discussion of results of the second experiment.

3.5 Results of the second experiment.

Many of the features of the morphodynamic evolution observed both in the channel and in the basin in the second experiment were similar to those observed in the first experiment. Some distinct features arose from channel convergence and the smooth shape of the inlet. Let us review the main observations.

3.5.1 Evolution of the bed profile.

The evolution of the bed profile in the second experiment was similar in many respects to those observed in the previous experiments, in particular:

- sediments scoured in the seaward portion of the channel migrated landward forming a sharp front and deposited in the inner part of the channel;
- a 'beach' formed in the inner part of the channel. The temporal evolution of the cross sectionally averaged bed profile is plotted in Fig. 3.25.

Figure 3.26 shows a detailed comparison between the observed and calculated bed profiles at different times displaying the following features:

- again the observed bed profile tends to equilibrium faster than the calculated one as a consequence of a net exchange of sediments between the channel and the basin, driven by the inlet hydrodynamics;
- ripples formed during the early stage of the experiment and persisted throughout;
- large scale forms, i.e. bars, were also observed after about 50 cycles;
- the equilibrium configuration predicted theoretically is quite close to that experimentally observed, once fluctuations associated to small and large scale bedforms are removed.

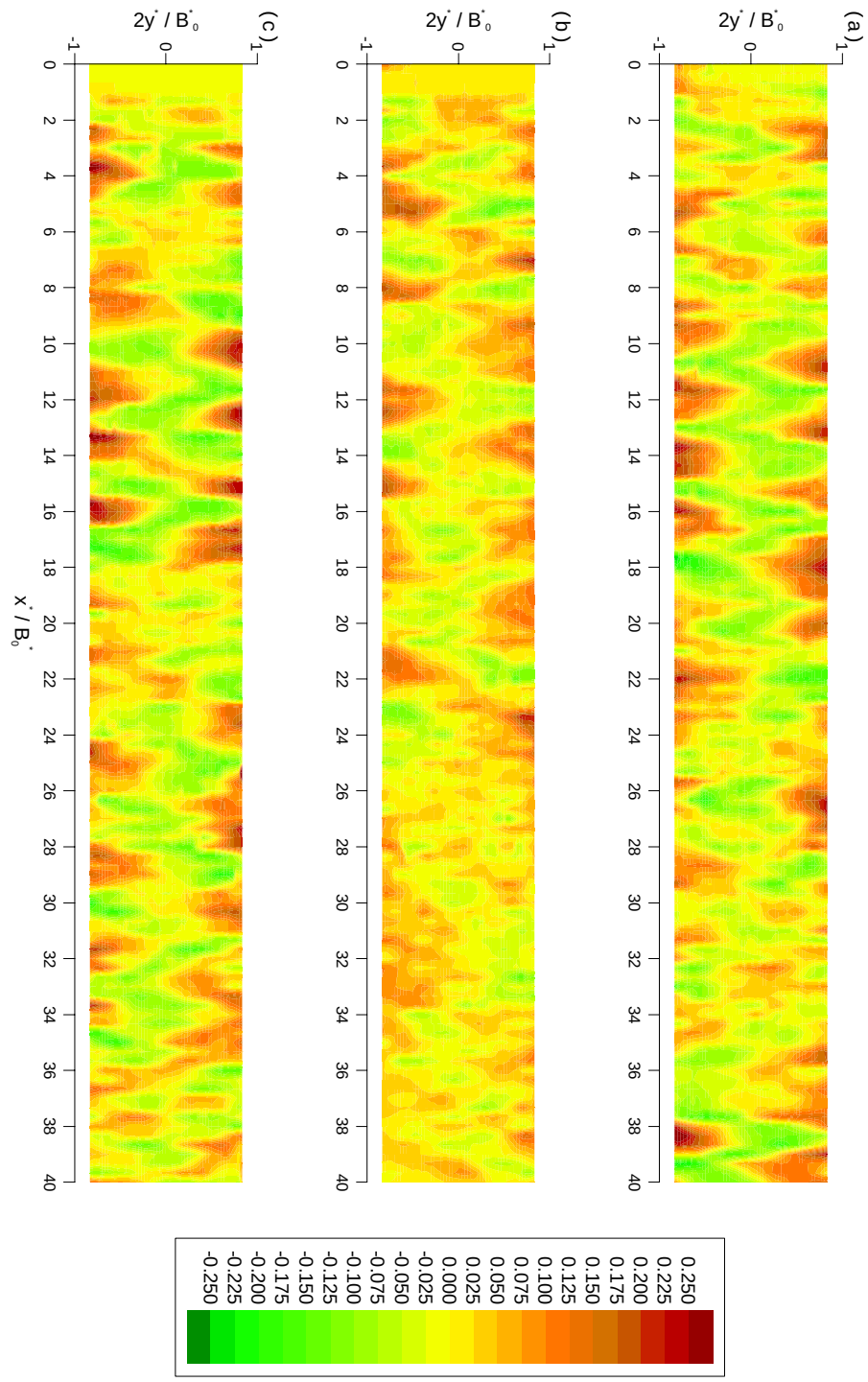

Figure 3.22: The pattern of bed topography in the seaward half of the channel at different times, showing the presence of alternate bars. Note that the cross sectionally averaged bed profile has been filtered out. Bottom elevation is scaled by the local flow depth. (a) $t^* = 570\ T$, (b) $t^* = 1000\ T$, (c) $t^* = 2000\ T$.

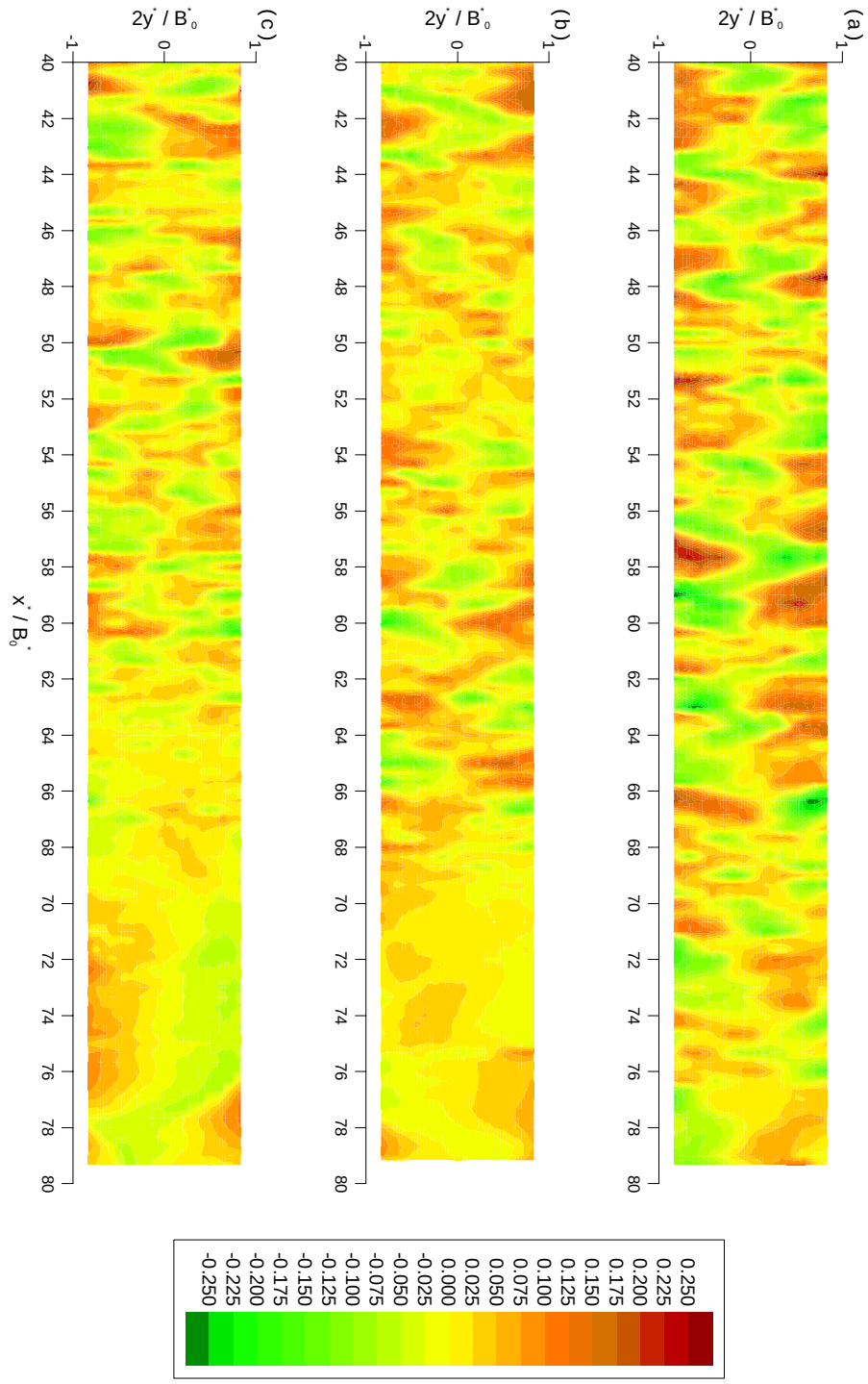

Figure 3.23: The pattern of bed topography in the landward half of the channel at different times. Note that the cross sectionally averaged bed profile has been filtered out. Bottom elevation is scaled by the local flow depth. (a) $t^* = 570\ T$, (b) $t^* = 1000\ T$, (c) $t^* = 2000\ T$.

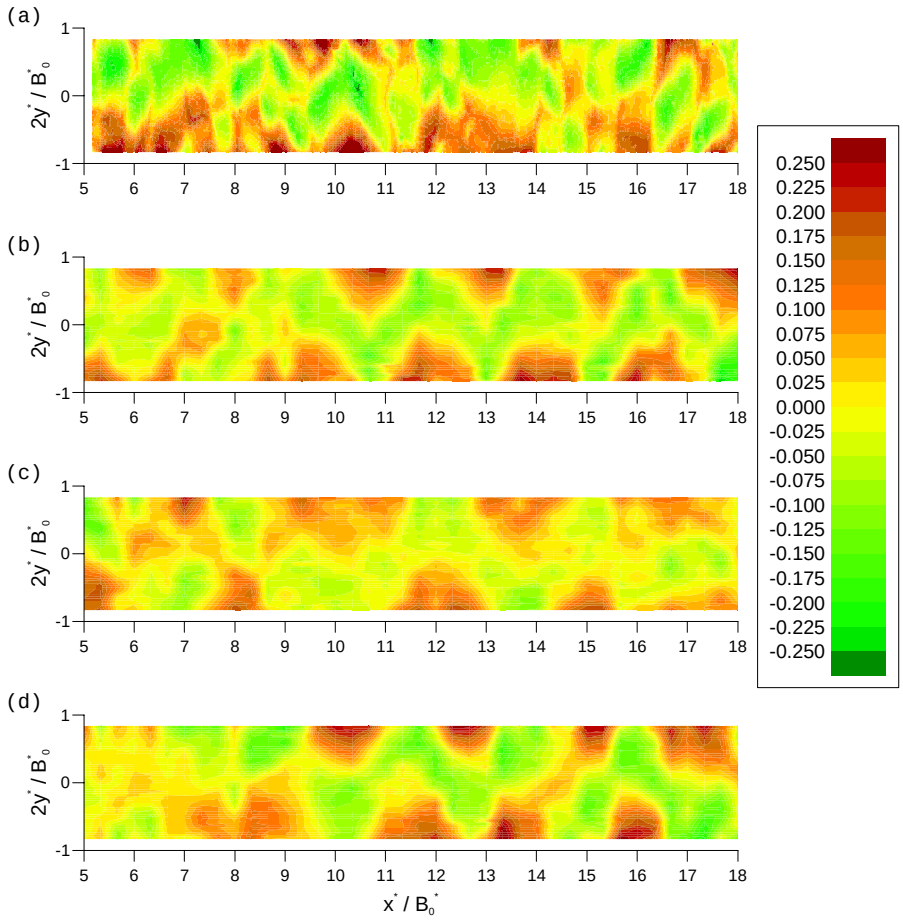

Figure 3.24: The pattern of bed topography in the seaward portion of the channel close to the inlet at different times showing the presence of alternate bars. The cross sectionally averaged bed profile has been filtered out. Bottom elevation is scaled by the local flow depth. (a) $t^* = 200\ T$, (b) $t^* = 570\ T$, (c) $t^* = 1000\ T$, (d) $t^* = 2000\ T$.

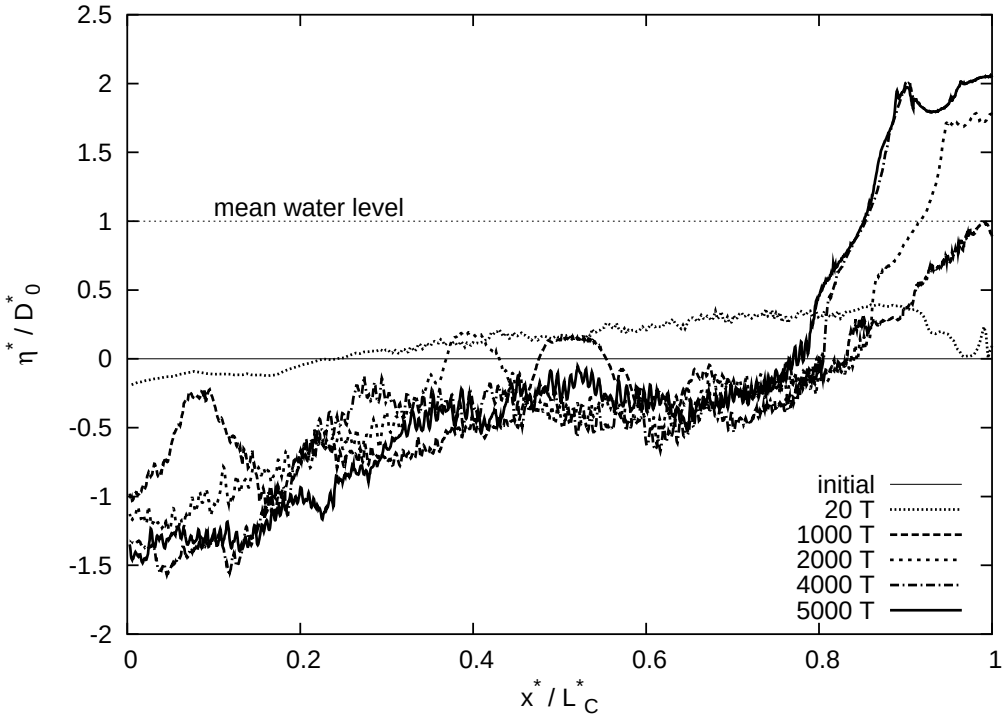

Figure 3.25: Temporal evolution of the cross sectionally averaged bed profile in the second experiment.

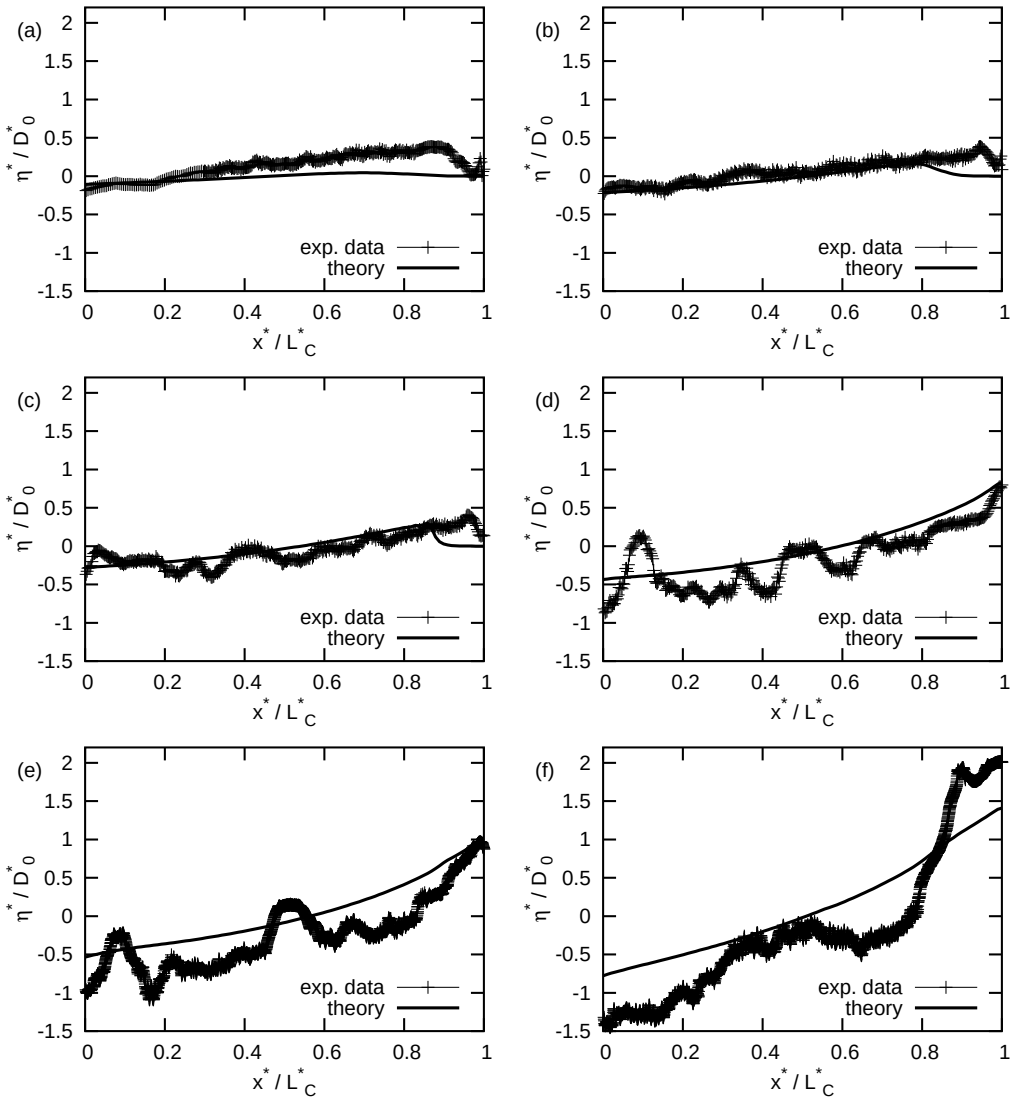

Figure 3.26: Comparison between the cross sectionally averaged bed profiles observed in experiment 2 at different times and those calculated by the approach developed in Chapter 2. (a) $t^* = 20\,T$, (b) $t^* = 60\,T$, (c) $t^* = 100\,T$, (d) $t^* = 500\,T$, (e) $t^* = 1000\,T$, (f) $t^* = 5000\,T$.

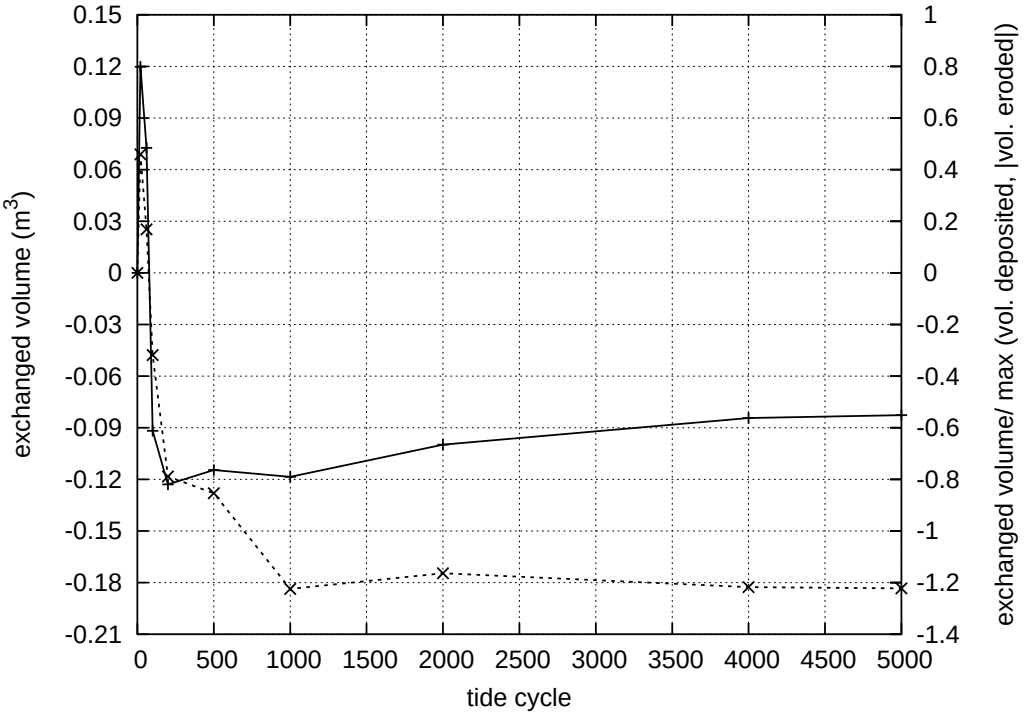

Figure 3.27: The volume of sediments exchanged between the channel and the 'sea' basin (dotted line) is plotted at different times for experiment 2. Also plotted is the ratio between the exchanged volume and the maximum between the volume of sediments deposited in the inner part of the channel and the volume of sediments eroded in the seaward part of the channel (continuous line).

The temporal evolution of the net exchange of sediments between the channel and the adjacent basin is shown in Fig. 3.27. In this case the net exchange is positive (from the basin into the channel) in the very initial stage; later it changes sign to keep negative till the end of the experiment. Unlike the observations performed in the first experiment, the final equilibrium was now significantly affected by such exchange, as 70% of the total degradation of the channel originates from the net exchange of sediments with the adjacent basin. As Figure 3.28 shows, the difference between the theoretical and observed net exchange of sediments kept roughly constant as the experiment progressed.

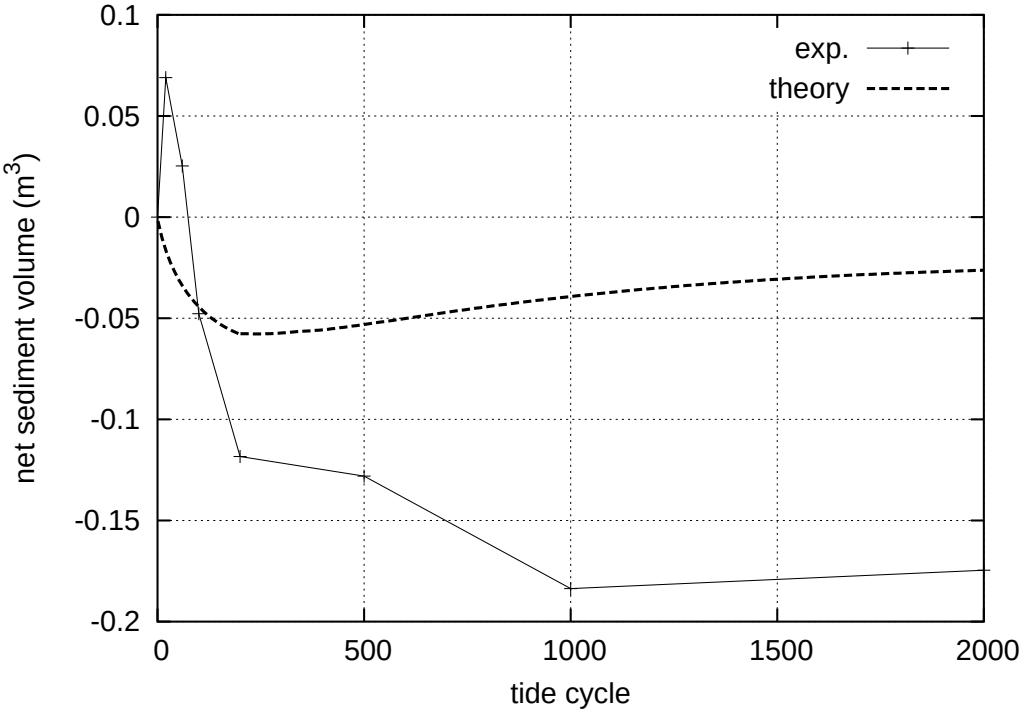

Figure 3.28: The observed volume of sediments exchanged between the channel and the 'sea' basin in experiment 2 is compared with that calculated by means of the theoretical model at different times.

3.5.2 Morphodynamic evolution of the inlet region.

The smooth, diverging shape of the inlet affects the inlet hydrodynamics and morphodynamics significantly. In fact, on one hand a strong seaward current is generated close to the inlet during the ebb phase and leads to intense scour with the formation of a submerged channel which progresses seaward until it reaches an equilibrium condition. However, the diverging character of the streamlines gives rise to sediment deposition in the form of an elongated central bar located seaward and levees bounding the scoured region adjacent to the inlet. This is shown in the Figures 3.29, 3.30 showing the pattern of bed elevation measured at different times in the sea basin using the laser scanner device. The smooth diverging shape of the inlet in experiment 2 caused a further reduction of the ebb - flood flow asymmetry, again enhanced by the morphodynamic evolution of the inlet described above. The change of inlet topography experienced in experiment 2 reflects itself in the different temporal evolution of the net exchange of sediments between the channel and the sea basin, emerging from a comparison between the Figures 3.11 and 3.27.

3.5.3 Ripples.

Immediately after the start of the experiment a quasi 2D ripple pattern was again observed throughout part of the length of the channel (Fig. 3.31). Initially ripples formed everywhere except in the regions immediately close to the inlet and to the landward end of the channel. As the intensity of sediment transport decreased, the presence of ripples extended to most of the channel. Ripple amplitude (ranging about 1.5 cm) as well as ripple wavelength (ranging about 15 - 20 cm) exhibited fluctuations along the channel, as shown in Fig. 3.32a,b where no distinct correlation with flow depth can be detected.

An interesting feature displayed by the ripple shape was the presence of a distinct correlation between the orientation of ripple asymmetry and the flood - or ebb - dominance of the tidal wave. This is shown in Fig. 3.33 which shows the bed elevation measured at the middle of the cross section along three different reaches of the channel, the first (a) located in the ebb dominated portion of the channel, the second (c) located in the flood dominated reach and the second (b) located in between the latter two reaches. The quasi 2D ripple pattern was again replaced by complex 3D patterns all along the channel after the first hours of experiment (Fig. 3.34).

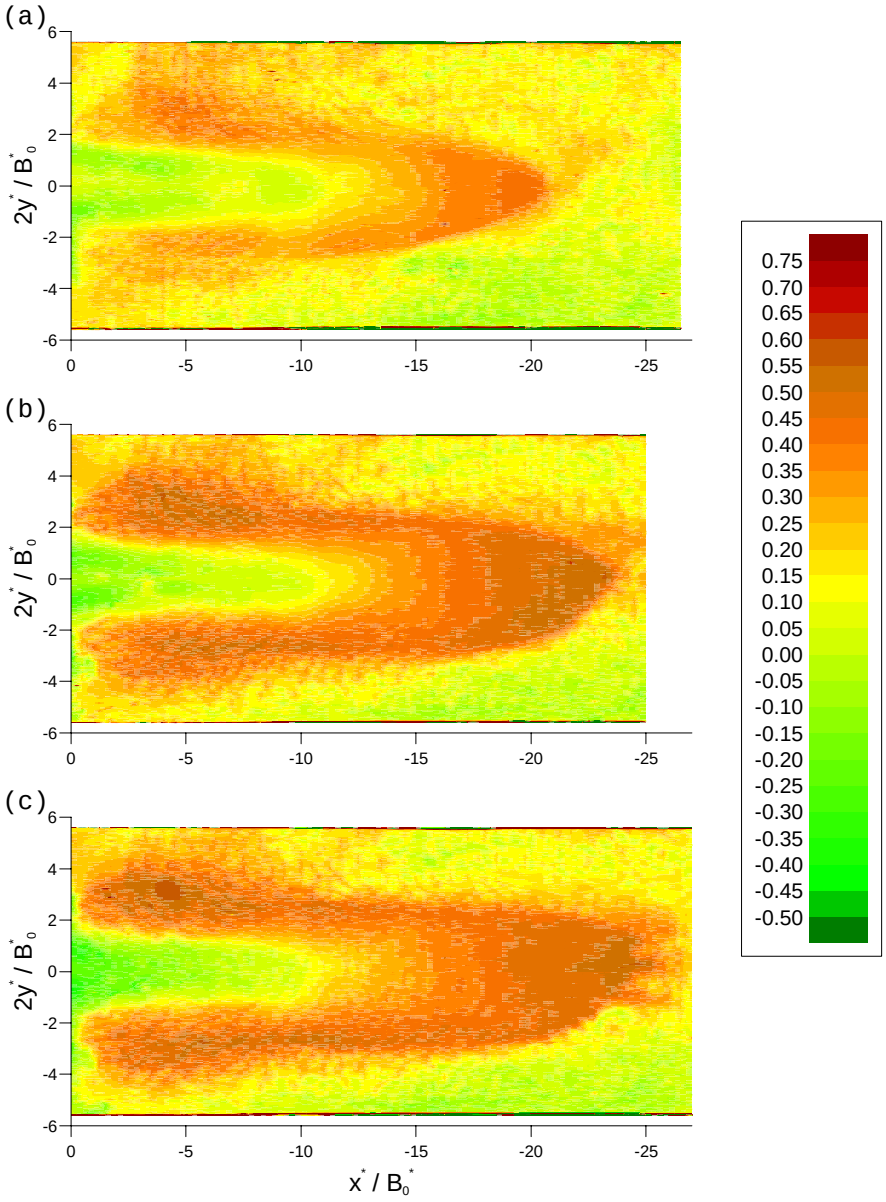

Figure 3.29: Evolution of the pattern of bed elevation measured in the sea basin at different times in experiment 2. (a) $t^* = 20\ T$, (b) $t^* = 60\ T$, (c) $t^* = 100\ T$.

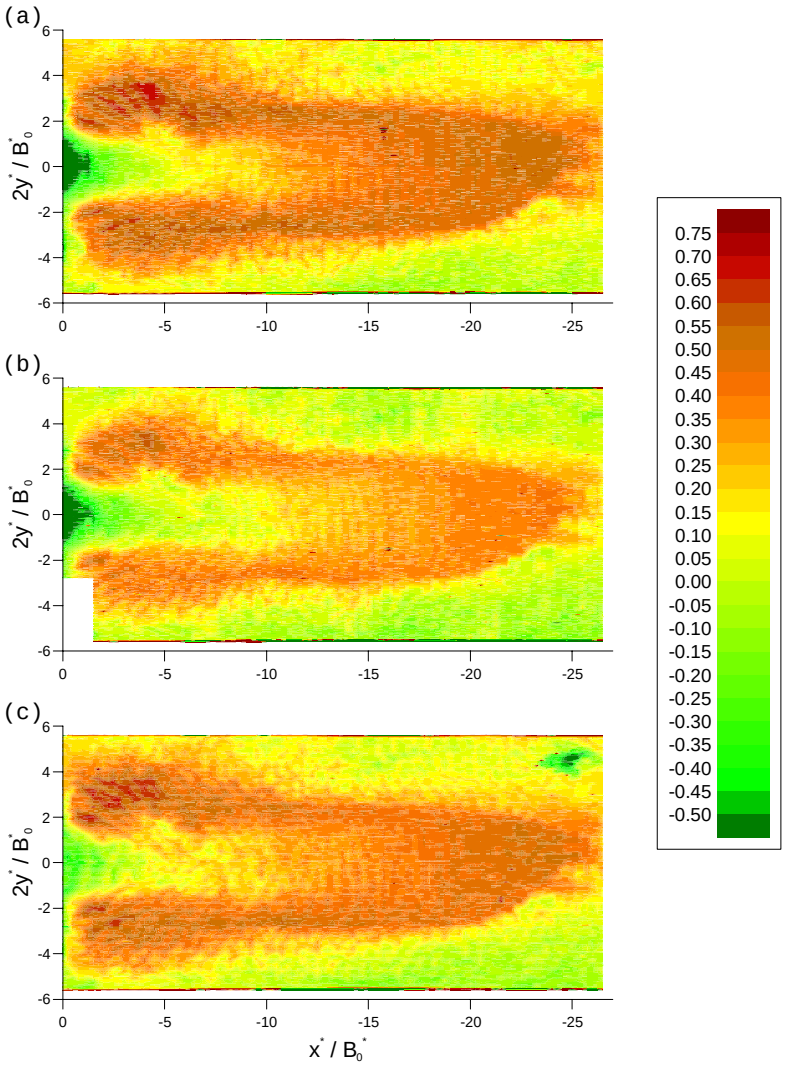

Figure 3.30: Evolution of the pattern of bed elevation measured in the sea basin at different times in experiment 2. (a) $t^* = 200\ T$, (b) $t^* = 500\ T$, (c) $t^* = 1000\ T$.

Figure 3.31: A picture of the ripple pattern observed along the channel in the initial phase of experiment 2.

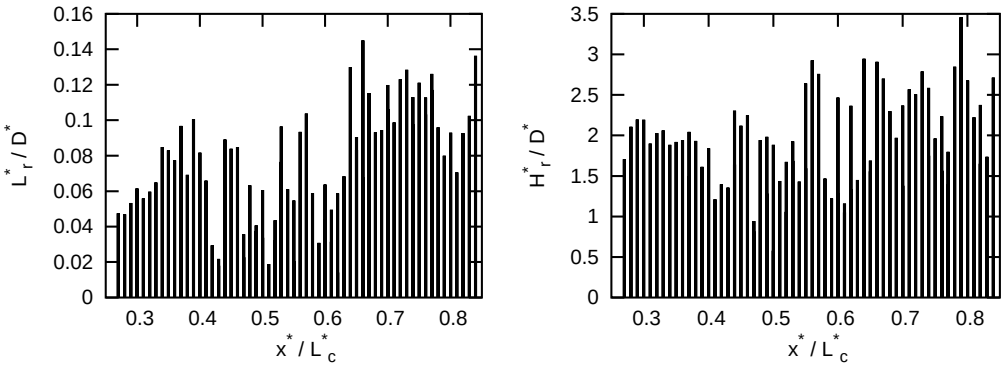

Figure 3.32: Spatial ditribution of the dimensionless ripple wavelength (left) and height (right) along the channel.

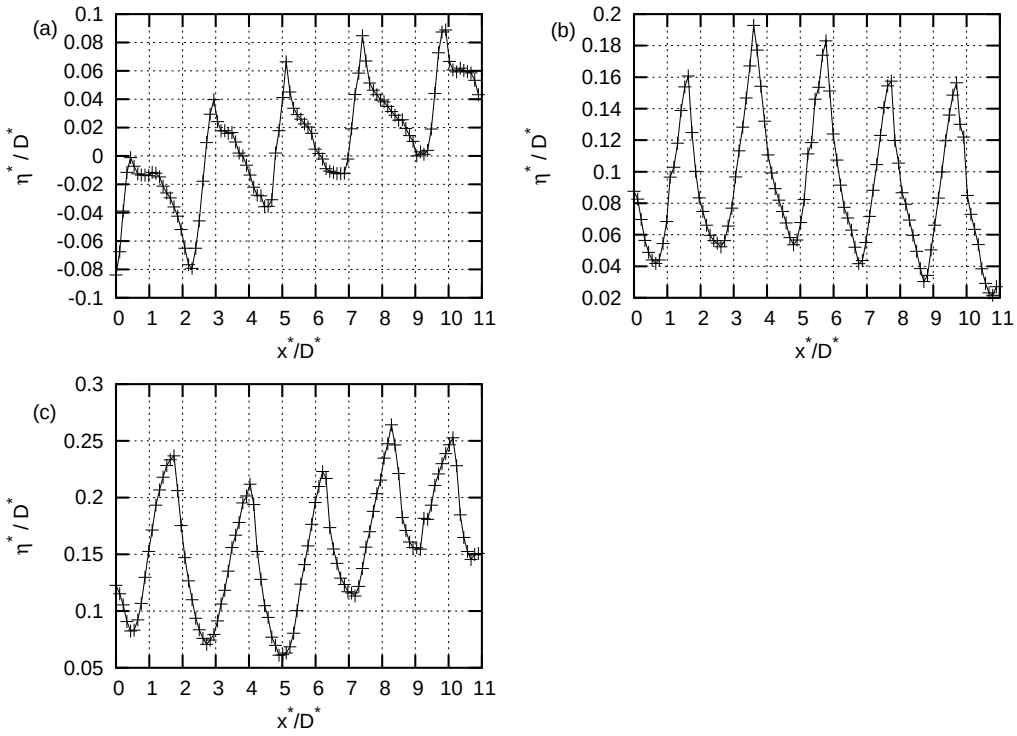

Figure 3.33: The profile of three sequences of ripples measured at the middle of the cross section along (a) an ebb-dominated reach, (c) a flood-dominated reach and (b) a reach with no dominance, showing the distinct correlation between dominance and ripple asymmetry.

Figure 3.34: A picture of the complex 3D ripple pattern observed in the second experiment.

3.5.4 Bars.

Like in the first experiments, bars formed in experiment 2 after about 50 tidal cycles. An alternate ripple and pool pattern can be detected in Fig. 3.35: note that, in the latter plot, the average bed profile has been subtracted, while the contribution of ripples to the fairly complex pattern is retained. Bar wavelength can be estimated to range about 3 channel widths (Fig. 3.36), a value consistent with the theoretical predictions of *Seminara and Tubino* [2001]. In fact, Fig. 3.37 shows a stability plot and and Fig. **??**b gives the bar growth rate calculated as a function of the dimensionless wavenumber on the basis of the above theory using the values of physical parameters appropriate for experiment 2. The latter curve indeed suggests that the critical value of bar wavelength ranges about 4 channel widths.

Alternate bars did not spread throughout the whole channel, but they rather concentrated in the middle reach.

3.6 Discussion and concluding remarks.

In the present laboratory investigations several features typical of estuarine environments where observed.

The theoretical results of *Lanzoni and Seminara* [2002] and those discussed in the previous chapter suggesting that tidal channels closed at one end and connected to the other end with a tidal sea can achieve a morphodynamic equilibrium characterized by a vanishing net sediment flux in a tidal cycle at each cross section and the formation of a 'beach' close to the landward end of the channel are confirmed. Moreover, a major observation emerged from the experiment is the fact that the bed elevation established close to the inlet at equilibrium results from the readjustment of the bed profile in the whole channel. In other words, except for the immediate neighbourhood of the inlet where the flow acceleration induced by streamline convergence during the flood phase gives rise to enhancement of local scour, the equilibrium cross section develops near the inlet as a result of non local effects. It will be of interest in the near future to investigate sistematically whether a relationship can be established between the length of a tidal channel at equilibrium and the flow depth established at the entrance, for given values of the hydrodynamic parameters.

Further interesting observations emerged on the formation of large and small scale bedforms. In fact, tidal free bars were observed according to the recent theory of *Seminara and Tubino* [2001]. Bar's wavelength ranged typically about few channel widths, though the fairly low values attained by

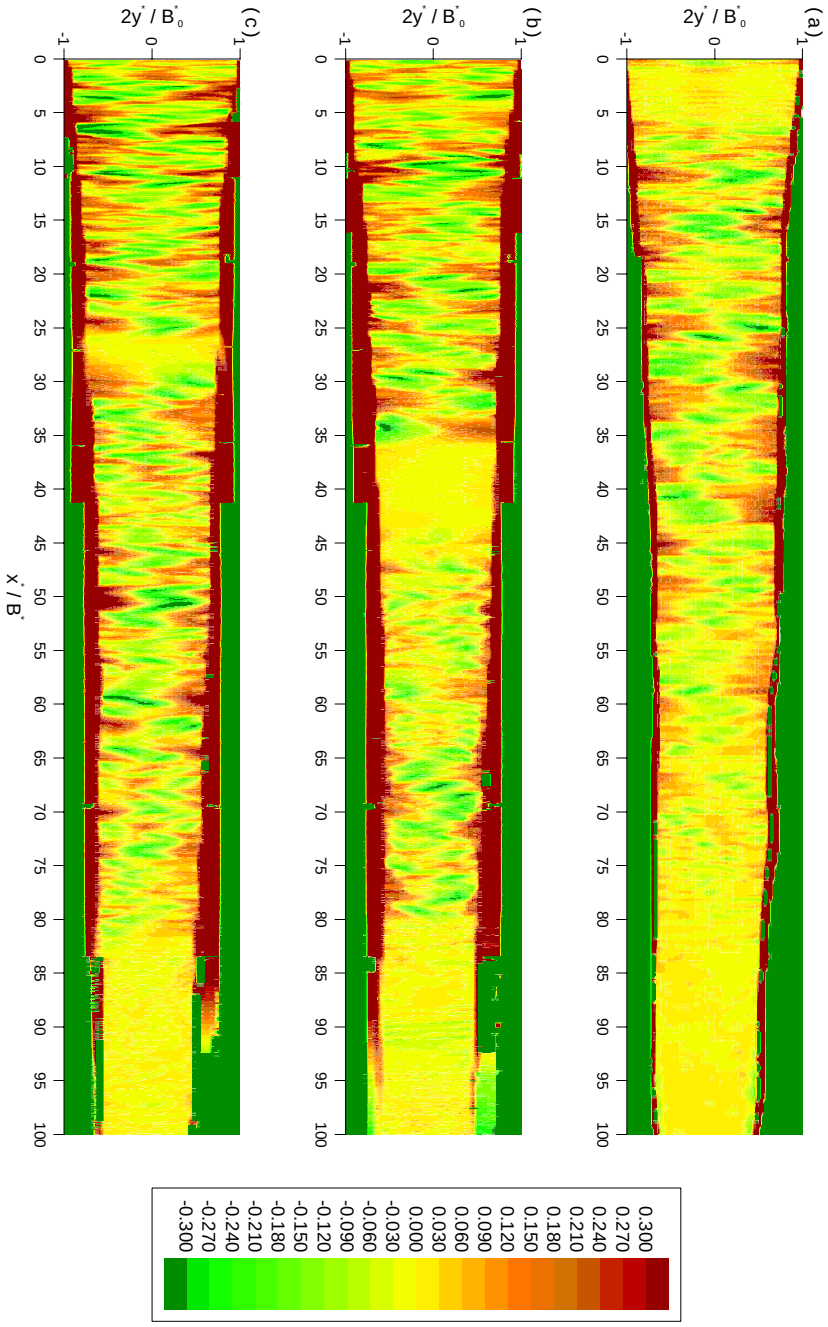

Figure 3.35: The pattern of bottom topography in the channel at different times, showing the presence of alternate bars. The cross sectionally averaged bed profile has been filtered out. Bottom elevation is scaled by the local flow depth. (a) $t^* = 200\ T$, (b) $t^* = 1000\ T$, (c) $t^* = 2000\ T$.

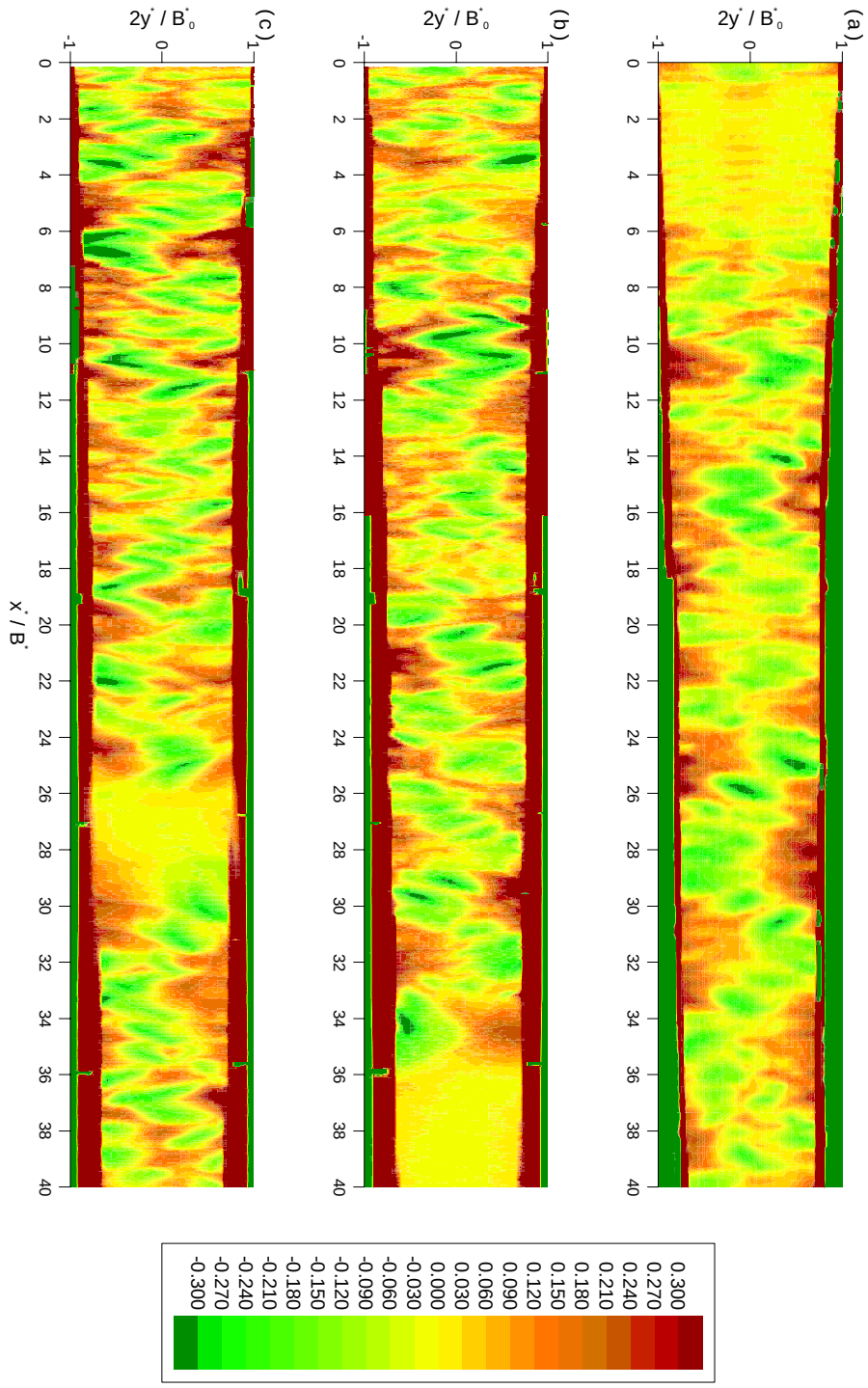

Figure 3.36: The pattern of bed topography in the seaward portion of the channel at different times, showing the presence of alternate bars. The cross sectionally averaged bed profile has been filtered out. Bottom elevation is scaled by the local flow depth. (a) $t^* = 200\ T$, (b) $t^* = 1000\ T$, (c) $t^* = 2000\ T$.

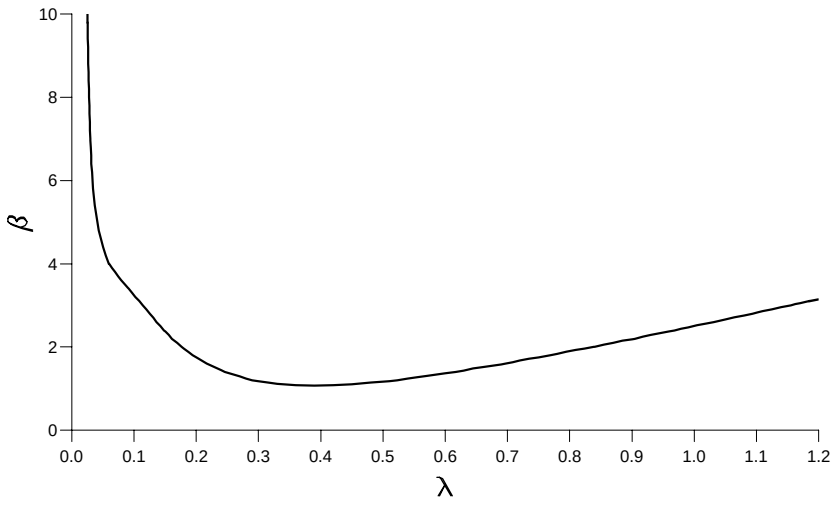

Figure 3.37: The marginal stability curve calculated on the basis of the theoretical approach of *Seminara and Tubino* [2001], using the values of physical parameters appropriate to experiment 2. ($d_{50}^* = 0.31\ mm$, $\rho_s/\rho = 1.48$, $D_0 = 0.09\ m$, $U_0^* = 0.3\ m$)

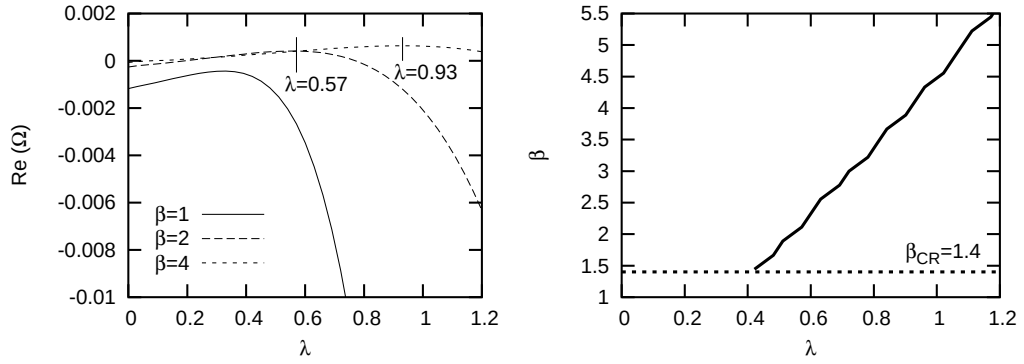

Figure 3.38: The real part of the growth rate (left) and the values of λ corresponding to the maximum growth rate for a given β (right) calculated on the basis of the theoretical approach of *Seminara and Tubino* [2001], using the values of physical parameters appropriate to experiment 2. ($d_{50}^* = 0.31\ mm$, $\rho_s/\rho = 1.48$, $D_0 = 0.09\ m$, $U_0^* = 0.3\ m$)

the aspect ratio of the channel prevented bars from attaining large amplitudes. At a smaller scale, the present laboratory observations also allowed to observe the formation of tidal ripples, typically displaing a 2D pattern at the very initial stage of the experiments replaced, later, by complex 3D patterns. The actual nature of such forms, namely the fact that they should be identified as ripples rather than dunes, has also been demonstrated.

Finally, the experiments allowed to show that the degree of ebb-flood flow asymmetry in the 'sea' region close to the inlet is reduced compared with that one observed and predicted in the fixed bed case by *Blondeaux et al.* [1982]. In fact, the seaward current generated close to the channel inlet leads to an intense scour of the bed and to the generation of a submerged channel which progresses seaward until it reaches a quasi-equilibrium configuration.

However there are still several questions which will require attention in the near future, in particular:

- does an equilibrium of the channel still exist in the presence of intertidal storage areas?
- what is the effect of the lateral exchange of sediments between channel and the tidal flats on the morphodynamic evolution of tidal flats and saltmarshes?
- what is the role played by the hydrodynamics and morphodynamics of tidal inles on the exchange of sediments between channels and adjacent seas?
- what is the effect of the meandering of the tidal channel on its long term equilibrium?

Some of the basic mechanisms underlying the latter questions will be investigated in the near future in order to reduce the gap between necessarily simiplified theoretical models and the complexity of natural systems.

Bibliography

Blondeaux, P., De Bernardinis, B. and Seminara, G., Correnti di marea in prossimità di imboccature e loro influenza sul ricambio lagunare, *Atti XVIII Conv. Idraulica e Costruzioni Idrauliche*, Bologna, 21-23 Sett. 1982.

Bolla Pittaluga, M. , Long term morphodynamic equilibrium of tidal channels: settling lag, overtides and sediment supply, *Water Resour. Res.*. To be submitted.

Bolla Pittaluga, M. and Seminara, G., Depth integrated modelling of suspended sediment transport, *Water Resour. Res.*, 2002. In press.

Cola, S. and Simonini, P., Mechanical behavior of silty soils of the Venice lagoon as a function of their grading characteristics, *Can. Geotech. J., 39 (4)*, 879-893, 2002.

Dalrymple, R.W., Rhodes, R.M., Estuarine dunes and bars. In *Geomorphology and Sedimentology of Estuaries*, Developments in Sedimentology, Elsevier, 53 pp., 1995.

Defina, A., Two-dimensional shallow flow equations for partially dry areas, *Water Resour. Res., 36 (11)*, 3251-3264, 2000.

Defina, A., D'Alpaos, L., Matticchio, B., A new set of equations for very shallow water and partially dry areas suitable to 2D numerical models. In *Proceedings of the Specialty Conference on Modelling of Flood Propagation Over Initially Dry Areas*, Milan (Italy), edited by P. Molinaro and L. Natale, 72-81, 1994.

Dongeren, A.R. van and de Vriend, H.J., A model of morphological behaviour of tidal basins, *Coastal Engineering,* 287-310, 1994.

Exner, F. M., Uber die wechselwirkung zwischen wasser und geschiebe in flussen, *Acad. Wissenscaften*, Wien, Sitz. Ber. Abt. IIa, Band 134, 165-180, 1925.

Galappatti, R., A depth-integrated model for suspended transport, *Delft University of Technology, Faculty of Civil Eng.,* Report No.83-7, 1983.

Galappatti, R. and Vreugdenhil, C.B., A depth-integrated model for suspended sediment transport, *J. Hydr. Res., 23 (4)*, 359-377, 1985.

Jay, D. A., Green's law revisited: Tidal long-wave propagation in channels with strong topography, *J. Geophys. Res., 96* , 20585-20598, 1991.

Katopodi, I. and Ribberink, J. S., Quasi-3D modelling of suspended sediment transport by currents and waves, *Coastal Engineering, 18,* 83-110, 1992.

Lanzoni, S. and Seminara, G., On tide propagation in convergent estuaries, *J. Geoph. Res., 103 (C13),* 30793-3812, 1998.

Lanzoni, S. and Seminara, G., Long term evolution and morphodynamic equilibrium of tidal channels, *J. Geoph. Res., 107 (C1),* 1-13, 2002.

Marchi, E., Sulla stabilità delle bocche lagunari a marea, *Rend. Accademia Nazionale dei Lincei*, Roma, Serie IX, 1, 137-150, 1990.

Meyer-Peter, E., Müller, R., Formulas for bedload transport, *2nd Congress IAHR*, Int. Ass. of Hydraul. Res., Sweden, Stockholm, 1948.

Nayfeh, A.H., Perturbation methods, *John Wiley & Sons, Ltd,* New York, 1973.

Parker, B.B., The relative importance of the various nonlinear mechanisms in a wide range of tidal interactions. In *Tidal Hydrodynamics*, edited by B.B. Parker, John Wiley & Sons, Ltd, New York, 237 - 268, 1991.

Pritchard, D., Hogg, A.J. and Roberts, W., Morphological modelling of intertidal mudflats: the role of cross-shore tidal currents. *Cont. Shelf Res. 22 (11-13)*, 1887-1895, 2002.

Rijn, L.C. van, Sediment transport, Part I: Bedload transport, *J. Hydr. Engrg., ASCE, 110(11),*, 1431-1456, 1984a.

Rijn, L.C. van, Sediment transport, Part II: suspended load transport, *J. Hydr. Engrg., ASCE, 110(11),* 1613-1641, 1984b.

Schuttelaars, H. M., de Swart, H. E., An idealized long-term morphodynamic model of a tidal enbaynment, *Eur. J. Mech., B/Fluids, 15*, 55-80, 1996.

Schuttelaars, H. M. and de Swart, H. E., Multiple morphodynamic equilibria in tidal embayment, *J. Geoph. Res., 105*, 24105-24118, 2000.

Seminara, G. and Tubino, M., Sand bars in tidal channels. Part 1: Free bars, *J. Fluid. Mech., 440,* 49-74, 2001.

Shetye, S.R.G., Gouveya, A.D., On the role of geometry of cross-section in generating flood dominance in shallow estuaries, *Estuarine, Coast. and Shelf Sci., 35*, 113 - 126, 1992.

Solari, L., Seminara, G., Lanzoni, S., Marani, M. and Rinaldo, A., Sand bars in tidal channels. Part 2. Tidal meanders, *J Fluid. Mech. 451*, 203-238, 2002.

Speer, P.E., Aubrey, D.G., A study on non-linear tidal propagation in shallow inlet/estuarine systems. Part II: Theory, *Estuarine Coast. and Shelf Sci., 21*, 206 - 240, 1985.

Sumer, B.M. and Bakioglu, M., On the formation of ripples on an erodible bed, *J. Fluid Mech., 144,* 177-190, 1984.

Wang, Z.B., Theoretical analysis on depth-integrated modelling of suspended sediment transport, *J. Hydr. Res., 30 (3),* 403-421, 1992.

Tambroni, N., Bolla Pittaluga, M. and Seminara, G., Long term morphodynamic equilibrium of tidal channels. Experimental observations, *Water Resour. Res.*. To be submitted.

Toro, E.F., Shock-capturing methods for free surface shallow flows, *John Wiley & Sons, Ltd*, New York, 2001.